中国科学技术大学

博士学位论文

相对论重离子碰撞实验中双电子的产生

作者姓名：　郭毅
学科专业：　粒子物理与原子核物理
导师姓名：　许怒　张子平
完成时间：　二○一四年八月

University of Science and Technology of China

A dissertation for doctor degree

Dielectron production in $\sqrt{s_{NN}}$ = 200 GeV p+p and Au+Au collisions at RHIC

Author's Name :	Yi Guo
Speciality :	Particle Physics and Nuclear Physics
Supervisor :	Nu Xu. Ziping Zhang.
Finished Time :	Aug, 2014

相对论重离子碰撞实验中双电子的产生

近代物理系（4系）　郭毅　中国科学技术大学

中国科学技术大学学位论文原创性声明

本人声明所呈交的学位论文, 是本人在导师指导下进行研究工作所取得的成果。除已特别加以标注和致谢的地方外，论文中不包含任何他人已经发表或撰写过的研究成果。与我一同工作的同志对本研究所做的贡献均已在论文中作了明确的说明。

作者签名：_____ 签字日期：_____

中国科学技术大学学位论文授权使用声明

作为申请学位的条件之一，学位论文著作权拥有者授权中国科学技术大学拥有学位论文的部分使用权，即：学校有权按有关规定向国家有关部门或机构送交论文的复印件和电子版，允许论文被查阅和借阅，可以将学位论文编入《中国学位论文全文数据库》等有关数据库进行检索，可以采用影印、缩印或扫描等复制手段保存、汇编学位论文。本人提交的电子文档的内容和纸质论文的内容相一致。

保密的学位论文在解密后也遵守此规定。

□ 公开 □ 保密 _____ 年

作者签名：_____ 导师签名：_____

签字日期：_____ 签字日期：_____

摘 要

相对论重离子碰撞实验的主要目的是研究 QCD 自由度下核物质的结构，包括有限温度和密度下 QCD 物质的性质，以及寻找 QCD 相变的临界点和一阶相变的边界。近年来，RHIC 和 LHC 的实验通过对末态强子的测量结果表明，在高能重离子碰撞中形成了一种新的物质形态——强耦合的夸克胶子等离子体(sQGP)。双轻子作为一种电磁探针，由于其不参与强相互作用，因此在产生之后，它们能不受影响的穿过高能重离子碰撞形成的介质。同时，双轻子能够在系统演化的各个阶段产生，使它们成为研究高能重离子碰撞中产生的介质性质的优秀探针。

由于关注的物理不同，双轻子的动力学相空间一般被分为 3 个不变质量质量区间。低质量区间（$M_{ll} < M_{\phi}$），双轻子的产生主要来源于介子在强子介质中的多次散射。在中间质量区间（$M_{\phi} < M_{ll} < M_{J/\psi}$），双轻子的主要来源于 QGP 物质的热辐射，以及重味夸克介子的半轻子衰变。在高质量区间（$M_{ll} > M_{J/\psi}$），双轻子主要来源于 Drell-Yan 过程和重味夸克偶素的衰变。

本文主要讨论 STAR 实验组在 $\sqrt{s}$ = 200 GeV 下的质子质子对撞和金金对撞中对双电子产生的测量。STAR 实验在 2010 至 2012 年间积累了大量的实验数据，同时桶部飞行时间探测器（TOF）的安装完成大大增强了 STAR 探测器鉴别电子（正电子）的能力，使得在 STAR 实验中测量双轻子成为可能。通过分析 2012 年采集数据得到的双电子不变质量谱极大地提高了质子质子对撞中双轻子不变质量谱的精度（与 STAR 实验之前的测量 [1] 比较，统计量提高了 7 倍左右)。通过在 200GeV 金金 MinBias（0-80% 中心度）碰撞中双轻子不变质量谱与强子衰变模拟和模型计算的比较，我们发现，在质量区间 0.3~0.76 GeV/c^2 中，双轻子的产生相对于不包含 ρ 介子贡献的强子衰变模拟结果有 1.66±0.06(stat.)±0.24(sys.)±0.33(cocktail) 倍的增强。对于这个增强因子，我们并未观测到明显的中心度依赖性和横动量依赖性。在中心对撞中（0-10% 中心度)这个增强因子比 PHENIX 实验观测到的结果要小。基于 ρ 介子在介质中质量谱展宽的模型计算可以很好的解释我们观测到的增强。同时本文也会讨论可能存在的相关联的重味夸克在介质中的修正效应，以及通过双轻子衰变道对 ω 介子和 ϕ 介子产生的测量。

关键词： 双轻子，矢量介子，手征对称性

ABSTRACT

The mission of a ultra-relativistic heavy ion program is to study the structure of nuclear matter with the QCD degrees of freedom including QCD matter at finite temperature and density in the laboratory and search for the QCD critical point and first-order phase boundary. Many experimental evidences have been found to demonstrate the formation of a strongly-coupled Quark-Gluon Plasma (sQGP). These evidences are mostly from hadron measurements in high energy heavy ion collisions at RHIC and LHC. Dileptons as an electromagnetic probe, escape the interacting system without suffering further strong interactions after their production. In addition, dilepton can be produced on the various stages of entire system evolution. They are therefore expected to be outstanding probes to study the property of the medium created in high energy heavy ion collisions.

Traditionally, due to different physics of interest, dilepton kinematic phase space is divided into 3 mass regions. In the Low Mass Region - LMR ($M_{ll} < M_{\phi}$), dileptons are produced via multiple hadron-hadron scattering by coupling to vector mesons. In the Intermediate Mass Region - IMR ($M_{\phi} < M_{ll} < M_{J/\psi}$), dilepton production is dominated by contributions from the thermal radiation and semilepton decay of the correlated charmed meson. Drell-Yan process and the decay heavy quarkonia contribute mainly for the dilepton source in the High mass Region - HMR ($M_{ll} > M_{J/\psi}$).

In this thesis, I will report the measurement on dielectron production in p+p and Au+Au collisions at $\sqrt{s_{NN}}$ = 200 GeV for the STAR experiment. The large data set collected during year 2010~2012, as well as the completion of barrel Time-Of-Flight (TOF) installation in year 2010, provides electron/position samples with high statistics and purity which makes it possible for dielectron measurement at the STAR experiment. The dielectron results from 200 GeV p+p collisions have greatly improved (~7 times more) statistics comparing to the previous published result from STAR [1]. The results from Au+Au collision at $\sqrt{s_{NN}}$ = 200 GeV are compared with hadronic decay cocktail and model calculations. We observed an enhancement factor of $1.66 \pm 0.06(stat.) \pm 0.24(sys.) \pm 0.33(cocktail)$ in mass region 0.3~0.76 GeV/c^2 when comparing to the hadronic cocktail without ρ contribution. This result is extracted from the 200 GeV minimum bias Au+Au collisions and we do not observe strong centrality nor transverse

momentum dependence. In the most top 10% central collisions, this enhancement is smaller than the PHENIX results [2, 3]. The model calculation based on in-medium broadening of ρ spectra function can reproduce the enhancement. I will also report the study of possible modification of the correlated charm and the measurements of ω and ϕ production through their dielectron decay channels.

Keywords: Dilepton， vector meson, chiral symmetry

Contents

List of Tables

List of Figures

Chapter 1 Introduction

1.1 Standard model and Quantum Chromodynamics

The Standard Model of particle physics is a theory concerning the electromagnetic, weak, and strong nuclear interactions, which explains how the basic building blocks of matter interact. The Standard Model includes members of several classes of elementary particles: 12 elementary particles of spin 1/2 known as fermions, 4 gauge bosons of spin 1 who carry the force of fundamental interactions and Higgs boson of spin 0 which interacts with elementary particles and gives them mass. The 12 fermions includes 6 quarks (up (u), down (d), strange (s), charm (c), top (t), bottom (b)), and 6 leptons (electron (e), muon (μ), tau (τ) and the corresponding neutrinos). The 4 gauge bosons are gluon (g), photon (γ), W and Z bosons, which are classified by the fundamental force they carry. Gluons mediate the strong interactions between color charged particles (quarks). Gluons also carry color charge, so they can also interact with themselves. The strong interaction are described by the theory of quantum chromodynamics. The electric charged particles interact through the electromagnetic force mediated by photons which is well-described by the theory of quantum electrodynamics. The weak force is carried by W and Z bosons. They are grouped with photons, as collectively mediation the electroweak interaction. Figure 1.1 shows the particles generations and interactions between them. Fermions interact with each other through the fundamental force carried by gauge bosons and form the matter world. On 14 March 2013, the Higgs boson was tentatively confirmed to exist.

1.1.1 Quantum Chromodynamics (QCD)

In the 1950s, a large number of strongly interacting particles (hadrons) were discovered in particle physics experiments. To understand and explain the spectrum of these particles, in 1963, Gell-Mann and Zweig proposed a model in terms of elementary constituents called *quarks*. The hadrons could be sorted into groups having similar quantum properties by the existence of three flavors of quarks inside hadrons. Mesons were expected to be quark-antiquark bound states, while baryons were interpreted as bound states of three quarks. To explain the electric charges and other quantum numbers of hadrons, Gell-Mann and Zweig assumed three species of quarks, up (u), down (d) and

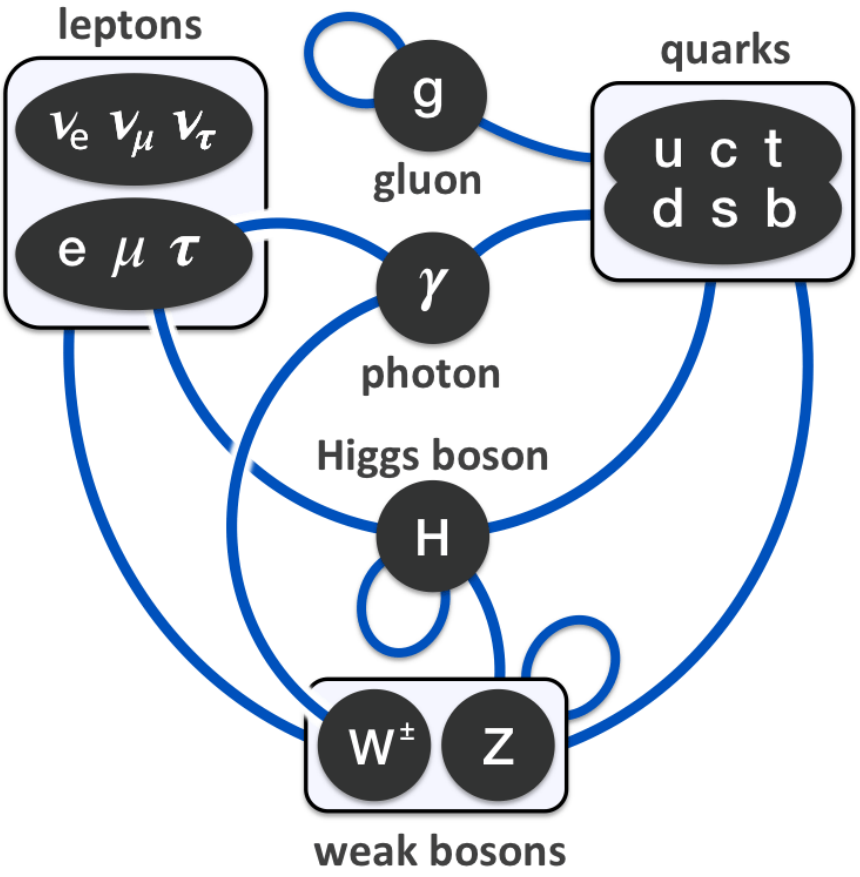

Figure 1.1 Summary of interactions between particles described by the Standard Model.

strange (*s*). With the discovery of more hadrons, the quarks family were extended of three more species: charm (*c*), bottom (*b*) and top (*t*). To make baryons with integer charges, the quarks were assigned fractional electric charge: +2/3 for *u*, *c, t,* and -1/3 for *d*, *s*, *b.* And all quarks were assumed to be spin-1/2. The quark model had great success in predicting new hadronic states, but some hadrons composed with three identical quarks with parallel spin, such as $\Delta^{++}(uuu)$, are forbidden by the Pauli exclusion principle. To solve this problem, Han and Nambu, Greenberg, and Gell-Mann introduced an additional SU(3) gauge degree of freedom of quarks called *color* and an octet of vector gauge bosons called gluons to carry the interaction between quarks. In 1972, Gell-Man and Fritzsch introduced the Quantum Chromodynamics (QCD) to describe the strong interaction between the colored quarks and gluons.

The QCD Lagrangian can be written as:

$$\mathcal{L}_{\text{QCD}} = -\frac{1}{4}F_a^{\mu\nu}F^a_{\mu\nu} + \sum_f \bar{q}_f{}^i i\gamma^\mu (D_\mu)_{ij} q_f^j - \sum_f m_f \bar{q}_f^i q_f^i \tag{1.1}$$

$$F_a^{\mu\nu} = \partial^\mu G_a^\nu - \partial^\nu G_a^\mu + g_s f^{abc} G_b^\mu G_c^\nu \tag{1.2}$$

$$D^{\mu} = \partial^{\mu} - ig_s \frac{\lambda^a}{2} G_a^{\mu} \tag{1.3}$$

where g_s is the QCD coupling constant, and the f^{abc} are the structure constants of the $SU(3)_C$ algebra. q_f^i defines a quark field with color *i* and flavor *f*, while γ^{μ} are the Dirac matrices. $F_a^{\mu\nu}$ are the field strengths tensor which were introduced to describe the self-interaction of the gluon fields. D^{μ} are the covariant derivative with the Gell-Mann matrices λ^a and the Yang-Mills (gluon) fields $G_{\mu}^{a}(x)$ where a =1, 2, ..., 8.

1.1.2 Running coupling

The effective QCD coupling constant $\alpha_s(Q)$ can be written as:

$$\alpha_s(Q) \equiv \frac{g_s^2(Q)}{4\pi} \approx \frac{4\pi}{\beta_0 \ln(Q^2/\Lambda_{QCD}^2)} \tag{1.4}$$

Where β_0 is a constant larger than 0 which depends on the number of quarks with mass less than the energy scale Q. The coupling $\alpha_s(Q)$ shows a dependence on the renormalization scale. Figure 1.2 shows the measurements of α_s as a function of the energy scale *Q*. The world average result of $\alpha_s(M_z^2) = 0.1179 \pm 0.0008$ [5] and the QCD scale is Λ_{QCD}~200 MeV. With decreasing interaction distance and increasing momentum transfer, the coupling constant decreases, the interaction between quarks and gluons becomes weaker. This is the major feature of QCD: asymptotic freedom. While the energy scale $Q \gg \Lambda_{QCD}$ (short distance and high momentum transfer), QCD can be described with perturbative method (perturbative QCD). On the other hand, pQCD breaks down when the $Q \sim \Lambda_{QCD}$ where QCD becomes strongly coupled. People introduced Lattice QCD to calculated QCD in this case.

1.1.3 Chiral symmetry

We consider the Lagrangian of two flavors massless fermions, and the results will be directly applicable to massless QCD. The Lagrangian is given by:

$$\mathcal{L} = i\bar{\psi}_j \gamma_{\mu} \partial^{\mu} \psi_j \tag{1.5}$$

where the index *j* presents the two different flavors (*u*, *d*). Consider two transformation :

1. vector transformation Λ_V :

$$\Lambda_V : \ \psi \rightarrow e^{-i\frac{\vec{\tau}}{2}\vec{\Theta}}\psi \simeq (1 - i\frac{\vec{\tau}}{2}\vec{\Theta})\psi \tag{1.6}$$

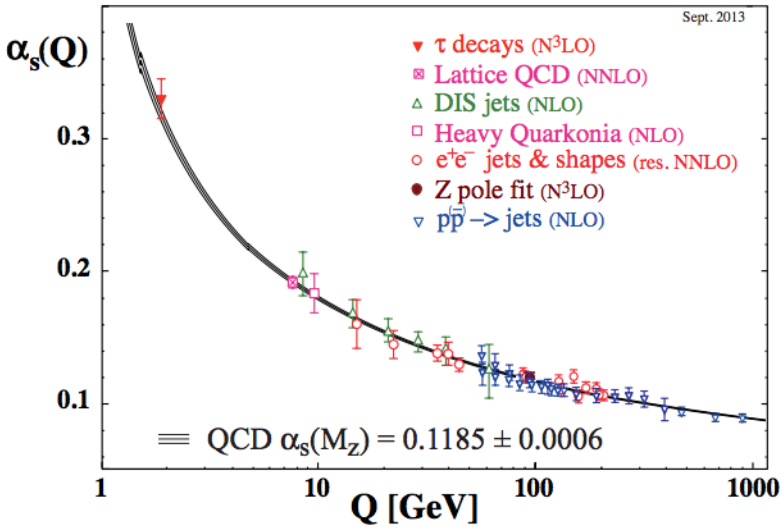

Figure 1.2 Summary of measurements of α_s as a function of the energy scale Q. Figure is taken from [5].

and its conjugate form:

$$\Lambda_V : \ \bar{\psi} \to e^{+i\frac{\vec{\tau}}{2}\vec{\Theta}}\bar{\psi} \simeq (1 + i\frac{\vec{\tau}}{2}\vec{\Theta})\bar{\psi} \tag{1.7}$$

where $\vec{\tau}$ is the Pauli-spin-matrices and $\vec{\Theta}$ are the rotation angle. ψ is the Dirac iso-spinor for fermions, $\psi = (\psi_u, \psi_d)$. Clearly the Lagrangian is invariant under Λ_V and the associated conserved current is

$$V^a_\mu = \bar{\psi}\gamma_\mu\frac{\tau^a}{2}\psi \tag{1.8}$$

2. axial transformation Λ_A

$$\Lambda_A : \ \psi \to e^{-i\gamma_5\frac{\vec{\tau}}{2}\vec{\Theta}}\psi \simeq (1 - i\gamma_5\frac{\vec{\tau}}{2}\vec{\Theta})\psi \tag{1.9}$$

$$\bar{\psi} \to e^{-i\gamma_5\frac{\vec{\tau}}{2}\vec{\Theta}}\bar{\psi} \simeq (1 - i\gamma_5\frac{\vec{\tau}}{2}\vec{\Theta})\bar{\psi} \tag{1.10}$$

The Lagrangian transforms as following :

$$i\bar{\psi}\gamma^\mu\partial_\mu\psi \to i\bar{\psi}\gamma^\mu\partial_\mu\psi - i\vec{\Theta}(\bar{\psi}i\partial_\mu\gamma^\mu\gamma_5\frac{\vec{\tau}}{2}\psi + \bar{\psi}\gamma_5\frac{\vec{\tau}}{2}i\partial_\mu\gamma^\mu\psi) \tag{1.11}$$

since γ_5 anti-commutes with γ_μ, the last term vanishes. Therefore the Lagrangian is also invariant under Λ_A with the conserved 'axial-vector' current:

$$A^a_\mu = \bar{\psi}\gamma_\mu\gamma_5\frac{\tau^a}{2}\psi \tag{1.12}$$

So, the Lagrangian of massless QCD is invariant under the vector and axial transformations. This symmetry is called *chiral symmetry*. If we introduce a mass term in the Lagrangian.

$$\delta\mathcal{L} = -m(\bar{\psi}\psi) \tag{1.13}$$

It can easily prove the $\delta\mathcal{L}$ is invariant under the vector transformations, but the axial transformations symmetry is broken. In case of QCD, the mass of the light quarks are very small (about 5~10 MeV) comparing to the QCD energy scale which is about 200 MeV. Therefore, the Λ_A should be an approximate symmetry. And the slight symmetry breaking due to the quark masses is called Partial Conserved Axial Current hypothesis (PCAC).

1.1.4 Spontaneous breaking of chiral symmetry

The conservation of chiral symmetry leads to a direct deduction that the chiral partners which can be rotated into each other by the operation Λ_A should have the same masses, since they should have the same Eigenvalues. However, in the real world, this is clearly not true, since the chiral partner ρ and a_1 have quite difference masses ($m_\rho = 770$ MeV and $m_{a_1} = 1260$ MeV) which should be degenerate if the chiral symmetry is conserved. In additional, this can not be explained by the slight symmetry breaking due to the finite current quark masses, which should lead to a mass difference much smaller than the particle mass. However, the mass difference between ρ and a_1 is of the same order as ρ mass. On the other hand, let us consider the weak decay of pion which is controlled by the matrix element of the axial current between vacuum and pion

$$\left\langle 0|A^a_\mu(x)|\pi^b(q)\right\rangle = -if_\pi q_\mu \delta^{ab} e^{-iq\cdot x} \tag{1.14}$$

and f_π is a constant ~ 93 MeV which measures the strength of the symmetry breaking. If we take the divergence of eq. 1.14

$$\left\langle 0|\partial^\mu A^a_\mu(x)|\pi^b(q)\right\rangle = -if_\pi q_\mu q^\mu \delta^{ab} e^{-iq\cdot x} = -f_\pi m_\pi^2 \delta^{ab} e^{-iq\cdot x} \tag{1.15}$$

, comparing to the hadronic scales, the pion mass is vanishing, thus the axial current is approximately conserved which supports for the conservation of chiral symmetry.

To solve the contradiction discussed above, the spontaneous breakdown of chiral symmetry was introduced. The breaking of symmetry has two conditions: explicit breaking, which is due to the explicit asymmetry in the Lagrangian, i.e. the finite mass of quarks in QCD; spontaneous breaking, which means the symmetry is not realized in

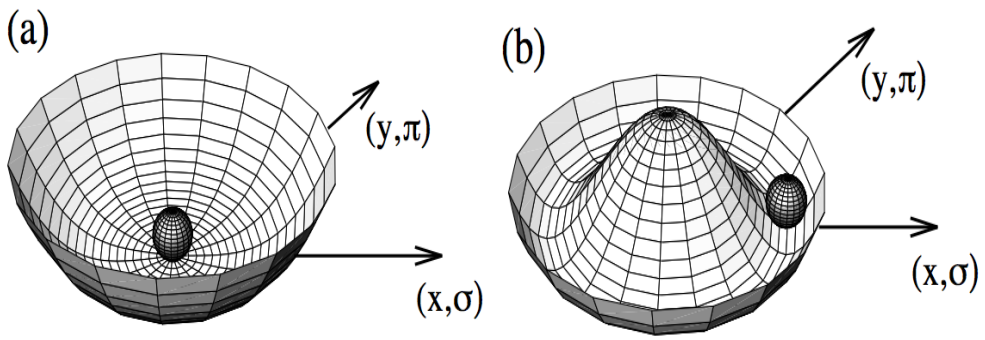

Figure 1.3 (a) No spontaneous breaking of symmetry. (b) Spontaneous breaking of symmetry.

the ground state. We consider effective potentials shown in fig 1.3. Panel (a) shows a potential with ground state just in the middle. The ground state plus potential are invariant under axial rotations. In panel (b), any points in the valley can be the ground state. If we chose one direction as the ground state, the axial rotation symmetry is obviously spontaneously broken, since the Lagrangian is invariant but the vacuum is not.

The QCD vacuum of quark-antiquark condensate $\langle 0 \left| \bar{q}q \right| 0 \rangle$ can be related to f_π by the Gell-Mann-Oakes-Renner relation (GOR):

$$m_\pi^2 f_\pi^2 = -2\bar{m} \langle 0 \left| \bar{q}q \right| 0 \rangle \tag{1.16}$$

where $\bar{m}$ is the average mass of up and down quarks. If taking $\bar{m}$ = 6 MeV, then the vacuum of quark antiquark condensate is about $\langle 0 \left| \bar{q}q \right| 0 \rangle \approx (-250MeV)^3$ per light flavor. The non-zero vacuum spontaneously breaks the chiral symmetry of QCD. Since chiral symmetry is a global symmetry, its spontaneous breaking must be accompanied by (almost) massless Goldstone bosons. In case of two light quark flavors, the three charge states of the pion servers as the Goldstone bosons, with a mass (about 140 MeV) which is much smaller comparing to all the other hadrons. The assumption of spontaneously broken axial-vector symmetry also explains the large mass splitting between ρ and a_1 meson. Theory calculations predict that $m_{a_1} = \sqrt{2} m_\rho$ [18].

1.1.5 Deconfinement and QGP

Another important feature of QCD is confinement which lead to the absence of direct observation of isolated quarks and gluons in the experiment. The confinement is because gluons who carry the force have color charge and thus can interact with itself. Due to the property of the running QCD coupling constant α_s, when two quarks are separated from each other, the force between them grows stronger as the distance increasing. When the energy is enough, a new quark/anti-quark pair is created from the

vacuum. As result of this, the quarks and gluons are confined inside hadrons, and when quarks are created in high energy experiment, instead of seeing the individual quarks, only cluster of color neutral hadrons are observed. This process is called hadronization. On the other hand, when the system is at extreme temperature or high energy density, such like the universe in a few microsecond after the "Big Bang", due to the asymptotic freedom, the interaction between partons (quarks/anti-quarks and gluons) is very weak and the partons can travel over larger distances of the size of a nucleon (~1 fm). The quarks and gluons are deconfined and form a thermalized state known as Quark-Gluon Plasma (QGP) [19].

The lattice QCD calculations expect a phase transition from the hadronic phase into the QGP phase. The *Polyakov loop operator,*

$$L = \frac{1}{3}\mathrm{tr}\left(\mathcal{P}e^{ig\int_0^\beta A_4(x,\tau)d\tau}\right) \tag{1.17}$$

is believed as an observable for the phase transition. Figure 1.4 left panel shows the Polyakov loop operator expectation value $\langle L\rangle$ and its temperature derivative as a function of the lattice coupling $\beta = 6/g^2$. At small temperature, a vanishing thermal expectation value $\langle L\rangle$ of Polyakov loop operator indicates infinite energy for a free quark, or in another word, quark is confined. At high temperature, $\langle L\rangle$ increase rapidly to a nonzero value, its derivative shows a sharp peak at a critical coupling β_c. This indicates that quark is deconfined at the corresponding critical temperature T_c. Figure 1.5 shows the phase diagram of strongly interacting matter in temperature vs. baryon chemical potential plane (T, μ_B). The lattice QCD calculations tell us the phase transition alone the temperature axis (μ_B = 0), with a crossover transition from hadron resonance gas to a QGP phase at a temperature about 154 MeV. On other hand, QCD based models indicate that the crossover transition ends at a critical point at high μ_B and becomes first order transition [20, 21]. However, the locations of the phase boundary and the critical point in this framework depend on model assumptions. One of the main aim of high-energy heavy-ion collision experiments is to explore the QCD phase diagram, to locate the position of critical point, and to determine the QCD phase boundary.

1.1.6 Restoration of the chiral symmetry

Another feature of the hot and density strongly interacting matter is the restoration of the chiral symmetry. Considering the chiral quark-antiquark condensate $\langle\bar{\psi}\psi\rangle$, figure 1.4 right panel shows $\langle\bar{\psi}\psi\rangle$ and its temperature derivative as a function of the lattice coupling $\beta = 6/g^2$ (a value corresponding to the temperature). The nonvanish-

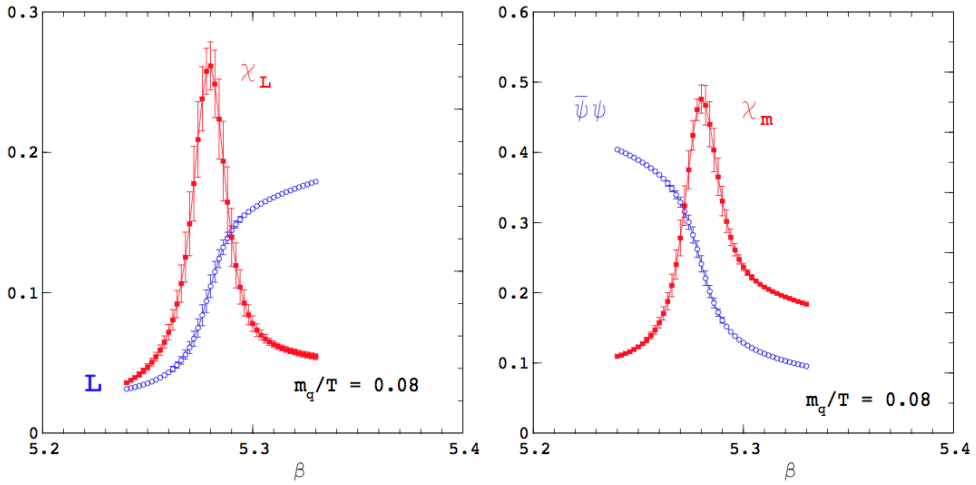

Figure 1.4 Left panel: the expectation value of Polyakov loop $\langle L \rangle$ and its temperature derivative (Polyakov loop susceptibility χ_L) as a function of the lattice coupling $\beta = 6/g^2$ which is related to the temperature T (larger β correspond to larger T). Right panel: the chiral condensate (the scalar quark density) $\langle \bar{\psi}\psi \rangle$ and the negative of its temperature derivative (chiral susceptibility χ_m) as a function of temperature. [6, 7]

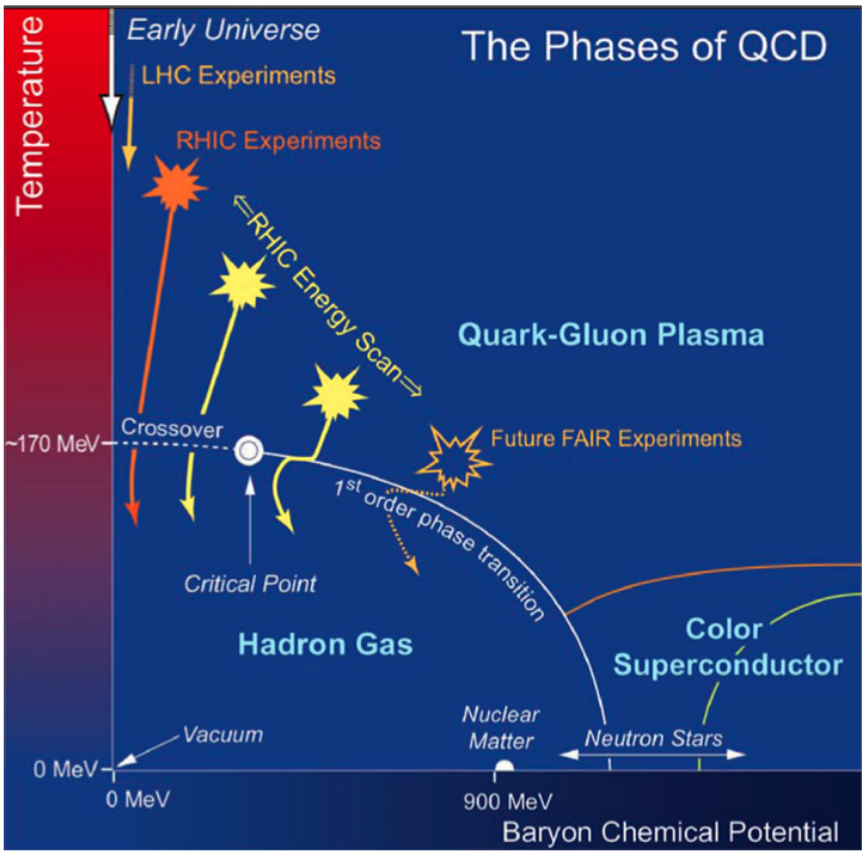

Figure 1.5 A conjectured QCD phase diagram with boundaries that define various states of QCD matter. [8]

ing chiral condensate at T = 0 spontaneously breaks the chiral symmetry and generates a dynamic mass of order 300 MeV for up and down quarks. With the temperature increasing, the dynamically generated mass melts away at T_c, and the quarks mass become vanishing again above T_c, or in another word, the approximate chiral symmetry is restored. Numerical computations of the lattice-discretized path integral for QCD at finite temperature predict chiral symmetry restoration to happen at a critical temperature of $T_c \approx 160 - 190$ MeV, corresponding to an energy density of about $\varepsilon_c \approx 1\text{GeV}/\text{fm}^3$ [22, 23]. Considering the quark component in real world (two light quarks u and d, and a much heavier strange quark s), this transition is more likely a rapid cross-over.

Chiral symmetry restoration can be characterized by the rapid decrease of the $\bar{q}q$ condensate, while in experiment, the key manifestations are its consequences for the hadron spectrum. Chiral partners must degenerate which lead to a massive medium modifications of hadronic spectral functions as the transition is approached. The ρ meson is a unique tool for characterizing the chiral properties of hot and density medium, since its life time is much short (~1.3 fm) than the medium (~10 fm) created in heavy energy heavy ion collisions. Its spectral function is expected to be significant modified (comparing to other light mesons) during the interaction with medium. There are two main scenarios on the in medium modification of the ρ meson. Brown and Rho suggests that the ρ-meson mass should drop to almost zero as a consequence of chiral symmetry restoration [24, 25]. Subsequently, more medium modifications of the ρ meson were investigated based on its rescattering on constituents of a hadronic medium, [26–29]. These calculations based on hadronic many-body interactions predict a strong broadening of the ρ spectral function, which when extrapolated to the putative phase transition temperature, leading to a complete "melting" of the resonance structure. Figure 1.6 right panel shows the scenarios for the effects of chiral symmetry restoration on the in-medium vector- and axial-vector spectral functions.

1.2 Dilepton production in high energy heavy ion collisions

The heavy ion collision is believed to be the best way to study properties of QCD matter in laboratory, since increasing the mass number of the incident particles is more efficient than increasing beam energy. During the past 20 years, world wide efforts have been dedicated in this region. Several large-scale experiments have been conducted. Relativistic heavy ion collider (RHIC) built in Brookhaven National Laboratory is the first accelerator-collider dedicated to heavy ion collisions. During the first few years of its operation, plenty measurements support the existence of a new matter form: a

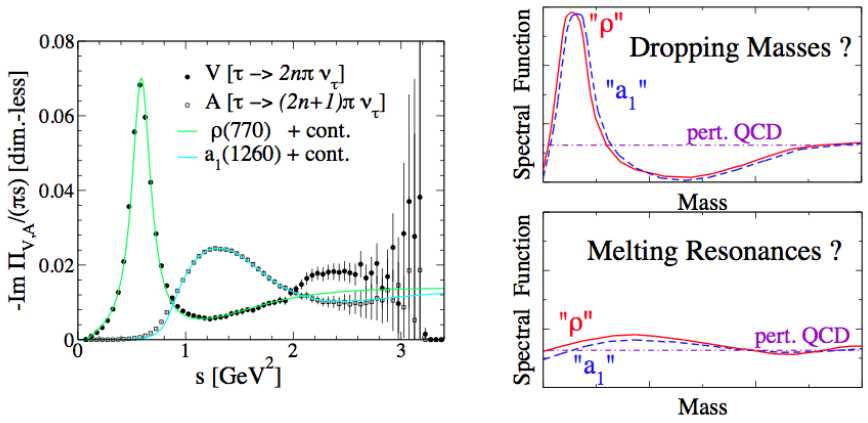

Figure 1.6 Left panel: vector and axial-vector spectral functions as measured in hadronic τ decay [9]. Right panel: scenarios for the effects of chiral symmetry restoration on the in-medium vector- and axial-vector spectral functions. Figure is taken from [10].

strongly coupling Quark Gluon Plasma (sQGP). Currently the physics program at RHIC was changing to studying the property of strongly interacting matter created in high energy heavy ion collisions and searching for phase boundary and critical point of the QGP phase diagram. At CERN, the Large Hadron Collider (LHC) also contributes in the heavy ion collisions program. It is pushing the colliding energy up to 5.5 TeV, where the energy density and temperature is much higher than the requirement of QGP formation.

Probes explored in experiments are mostly hadrons which have been used to demonstrate the formation of a strongly-coupled Quark Gluon Plasma (sQGP) in high energy heavy ion collision at RHIC and LHC. Dileptons as an electromagnetic probe, escape the interacting system without suffering further strong interactions after production. In addition, dilepton can be produced on the various stages of entire system evolution. They are therefore expected to be an outstanding probes to study the property of the medium created in high energy heavy ion collisions.

Traditionally, due to different physics of interest, the dilepton kinematic phase space is divided into the Low Mass Region - LMR ($M_{ll} < M_{\phi}$), the Intermediate Mass Region - IMR ($M_{\phi} < M_{ll} < M_{J/\psi}$) and the High Mass Region - HMR ($M_{ll} > M_{J/\psi}$).

At the initial stage of the system, the initial hard pQCD process Drell-Yan production ($q\bar{q} \rightarrow l^{+}l^{-}$) can produce high mass dilepton and is thus expected to dominate in the HMR. Moreover, direct photons from the initial hard scattering can allow for bremsstrahlung emission of soft virtual photons which convert into low mass and high transverse momentum (p_T) dielectrons ("internal conversion"). These dilepton, in principle, can be calculated within the pQCD frame.

The system is expected to quickly reach the partonic sQGP phase where dileptons

can be produced in thermal radiation via multiple parton-parton scattering. Theoretical calculations suggest that at top RHIC energy, QGP thermal dilepton production will become dominant in the IMR while thermal dileptons with higher masses originate from earlier stages [30]. This indicates that investigating the thermal dilepton production in M_{ll} & p_T allows for probing the medium properties at different stages of the space-time evolution. Measuring thermal dilepton collective flow and polarization can reveal information about the degrees of freedom of deconfinement and equilibrium of the strongly interacting matter created in heavy ion collisions[31–33]. Thermal radiation can produce real photons accompanied by low mass and high p_T dileptons. Study of these dileptons compared to that from initial hard scattering, one can learn the direct real photon production from the thermal QGP medium.

As the fire ball expands and cools, the system enters the hadronic phase. Dileptons emitted from the hadronic medium are governed by the coupling of vector mesons (ρ, ω, ϕ etc) to the medium via hadron-hadron interaction and are expected to dominate LMR production [26]. Their mass spectra are determined by the chiral properties of QCD which is spontaneously broken in vacuum. Theoretical calculations suggest that the vector meson spectral functions will be modified in the hot and dense hadronic medium, which may be connected to the restoration of chiral symmetry. Among them, the ρ meson is expected to be most modified, due to its short life time ~ 1.3 fm comparing to the life time of hadronic medium (~ 10 fm) [34]. Two scenarios have been proposed for the change of vector meson spectral functions when chiral symmetry is restored: a shift of the pole mass [25] and a broadening of the mass spectral function [35]. Measurements of dielectron continuum in the low mass region will shed light on the vector meson production mechanism, and hence the medium chiral properties in heavy ion collisions.

Finally, when all particles decouple from the system long-lived π^0, η, $D\bar{D}$ etc. can decay into lepton pairs and be measured by the detector system. Their contributions can be calculated based on the measured or predicted invariant yields of parent mesons. Usually, their contributions are called hadronic decay cocktail.

1.3 Previous experiments and measurements

Dilepton measurements in heavy ion collisions have been pursued for decades in different collision system from low to relativistic energies[2, 11–13, 36–42]. In this section, I will make a brief review of several important experiment measurements from SPS and RHIC.

1.3.1 CERES/NA45

NA45 is a fixed-target heavy ion collisions experiment at the CERN Super Proton Synchrotron (SPS). It is also well known by the name of the detector - Cherenkov Ring Electron Spectrometer (CERES). A detailed description of the CERES/NA45 experiment can be found in [43].

Figure 1.7 shows the dielectron mass spectra measured by CERES in different collision system. In p-A collisions (p-Be, p-Au at 450 AGeV) the production of dielectron can be well explained by the hadronic cocktail simulations [11]. The results from the S-Au collision system, however, show a statistically significant enhancement w.r.t the hadronic cocktail simulations. Further measurements in 40 and 158 AGeV Pb-Au collisions show similar results [12, 44]. The centrality and transverse momentum dependence of the enhancement was studied in Pb-Au collision at 158 AGeV. The experiment results demonstrates that the enhancement is mostly in low p_T region and shows a strong centrality dependence. The observation of the enhancement has risen great interests among theorists. A common agreement is that one observes direct thermal radiation from the fireball, dominated by two pion annihilation $\pi^+\pi^- \rightarrow \rho \rightarrow e^+e^-$ with an intermediate ρ vector meson. Due to the short life time and its direct connect to the chiral symmetry restoration, the ρ is expected to be significant modified (comparing to ω and ϕ) in the hot and dense medium. And there are two main theoretical alternatives to describe the modification: 1) "Brown-Rho scaling" which is directly connected to the chiral symmetry properties of the medium, which lead to a dropping of the ρ pole mass comparing to the vacuum value; 2) the multi-scattering with hadrons in medium, spreading the width of the ρ spectra function. The experiment results in Pb-Au collision at 40 AGeV (shown in Fig 1.8) clearly role out the vacuum unmodified ρ. The data agrees with the two in-medium scenarios, however, due to limited statistics, it fails to distinguish between them.

1.3.2 NA60

NA60 is another experiment on SPS at CERN. It inherited the muon spectrometer and zero degree calorimeter from NA50 and equipped with a high-granularity silicon pixel telescope vertex detector. NA60 is a muon detector and measured the dimuon spectra which don't have large background contributed from Dalitz decay from π^0. Benefited from the new vertex detectors, NA60 can identify the offset of the muon tracks with respect to the collision vertex. The dimuon contributed from charmed meson decay thus can be separated from prompt muon pairs.

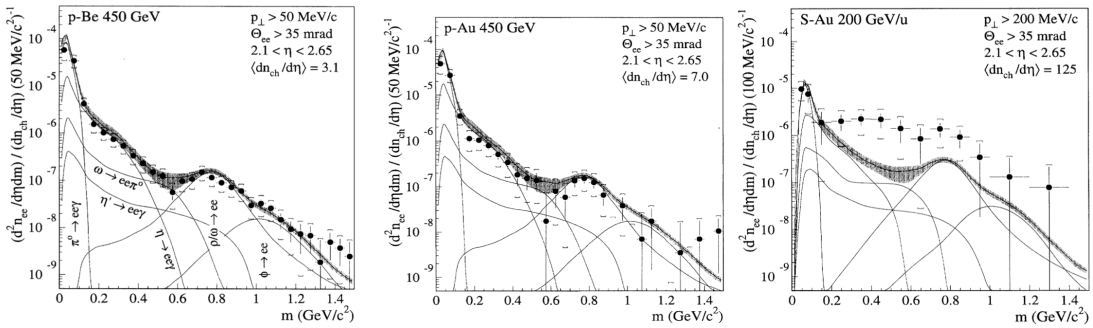

Figure 1.7 Inclusive e^+e^- mass spectra in 450 GeV p-Be collisions (left), p-Au collisions (middle), and 200GeV/nucleon S-Au collisions from CERES/NA45 experiments [11].

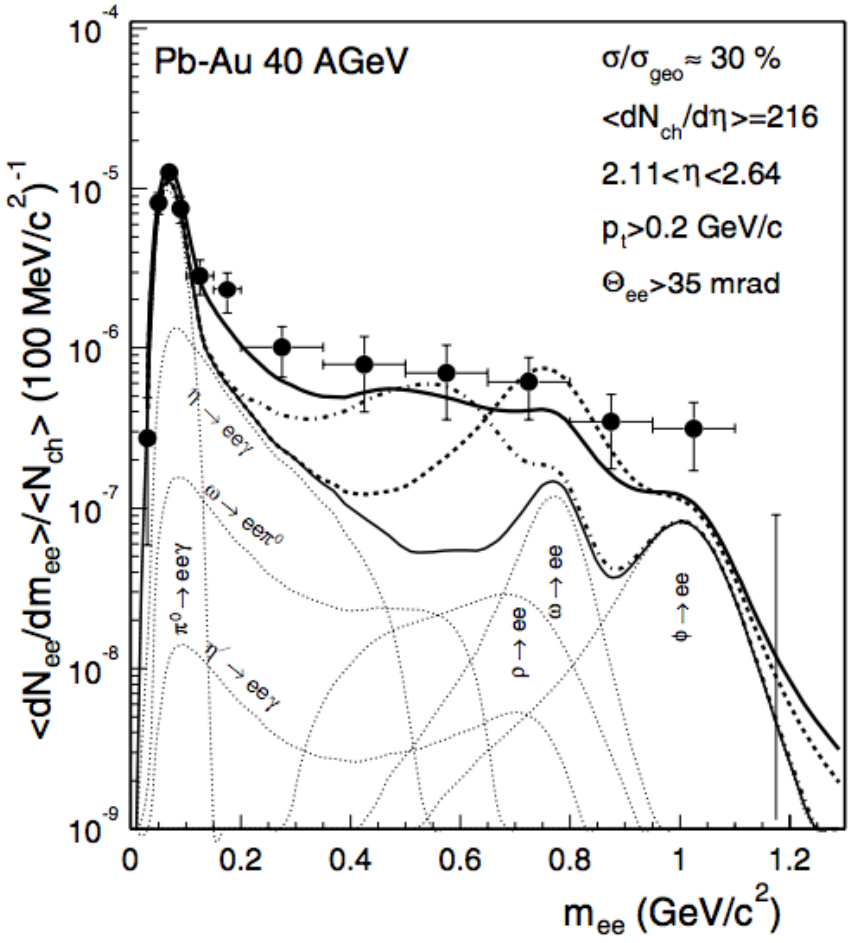

Figure 1.8 Inclusive dielectron mass spectrum, compared to the hadron decay cocktail (thin solid; individual contributions thin dotted) and to theoretical model calculations: vacuum unmodified ρ (thick dashed); in-medium dropping ρ mass (thick dash-dotted); in-medium broadening ρ width ((thick solid). [12]

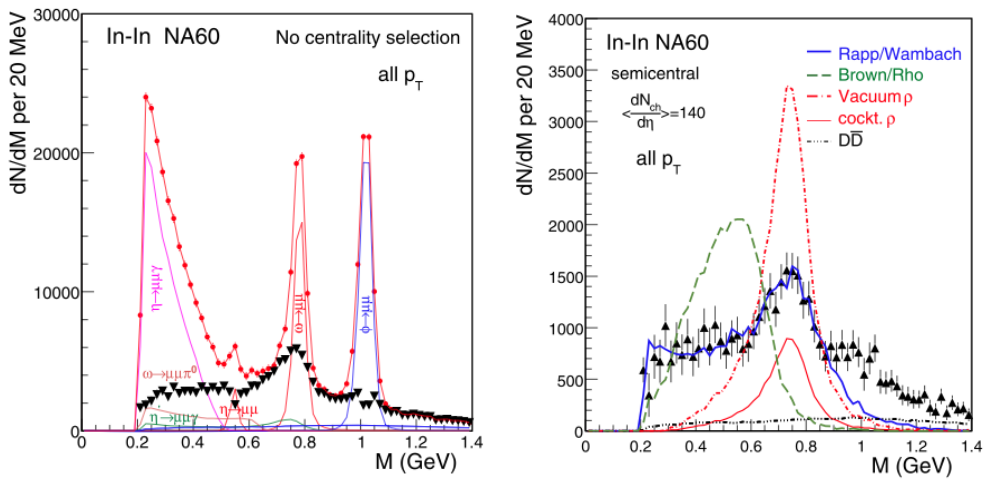

Figure 1.9 (Left) Background-subtracted mass spectrum before (dots) and after subtraction of the known decay sources (triangles). (Right) Excess dimuons compared to theoretical predictions, renormalized to the data in the mass interval M < 0.9 GeV. [13]

Figure 1.9 left panel shows the centrality-integrated dimuon measurement from NA60 In-In collisions at 158 AGeV. The high data quality allows to isolate the dimuon excess from total data by subtracting the hadronic cocktail from the known decay sources. All hadron source except ρ are included in the cocktail simulation. The excess results are compared with the in medium modified ρ model calculations. The high precision data role out the vacuum ρ and dropping ρ pole mass scenarios [45], and the broadening model [26] can explain the data very well.

Another important results from NA60 are shown in Fig 1.10. The inverse slope parameters T_{eff} of the m_T spectra are plotted as a function of dimuon mass in the right panel. In low mass region ($M_{ll} < 1GeV/c^2$), T_{eff} shows a monotonic rise with mass towards to the ρ pole mass, which is a strong indication for radial flow of a hadronic source. The measurements from hadrons also confirms this conclusion. Around the ϕ mass, the T_{eff} distribution shows a sudden drop about 50 MeV. This provides a first indication of thermal leptons from a partonic source as argued by the NA60 collaboration [42]. In the left panel of Fig 1.10, Acceptance-corrected invariant mass spectrum of the excess dimuons are compared with three sets of thermal model results [46–48], which provide further support of the conclusion of the transition from hadronic source to partonic source from low mass to intermediate mass. In the region above 1 GeV, all three models explicitly differentiate between partonic and hadronic processes. In case of [46, 48], partonic source dominate and can full describe the data up to 2.5 GeV.

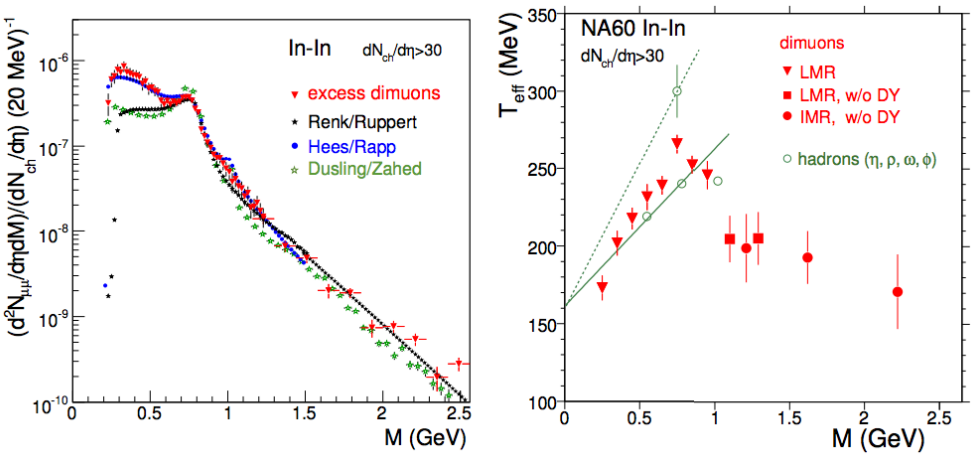

Figure 1.10 Left Panel: Acceptance-corrected invariant mass spectrum of the excess dimuons, comparing with three different sets of thermal-model calculations. Right Panel: Inverse slope parameter T_{eff} of the m_T spectra as a function of dimuon mass. Charm contribution is removed. Hadron results are shown for comparison. Figures are taken from [14].

1.3.3 PHENIX

PHENIX (Pioneering High Energy Nuclear Interaction Experiment) is one of the two major detector system at RHIC. It is designed to mainly study leptons and photons production from heavy ion collisions. The PHENIX system consists of two central arm spectrometers, each arm covers the pseudo-rapidity range $|\eta| < 0.35$ and an azimuthal angle of $\pi/2$. The PHENIX collaboration reports the measurements of inclusive mass spectrum of e^+e^- pairs in p+p collision and Au+Au collisions at $\sqrt{s}$ = 200 GeV, which are shown in Fig 1.11. The e^+e^- mass spectra in p+p collision can be describe by the hadronic cocktail simulation, while, the results from Au+Au collision shows huge enhancement in LMR when comparing to the hadronic cocktail. The integral enhancement observed in Au+Au collision is $4.7 \pm 0.4(stat.) \pm 1.5(sys.)$[2] in mass region 0.15~0.75 GeV/c^2. The LMR excess in 200 GeV Au+Au collisions are also compared with in-medium model calculations in Fig 1.12, however none of them can explain the large enhancement.

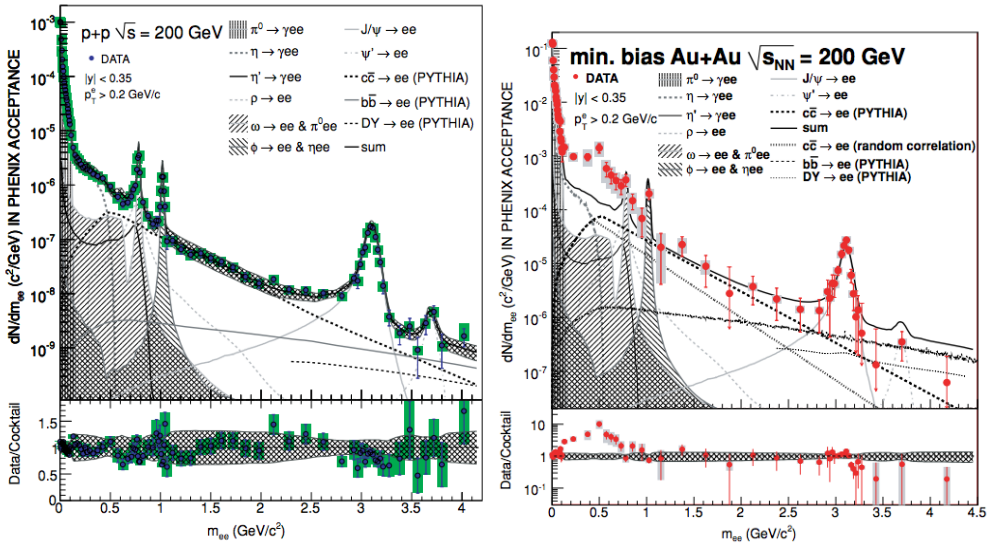

Figure 1.11 Inclusive mass spectrum of e^+e^- pairs in the PHENIX acceptance in minimum-bias p+p collision (left) and Au+Au collisions (right) at $\sqrt{s}$ = 200 GeV. [2]

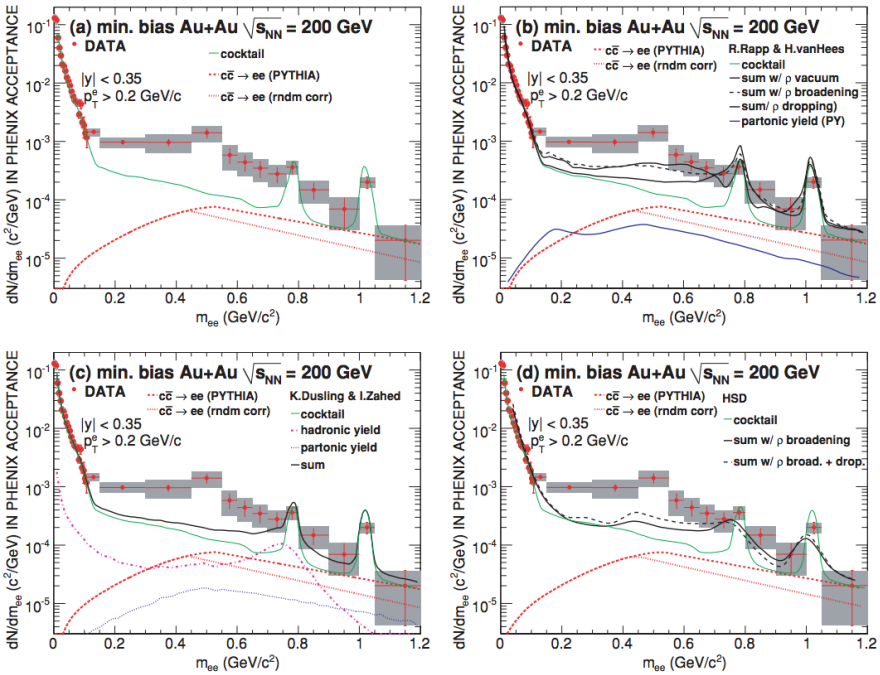

Figure 1.12 Invariant mass spectra of e+e− pairs in Au+Au collisions in the LMR. The data are compared to hadronic cocktail (left upper) and three model calculations. [2]

Chapter 2 Experiment set-up and detectors

2.1 The Relativistic Heavy Ion Collider

The Relativistic Heavy Ion Collider (RHIC) at Brookhaven Nation Laboratory (BNL) was built at year 1999, after nine years construction. It is deigned to accelerate and collide heavy ions and polarized protons at relativistic energy. RHIC has capabilities to deliver beams ranged from proton to uranium with high luminosity. The top center-of-mass collision energy is 200 GeV per nucleon pair for heavy ion collisions and 500 GeV for polarized p+p collisions. The basic design parameters of the collider are listed in Table 2.1. The main physics goal of RHIC is to investigate the phase transition from hadronic phase to QGP phase and to study the formation and property of QGP. RHIC also provides polarized p+p collision with collision energy up to 500 GeV to expand the scientific objective of RHIC to include vigorous spin physics program.

Figure 2.1 shows the layout of RHIC complex with the injector chain and the ring tunnel. The RHIC complex contains the Tandem van de Graaff pre-accelerator, a linear proton accelerator, the Booster Synchrotron, the Alternating Gradient Synchrotron (AGS) and and ultimately the RHIC synchrotron ring. The acceleration scenario for gold ion beams is shown in Fig. 2.2. Negatively charged ($Q_T = -1$) Au ions is injected into the Tandem Van de Graaff from the Pulsed Sputter Ion Source. They are partially stripped of their electrons and accelerated inside the Tandem Van de Graaff and exit with the energy of 1 MeV/nucleon and charge state of $Q_T = +32$. The ions are delivered to the Booster Synchrotron and accelerated to 95 MeV/nucleon and further stripped to $Q_T = +77$ at the exit. Then they are transferred into the AGS, where they are accelerated to 8.86 GeV/nucleon and sorted into four final bunches. Ions are fully stripped ($Q_T = +79$) at the exit of the AGS and transported to the RHIC storage rings though the AtR beamline. RHIC also has capability to provide polarized proton beams. Protons are injected from the 200 MeV Linac into the booster, followed by acceleration in the AGS and injection into RHIC.

RHIC has two concentric super-conducting accelerator/storage rings, one ("Blue Ring") for clockwise and the other ("Yellow Ring") for anti-clockwise beams. They are on a common horizontal plane in the tunnel with a circumference about 38 km. Each ring consists of six insertion sections with collision point at their center along its

	For Au+Au	For p+p
Beam energy	→100 GeV/nucleon	30→250 GeV
Luminosity	$2 \times 10^{26} cm^{-2} s^{-1}$	$1.4 \times 10^{31} cm^{-2} s^{-1}$
Number of Bunches/ring	60(→120)	60(→120)
Luminosity lifetime	~ 10 hours	~ 10 hoours

Table 2.1 Performance specifications of RHIC [4].

circumference. Two major experiments STAR and PHENIX are located at 6 o'clock and 8 o'clock, and two minor ones PHOBOS and BRAHMS were located at 10 o'clock and 2 o'clock, respectively. To date, RHIC has been configured to run in p+p, d+Au, Au+Au, Cu+Cu, Cu+Au and U+U collisions.

2.2 STAR experiment

The Solenoidal Tracker at RHIC (STAR) is one of the two large detecter systems constructed at RHIC. Heavy ion collision at RHIC creates a nuclear environment of a large produced particles (up to approximately 1000 per unit pseudo-rapidity) and high momentum particles from hard parton-parton scattering. The main physics goal of the STAR experiment is to measure many observables simultaneously to investigate the signatures of a possible QGP phase transition and to understand the space-time evolution of the collision process in ultra-relativistic heavy ion collisions. In order to accomplish this, STAR was designed primarily for measurements of hadron production over a large solid angle. The STAR detector systems are very effective in high precision tracking, momentum analysis, and particle identification at the central rapidity region. With the installation of the Time Of Flight detector (TOF) in 2009, STAR gained the capability to identify electrons and positions.

STAR has an azimuthal symmetric acceptance and covers large range around mid-rapidity ($|\eta|$<1, 2π azimuthal coverage). Figure 2.3 shows the layout of the STAR detector systems alone with the subsystems.

Close to the beam pipe is the Heavy Flavor Tracker (HFT) which is a new detector add in the STAR detector systems in 2014. The HFT is designed to measure the heavy flavor production by the measurement of displaced vertices and to do the direct topological identification of open charm hadrons. The Time Projection Chamber (TPC) is the main tracker at STAR which has a coverage of $|\eta|$<1 and 2π in azimuthal direction. The Time Of Flight (TOF) detector is surrounding the TPC which has also a coverage

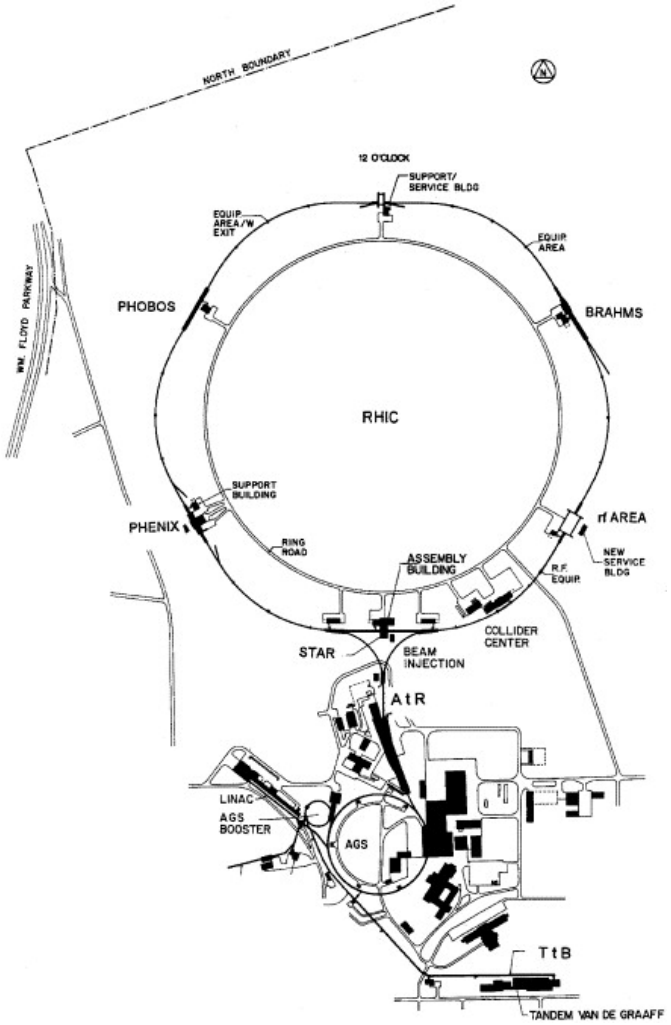

Figure 2.1 The layout of RHIC complex[15].

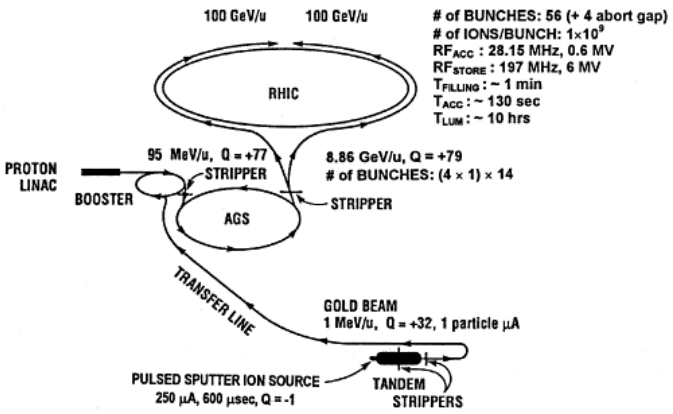

Figure 2.2 Acceleration scenario for gold ions[4].

$|\eta|$<1 and 2π in azimuthal direction. The Barrel Electro-Magnetic Calorimeter (BEMC) located outside of the TOF and covers $|\eta| < 1$ with complete azimuthal symmetry. The Endcap Electro-Magnetic Calorimeter (EEMC) covers for 1 < |η| < 2, over the full azimuthal range. The EMCs are used to distinguish high momentum single photons from photon pairs of π and η meson decays and electrons from charged hadrons. Outside the BEMC is the magnet system which provides a uniform magnetic field parallel to the beam direction and together with BEMC it also servers as the electron and hadron absorber for the Muon Telescope Detector (MTD). The MTD is also a new added detector, which is installed in 2014. It is designed to detect high p_T muon for heavy flavor collectivity and production.

Along the beam pipe, there are some trigger detectors: Zero Degree Calorimeter (ZDC), Vertex Position Detector (VPD) and Beam-Beam Counter (BBC). Two ZDCs locates on each side ~ 18 m away from the collision point. The ZDCs are designed as hadronic calorimeters to detect the outgoing neutrons. Dipole magnets are put before the ZDC detectors to bend away the charged fragments. The ZDC signals are used for monitoring the heavy ion beam luminosity and for the experiments triggers. The BBC subsystem covers $3.3 < |\eta| < 5.0$ and consists of two disk shaped scintillating detectors. They are placed at the endcaps of the TPC (3.5 m from TPC center). Each BBC disk is made up of close packed hexagonal scintillator tiles in two rings. A BBC trigger corresponds to a prompt coincidence between at least one (out of eighteen total) tile firing in both BBC EAST and BBC WEST within a time window. This BBC trigger defines a minimum bias trigger corresponding to a p-p cross section of ≈ 26 mb, 87% of the p-p Non-Singly Diffractive (NSD) inelastic cross section. The VPD detector has two assembly which consists of two rings of readout detectors (19 channels). The two assemblies are mounted symmetrically with respect to the center of STAR at a distance of 5.7 m and cover $4.24 \leq \eta \leq 5.1$. The signals from VPD are used to select minimum bias collisions, to constrain the location of the primary collision vertex along the beam pipe and to provide start time for STAR fast timing detectors. EMCs is also used to trigger on high p_T particle events.

The detectors involved in this analysis will be introduced in detail in follow sections.

2.2.1 STAR magnet system

The STAR magnet system [49] is a room temperature solenoidal magnet which was designed as a cylinder with a length of 6.85 m and has inner and outer diameter of

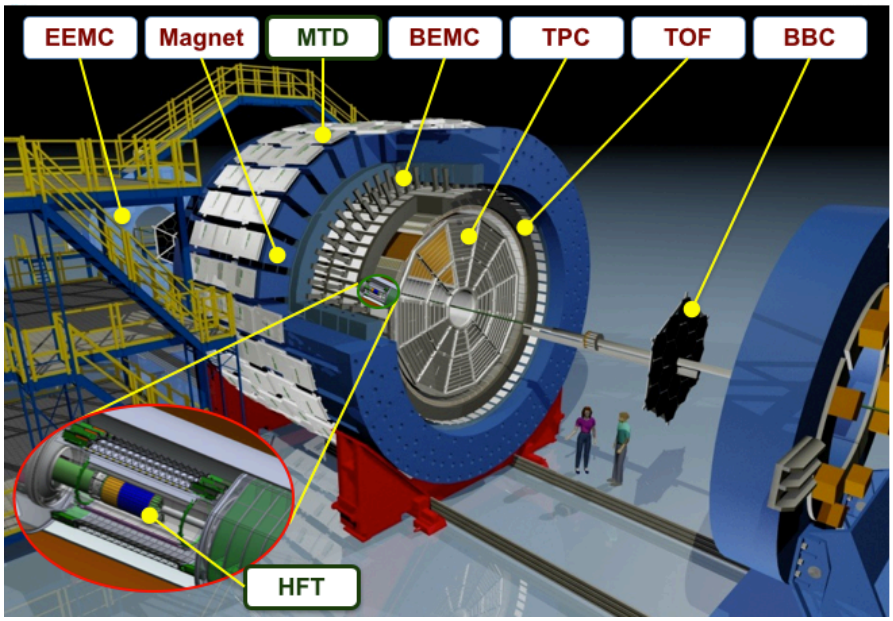

Figure 2.3 The STAR detectors. HFT and MTD are new added detectors and were fully installed in 2014.

5.27 m and 7.32 m, respectively. It provides an uniform magnetic field which parallels to the beam direction (Z direction) with a maximum value 0.5 T for charged particle momentum analysis. STAR magnet can work under full field (+0.5 T), reversed full field (-0.5 T) and half field configuration ($\pm$0.25 T).

2.2.2 Main tracker - Time Projection Chamber

The Time Projection Chamber (TPC) is the primary tracking detector and the heart of STAR detector system. The TPC was designed to record the tracks of particles, measure their momenta, and provide particle identification by measuring their ionization energy loss (*dE/dx*). It has a large acceptance around middle rapidity ($|\eta| < 1.8$) and full azimuthal coverage.

Figure 2.4 shows the STAR TPC. It was built as a cylinder with a length of 4.2 m and outer diameter of 4 m and inner diameter of 1 m. TPC was installed inside the STAR magnet system which provides a 0.5 T uniform magnetic field. The beam pipe which is alone the Z direction goes through the center axis of TPC and concentric with TPC. The collisions happens in side the beam pipe near the center of TPC.

Inside the TPC, it is an empty volume which is filled with P10 gas (10% methane, 90% argon) regulated at 2 mbar above atmospheric pressure. There is a well defined, uniform, electric field of $\approx$135 V/cm in the volume serve as the drift field. The primary advantage of P10 gas is that electrons has a fast drift velocity which peaks at a low

electric field which makes the drift velocity stable and insensitive to small changes in temperature and pressure. The uniform drift field in TPC is defined by a thin conductive Central Membrane (CM) at the center of the TPC, concentric field-cage cylinders and the readout end caps [16]. The central membrane is operated at 28 kV and the end caps are at ground. The typical drift velocity of electrons in the STAR TPC is 5.45 cm/μs. The transverse diffusion is 230 $\mu m/\sqrt{cm}$ and the longitudinal diffusion is 360 $\mu m/\sqrt{cm}$ with 140V/cm drift field and 0.5 T magnetic field.

The STAR TPC's readout system is based on Multi-Wire Proportional Chambers (MWPC) with readout pads. The readout planes are arranged as on a clock with 12 sectors around the circle at each end of TPC. The readout system includes four components: a pad plane and three wire planes, shown in Fig. 2.5. The anode wire plane of 20 μm wires with the pad plane on one side and the ground wire plane on the other composes the amplification readout layer. It can provide an amplification of 1000 to 3000 while the drifting electrons avalanche in the high fields. Figure 2.6 shows the anode pad plane with one full sector. To optimize the *dE/dx* resolution, the outer sector was designed to have continuous pad coverage. This setup can improve statistics on the *dE/dx* measurement because the full track ionization signal is collected with more ionization electrons. The inner sub sectors are in the region of highest track density. The design of inner pads is optimized for good two-hit resolution by using smaller pads with separate pad rows instead of continuous pad coverage. The third wire plane is a gating grid which is a gate to control electrons from TPC drift volume to MWPC. It also stops the positive ions inside MWPC from entering the drift volume to preserve the uniform drift field [50].

When the charged particles travel through the gas volume, they liberate electrons from the gas molecules due to ionization energy loss. The released secondary electrons drift under the drift field to the ends of TPC and collected by the readout system. The signals then are digitalized and transmitted to STAR Data AcQuistion system (DAQ). These raw signals (ADC and TDC) are reconstructed into 3D position informations of the ionization (hit positions) by a Kalman filte with a typical resolution 0.5~1.0 mm. The tracks of particles are reconstructed with high precision from these hits informations in 3 dimension by Time Projection chamber Tracker (TPT) algorithm. These tracks are combined with other available tracking detector's results and refit by a Kalman filter routine. Then the primary collision vertex is reconstructed from these global tracks. The primary vertex resolution is ~ 350 μm with more than 1000 tracks. Furthermore, tracks with the *distance of closest approach* (dca) to the primary vertex less then 3 cm is refitted by forcing the track to originate from the primary vertex, these tracks are called

primary tracks which has improved resolution in position and momentum due to the relatively high precision of primary vertex. The reconstruction efficiency including the detector acceptance for primary tracks depends on the particle type, track quality cuts, p_T, track multiplicity etc. The typical value for the primary pions with N_{fit} > 24 and $|\eta|$ < 0.7, dca < 3.0 cm is approximate constant at p_T > 0.4 GeV/c: $>\sim$ 90% for Au + Au peripheral collisions and ~ 80% for central collisions, respectively.

With the collected ionization energy loss (*dE/dx*) information, TPC also provides capability for particle identification. The mean rate of *dE/dx* is given by the Bethe-Bloch equation 2.1 [51]:

$$-\frac{dE}{dx} = Kz^2\frac{Z}{A}\frac{1}{\beta^2}\left[\frac{1}{2}\ln\frac{2m_ec^2\beta^2\gamma^2T_{max}}{I^2} - \beta^2 - \frac{\delta}{2}\right] \tag{2.1}$$

and furthermore optimized by the Bichsel functions [52]. For each track, *dE/dx* is extracted from the deposit charge collected on the pad rows up to 45. Energy loss of a charged particle for a given track length can be described by the Bichsel function [52]. However, the mean of the distribution is sensitive to the fluctuations in the tail of the distribution. Therefore, the most probable *dE/dx* is measured by removing the highest 30% of the measured clusters. Figure 2.7 shows the 70% truncated mean dE/dx distribution as well as the expectation from Bichsel functions. Clearly the energy loss is different corresponding to different particle species at the same momentum. In Au+Au 200 GeV collision, STAR can separate π and K up to ~ 0.7 GeV/c and identify proton up to ~ 1.1 GeV/c.

***dE/dx* calibration** is performed for each run setups respect to collision type, collision energy and magnetic field. The calibration is done with a specified data sample selected by following requirement:

- Good clusters : used in track fit, without overlaps.
- Good global tracks : with track length in TPC > 20 (or 40) cm.
- Tracks with 0.4 < p < 0.5 GeV/c (~MIP for pions: $\beta\gamma = p/m = 4$) where π can be well separated from other particles and the $\beta\gamma$ dependence of *dE/dx* is completely defined by Bichsel model.

The dE/dx calibration process contains a lot of corrections due to the energy loss in TPC is influenced by many factors, but usually it can be separated into three step: a over all correction of gas gains for sectors and rows; correction for gas pressure dependence; correction of track length. A value *Z* is defined as flowing:

$$Z_\pi = log\left(\frac{dE/dx_{measure}}{dE/dx^{\pi}_{Bichsel}}\right) \tag{2.2}$$

Where $dE/dx^{\pi}_{Bichsel}$ is the predicted for π from Bichsel model. The Z_π distributions are parameterized by a 5 gaussians fit with respect to mean position (μ) and width (σ) of π, which contain contribution from π, K, p, d and e. The relative positions of other particles to π are fixed. And the position (μ) of π defines the calibration correction. The correction parameters are defined which provide condition: $\mu = 0$ and variation is within 1% level. Figure 2.8 shows an example of the 5 gaussians fit for sector 24 row 40 in Run11 p+p 500 GeV collisions. The calibration is separated into 4 passes:

1. pass 0: Gas gain correction for sector/row. The Z_π distributions are parameterized in each sector and row. The correction is defined to direction shift μ to 0 for each sector and row which generates a correction table. Figure 2.9 shows the variation vs Sector and Row before correction (before) and after correction (after).

2. pass 1: Dependence of gas gain on gas density due to pressure. Figure 2.10 shows the dE/dx variation vs gas pressure before and after the correction. A linear fit is used to parameterize pressure dependence of dE/dx variation and to define the correction.

3. pass 2: Dependence of the truncated mean for track's *dE/dx* and its relative error versus track length in TPC. Figure 2.11 shows the track length dependence before correction and after correction. Usually a polynomial function is used to define the correction.

4. pass 3: Final pass to check the calibration results.

The corrections are not independent with each other, so after each new pass, the results for previous correction need to be checked. If the variation is larger than 1%, another pass is need to redone previous correction. Figure 2.12 shows the procedure of *dE/dx* calibration. The requirement for dE/dx resolution achievable with our calibration procedure has been set as 7.5% for tracks with length in TPC equal to 76.2 cm. Here take the calibration for p+p 500GeV in Run11 as an example, without any correction the *dE/dx* resolution for tracks with 76.3 cm length in TPC is 7.73% and the one with all corrections is 6.82% (Fig 2.13).

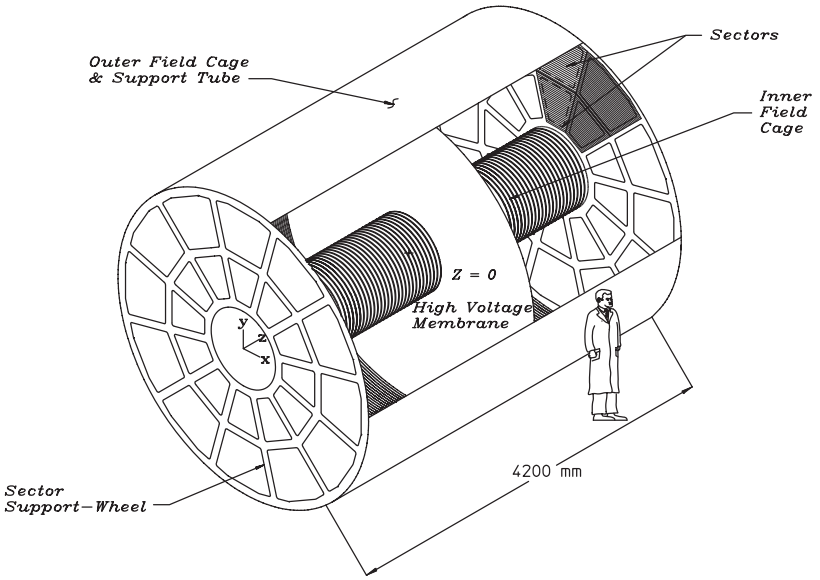

Figure 2.4 The STAR Time Projection Chamber (TPC) [16].

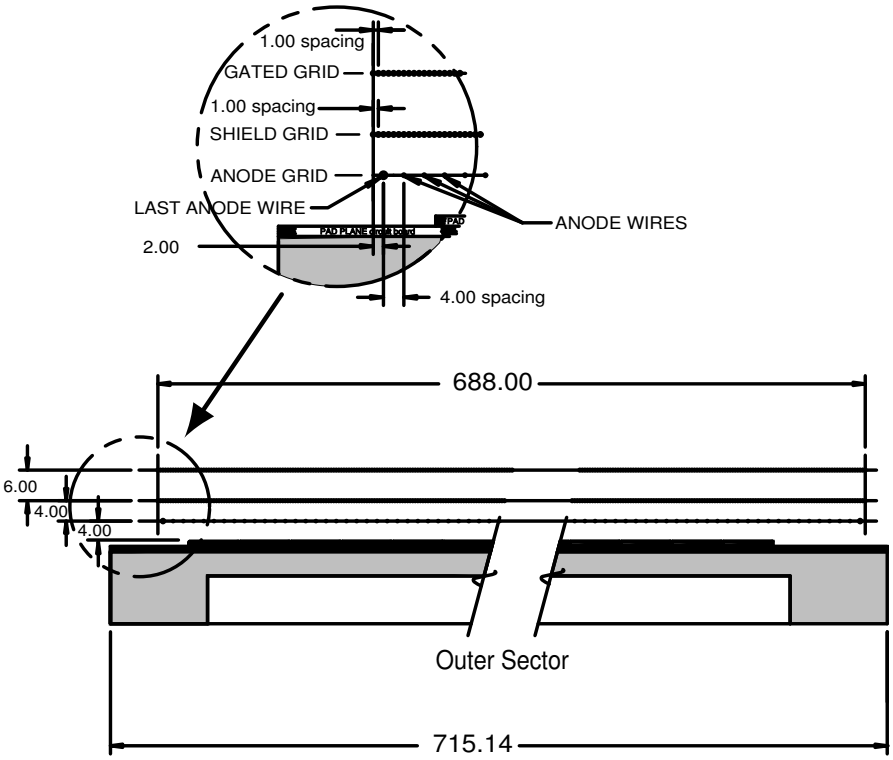

Figure 2.5

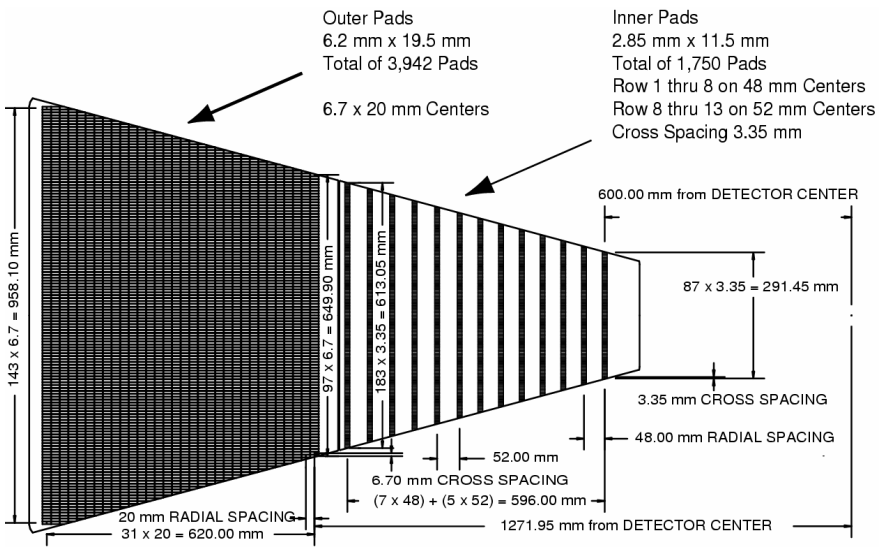

Figure 2.6 The anode pad plane with one full sector.

2.2.3 Time Of Flight system

The Time of Flight System (TOF) is another important set of detectors used in this analysis. The TOF system is designed to measure the flight time of charged particles. Combining with path length of tracks reconstructed by TPC, it can provide the velocity of the charge particles which is used to identify charged particles. In Fig. 2.7, the *dE/dx* binds of different particles cross with each other in some momentum regions where they can not be separated by using *dE/dx* only. With the installation of TOF, these holes are covered by adding the flight velocity into the PID criteria. Therefore, TOF greatly improves the PID capability of STAR and makes the identification of electron and position from the hadron background possible for the STAR detector system.

The TOF consists of the barrel Time Of Flight detector (bTOF) [**?**] and the the Vertex Position Detector (VPD). The bTOF is surrounding the TPC and measures the "stop" time (the time charged particle reach bTOF). The pVPD consists of two identical detector assemblies that are positioned very close to the beam pipe and outside the STAR magnet. It measures the start time (the time when the collision happens).

The bTOF is based on the Multi-gap Resistive Plate Chamber (MRPC) technology which is first developed by the CERN ALICE group [53]. MRPC technology is capable to provide the necessary timing resolution with a relative low cost. Figure 2.14 shows the side view of an MRPC module appropriate for STAR. Basically, the MRPC is a stack of resistive plates arranged in parallel. These plates are separated by nylon fishing line and form a series of uniform gas gaps with a width of 0.22 mm. The internal resistive plates are 20 cm long and 6.1 cm wide and 0.54 mm thick, which has a resist of $8 \times 10^{12}\ \Omega \cdot cm$.

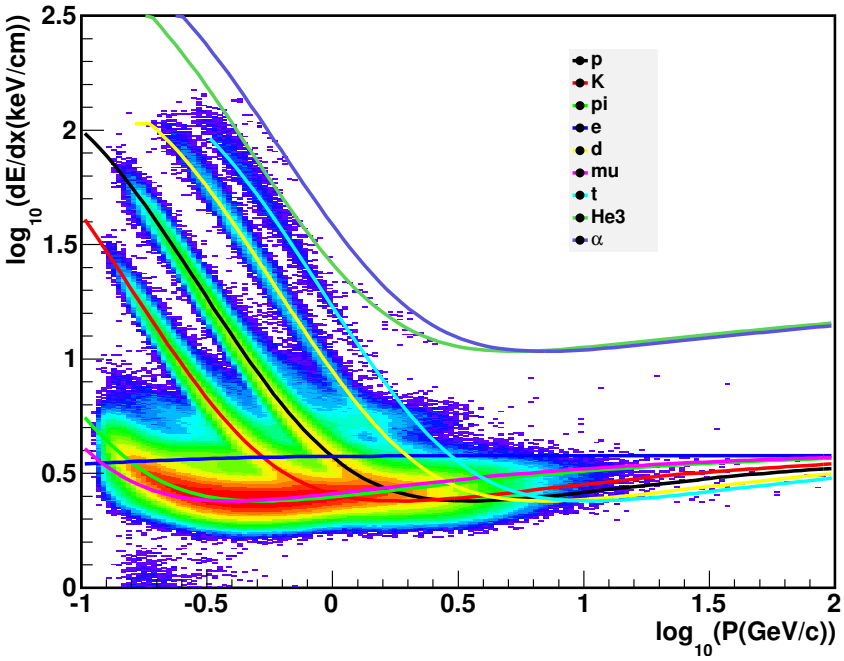

Figure 2.7 Distribution of *dE/dx* as a function of momentum. The Bishcel functions are also shown for difference particle species.

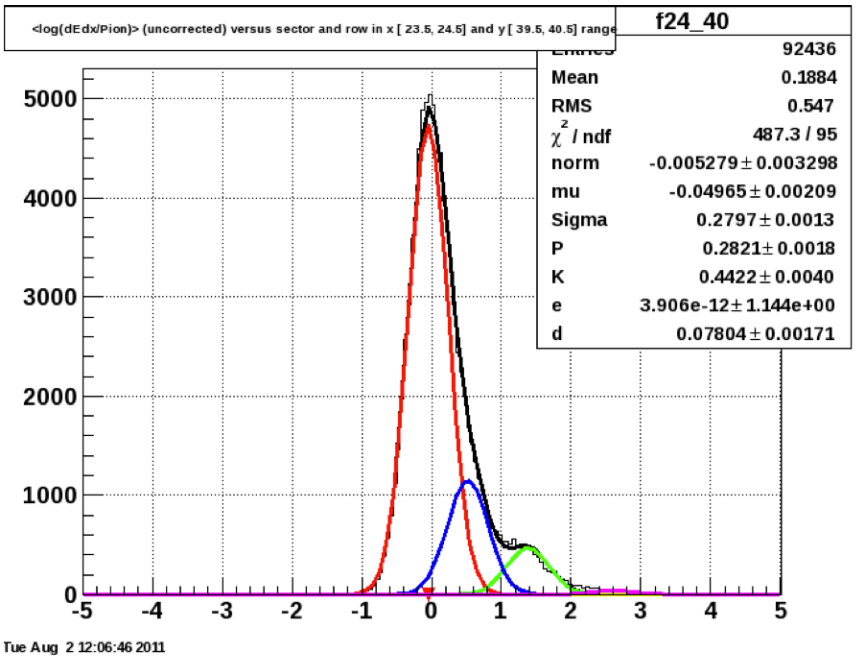

Figure 2.8 Fit for sector 24 row 40.

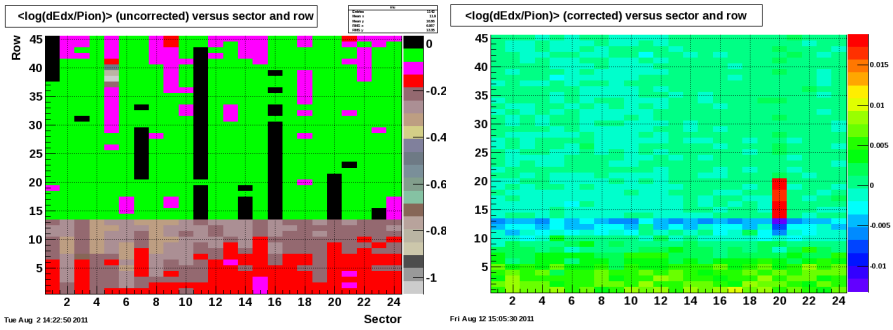

Figure 2.9 Variation vs Sector and Row before SectorRow correction (left) and after correction (right).

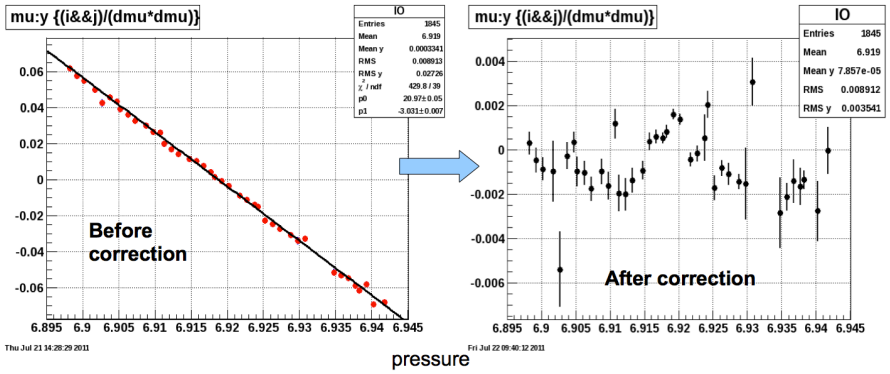

Figure 2.10 Variation vs gas pressure before correction (left) and after correction (right).

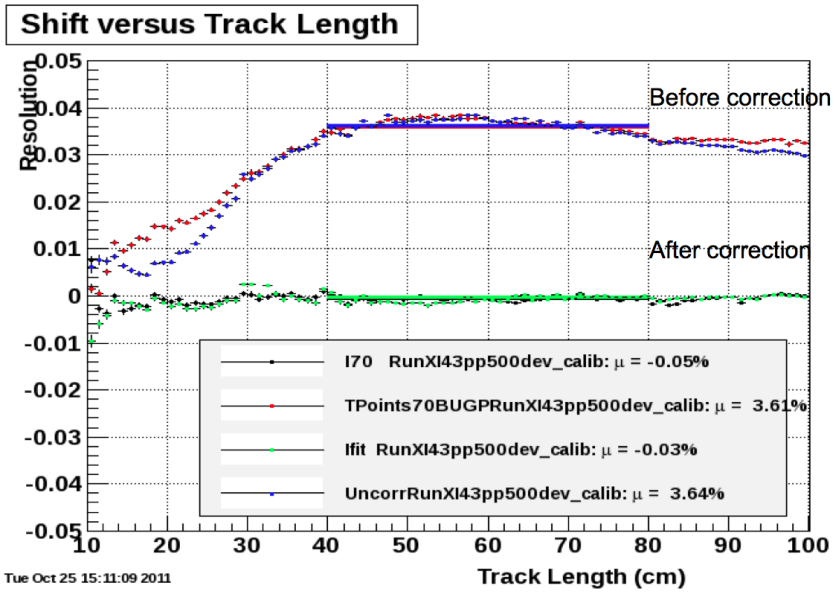

Figure 2.11 Variation vs track length before correction and after correction.

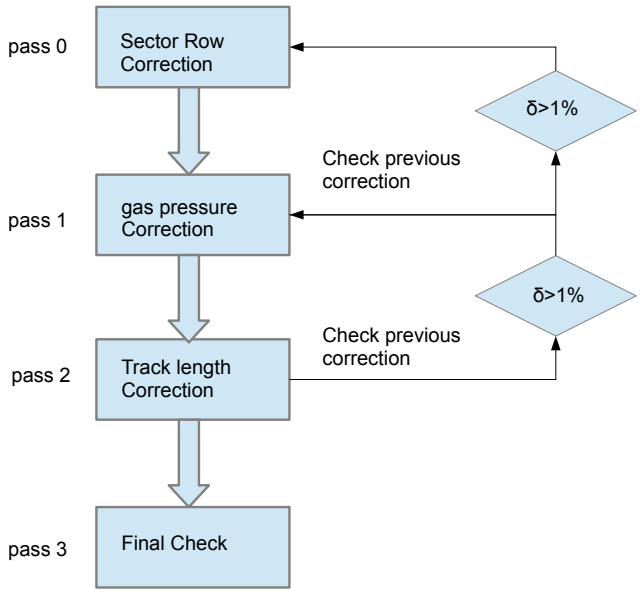

Figure 2.12 The procedure of *dE/dx* calibration.

The external plates are $20.6\ cm \times 7.6\ cm \times 1.1\ mm$ with electrodes on the outer surface. High voltage is applied on these electrodes to generate a uniform strong electric field in each sub-gap. All the internal plates are electrically floating. When charged particles go through the chamber, they generates avalanches in the gas gaps. The resistive plates are transparent to charge induction from avalanches in the gaps. Thus the signal collected on the copper pickup pads is the sum of possible avalanches from all gas gaps. The typical size of a MRPC module is $94\ mm \times 212\ mm \times 12\ mm$ and the active area is $61\ mm \times 200\ mm$, and has 6 readout pads which has an area of $63\ mm \times 31.4\ mm$ with $3\ mm$ gaps between pads.

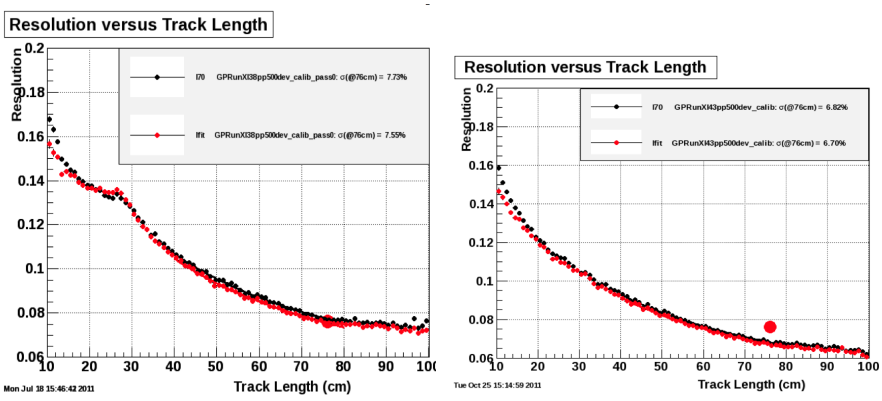

Figure 2.13 *dE/dx* resolution as a function of track length without any correction (left) and with all corrections (right) for p+p 500GeV in Run11.

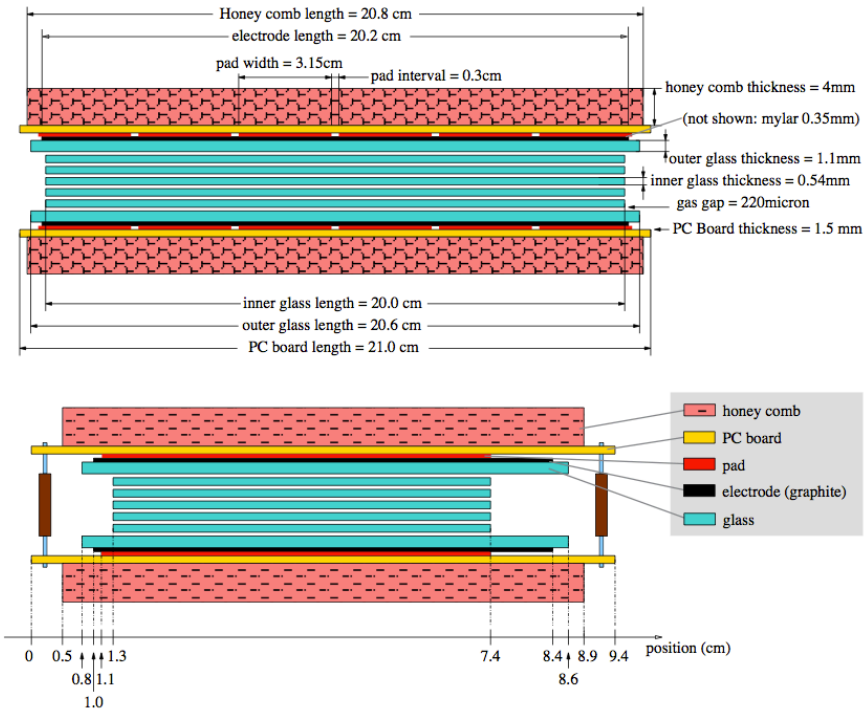

Figure 2.14 Two side views of the structure of an MRPC module. The upper (lower) is for long (short) side view. The two plots are not at the same scale.

One TOF tray consists of 32 MRPC modules which are installed alone the beam direction. Every modules contains 6 read out units (cell/channel). Figure 2.15 shows the structure of a STAR-TOF tray. The bTOF contains 120 trays in total and has a coverage of 2π in azimuthal direction and $|\eta| < 0.9$ in beam direction. The first prototypes of TOF were installed in year 2003. 72% of the bTOF were installed in 2009 and fully installed with 2π azimuthal coverage in 2010. The typical time resolution of TOF system is smaller than 100 ps. Figure 2.16 shows the inverse velocity ($1/\beta$) distribution as a function of momentum. With the installation of TOF, the momentum range of separating π and k is improved from 0.7 GeV/c to 1.8 GeV/c, and proton identification range is improved from 1.1 GeV/c to 3 GeV/c.

2.2.4 STAR trigger system

At STAR, the collision rate for Au+Au events is about 50 kHz, and for high luminosity p+p collisions, this rate can reach up to 4MHz which is close to the magnitude of the RHIC bunch crossing rate (10MHz). However, the STAR DAQ system can only operate at a rate below 1800Hz which is more than 3 magnitudes lower than the collision rate. Thus a trigger system is needed to reduced the event rate. Furthermore, only a small fraction of the collisions are physically interested. The beam may hit residual gas

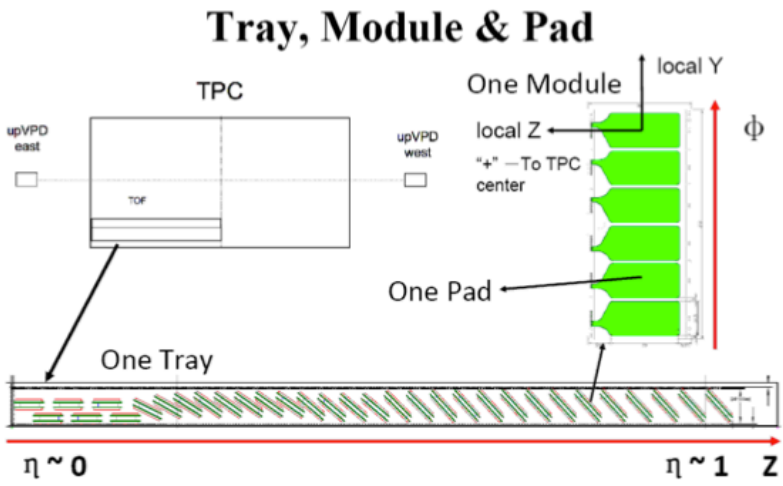

Figure 2.15 The structure of a STAR-TOF tray.

atoms in the beam pipe and also beam pipe itself, which makes a large fraction of the collisions are background. These background events should be also suppressed by the trigger system. The trigger system also includes triggers designed for special physics purpose, such like, selecting events containing high p_T particles for heavy flavor and jet physics.

The STAR trigger system consist of three levels. Figure 2.17 shows data flow through the trigger system. Level 0 examines every branch crossing to determine whether there is a interested interaction happened. It is constrained to issue a trigger decision within 1.5 μs after the interaction. The signals from fast detectors are digitized and sent into Data Storage and Manipulation (DSM) boards. The DSM boards analyze these signals and form a decision tree which is fead into Trigger Control Unit (TCU) board where the Level 0 trigger decision is issued. Level 1 and 2 triggers apply more complex criteria on events accepted by Level 0 trigger. Level 1 has a time budget ~ 100 μs and Level 2 has about 5 ms. When an interaction is accepted at Level 2, the trigger system notifies the DAQ system and detectors. A review on the STAR trigger system can be find at [17].

2.2.5 High Level Trigger/L4 system

The High Level Trigger (HLT) system replaced the old Level 3 trigger system which was abandoned since it could not catch up with STAR's DAQ system upgrade. Similar with the old Level 3 trigger system, HLT is trigger system base on online tracking and analysis. In Sec 2.2.4, we introduced the multi-level trigger system based on fast

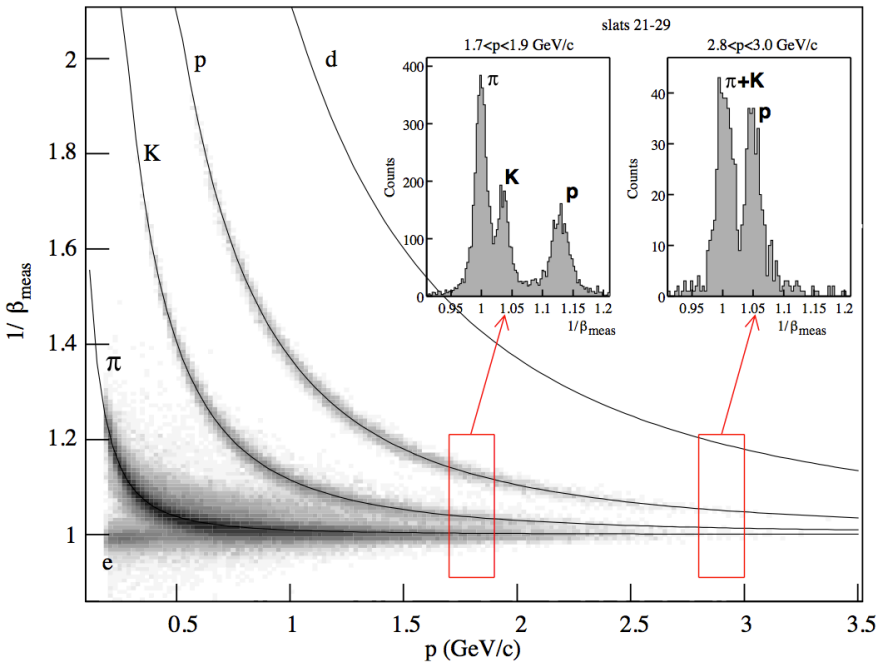

Figure 2.16 $1/\beta$ vs momentum distributions. The solid lines show the expected value for each particles

hardwares with simple trigger algorithms. It rejects most of the background events and reduce the event rate down to a level under STAR DAQ system limitation. At this points, for events selected by this trigger system, signals from all detectors are digitized and passed to STAR DAQ system for further processing. The HLT system is implemented after that. Similar as the offline event reconstruction process, it collects informations of subsystems from DAQ system, reconstructs events in real time, then it issues a trigger decision base on real time PID and analyze. It will select events with great physics interest, such as heavy fragmentation, di-electrons, exotics and UPC collisions.

The prototype of STAR HLT was tested in 2009 and implied in 2010. It worked as a tag system which tags events that pass through certain analyze algorithm. During the RHIC Beam Energy Scan (BES) program, it was used as an event monitor. Figure 2.18 shows the architecture of the HLT system used during year 2009~2012. It consists of two sub level, the Sector Level 3 (SL3) and the Global Level three (GL3). SL3 shares half of the computing power on 24 TPX computers, where cluster finding and track reconstruction are performed, sector by sector. After that, tracks from all sectors as well as informations from other subsystem are sent to GL3 machines, where they are assembled and analyzed to make a real time event selection. Currently, BEMC and TOF are included in HLT.

To keep up with the speed of DAQ system, a few techniques and approach have

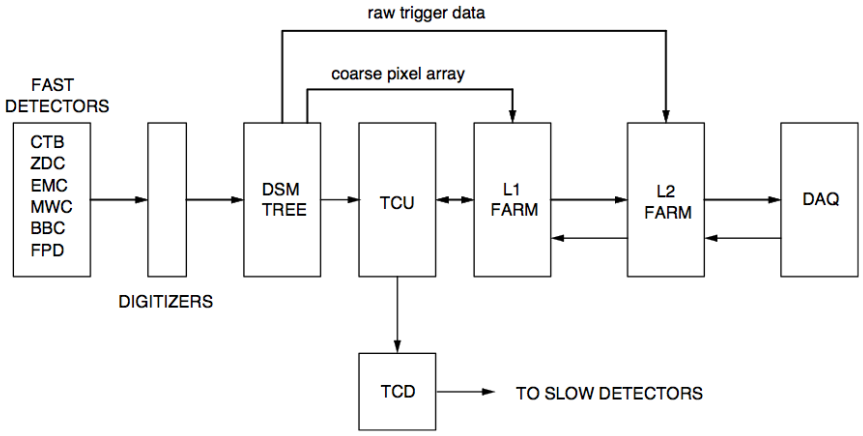

Figure 2.17 Data flow through the trigger [17].

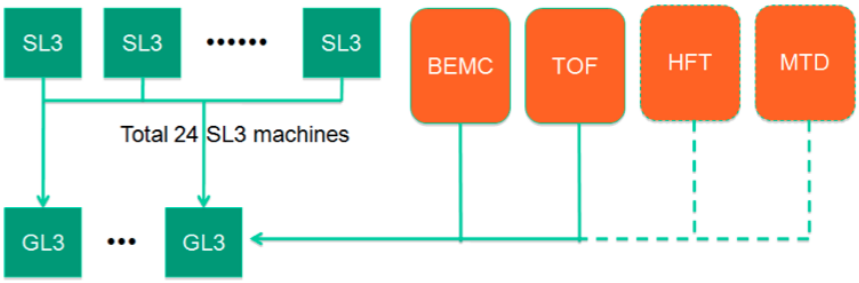

Figure 2.18 Architecture of the STAR high-level trigger. Solid lines connect the currently used subsystems and dashed lines connect subsystems that will be included in the future.

been implemented in HLT to increasing the processing speed. We introduced the TPC hit map to combined the calculation and correction for TPC hits in one step. It contains a grid map divided by all 24 sectors, all 45 pad rows, one for every 30 pads and one for every 40 time bucket. Points on the grid contains all the corrections the same as offline reconstruction. Points between grids are calculated as weighted average of adjacent grids. With the TPC hit map, the CPU time of hits reconstruction is reduced from ~ 1 s per event to ~20 ms per event. Tracking reconstruction in HLT is done sector by sector in parallel, so 24 times of speed-up is naturally achieved. The STAR HLT tracker is based on conformal mapping [54] and a follow-your-nose approach on finding next-hit-on-track. These approaches greatly reduces the track time with little loss on efficiency and track resolution (at p_T>1 GeV/c efficiency w.r.t offline is 90% and momentum difference w.r.t offline is less than 2%). The TOF and BEMC calibration tables for HLT was made following the same procedure as offline. The EMC pedestal and gain table are the same as the one used by STAR's lower level triggers. The TPC *dE/dx* calibration is made

by adjusting the *dE/dx* gain obtained from the previous run, for inner and outer sector separately. The calibration for TPC hit positions are folded into the TPC hit map based on offline calibration tables.

During year from 2010 to 2012, the STAR HLT has delivered several important physics results by selecting events containing heavy fragments, di-electrons and high p_T tracks. It played a very important role in the finding ${}^4\bar{H}e$ in $\sqrt{s_{NN}}$ = 200 GeV Au +Au collisions by triggering on events containing charge-2 particles. This discovery has been published in *Nature* [55]. A brief review about the HLT and its future development can be find at [56].

2.3 Future upgrade

In 2014, two new detectors was added into the STAR detector system. Installed in the most outside of STAR is the Muon Telescope Detector (MTD), which is a μ detector. MTD is based on long-MRPC technology, covers 45% acceptance ($|\eta| < 0.5$) in η direction and 2π in azimuthal direction. It uses the BEMC and the magnet steel as the absorber of electrons and hadrons. The first prototype was installed in STAR in year 2007, and showed good performance in the following runs. In 2014, MTD has been fully installed and significant data set was taken with it. Another detector installed in 2014 is Heavy Flavor Tracker (HFT). The HFT is an inner vertex detector which was installed between the beam pipe and TPC. It consists of two layers of pixels located at mean radius of 1.5 cm and 5 cm from the center of beam pipe and the Silicon Strip Detectors (SSD) to fill the gap between the innermost pixel detector and the TPC.

Chapter 3 Analysis

3.1 Data set and event selection

The data set used in this analysis was minimum bias triggered events taken in year 2010 and year 2011 Au+Au 200 GeV collisions and central triggered data taken in year 2010 Au+Au 200 GeV collisions. For demonstration, the Au+Au data in year 2010 was analyzed by Bingchu Huang and Jie Zhao [57, 58] (My contribution in this data set is on consistency check and efficiency calculation). Only year 2011 data are used to demonstrate the analysis method for Au+Au 200 GeV, and the analysis method for year 2010 and year 2011 are similar. The final results reported in this thesis are from the combined year 2010 and year 2011 data for Au+Au 200 GeV collisions. For the p +p analysis, the data set was taken in year 2012 p+p 200 GeV minimum bias collision. The minimum bias trigger was defined as a coincidence in the east and west VPDs, and an online vertex cut was applied to select the collision happening in the center of the detector. For the central trigger, a small signal in the ZDC detectors was required as well as a large multiplicity from the barrel TOF. This trigger corresponds to 0-10% of the total hadronic cross section.

Events used in this analysis were selected by the following event selection criteria. To insure the TPC performance, events were required to have a valid reconstructed collision vertex (primary vertex, defined by primary tracks) within 30cm (for Au+Au 200 GeV collisions, Figure 3.1 (c)) and 50cm (for p+p 200 GeV collisions) of the TPC center alone the beam pipe (z direction). Figure 3.1 (b) shows correlation between TPC vertexZ and VPD vertexZ. The clean diagonal correlation band indicate the correct vertices which fire the VPDMB trigger. Random distributions could also be seen in a wide region which typically indicate the vertex found by TPC is a pile-up vertex (the wrong vertex from different bunch crossing collisions). The cross like distribution in the random correlation regions is due to the online vertexZ cut in the trigger definition. To suppress the pile up events and to ensure that the selected event is firing the trigger, the difference between event vertex z-coordinate (V_z) and the V_z calculated from the VPD timing was required to be within 3cm (for Au+Au 200 GeV collisions) and 6cm (for p+p 200GeV collisions). In order to remove the events from the Au beam hitting the Beam pipe, 2cm of the vertex radius cut in transverse plane was also applied in the data

Au+Au 200 GeV	p+p 200 GeV
First primary vertex	First primary vertex
$\|Vr\| < 2cm$	
$\|Vz\| < 30cm$	$\|Vz\| < 50cm$
$\|Vz - VzVpd\| < 3cm$	$\|Vz - VzVpd\| < 6cm$

Table 3.1 vertex selection criteria.

Year	Run Type	# of events
2010	Au+Au 200 GeV MinBias	240M
	Au+Au 200 GeV Central	220M
2011	Au+Au 200 GeV MinBias	490M
2012	p+p 200 GeV MinBias	375M

Table 3.2 Number of events after event selection.

selection. The vertex criteria is also shown in table 3.1. The events number after event selection is shown in table 3.2.

3.2 Centrality definition

The centrality in Au+Au 200 GeV collisions was defined using the uncorrected charged particle multiplicity $dN/d\eta$ within $|\eta| < 0.5$ (also called reference multiplicity). A Monte Carlo Glauber calculation was used to compared with the $dN/d\eta$ distribution from data to define centrality bins. The dependence on collision vertex Z-position and the luminosity has been also taken in account to address the efficiency and acceptance change on the measured $dN/d\eta$. Figure 3.2 shows the uncorrected $dN/d\eta$ distribution measured within $|Vz| < 5cm$ and extrapolated to zero ZDC coincidence rate for the VPDMB triggered events for Au+Au 200 GeV collision in year 2010 as well as the MC Glauber simulation [59]. The discrepancy at the low multiplicity is because the VPD trigger efficiency starts getting lower while fewer particles are produced in peripheral collisions. The difference in low multiplicity region has been taken as a weight with the ration shown in Fig. 3.2 (bottom panel) to account for the VPD inefficiency. Finally, the centrality bins are determined by the cut on the measured multiplicity according to the MC Glauber distribution. Table 3.3 lists $\langle N_{part} \rangle$ and $\langle N_{bin} \rangle$ from the Glauber model simulation at $\sqrt{S_{NN}} = 200$ GeV Au+Au collisions.

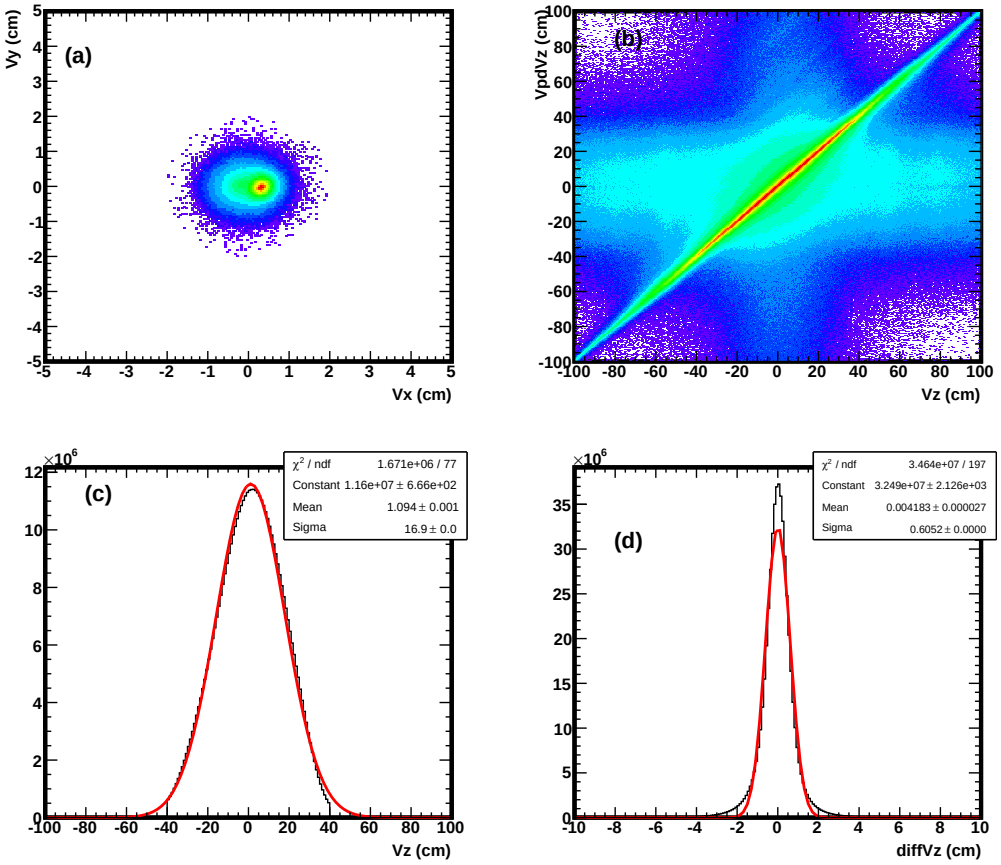

Figure 3.1 (a) TPC vertex distributions in transverse plane, (b) TPC vertex in Z direction (V_z) and the VPD V_z correlation, (c) V_z distribution of TPC primary vertex, (d) difference between TPC V_Z and the VPD V_Z in Au+Au 200 GeV minimum bias collisions.

3.3 Track selection and electron identification

3.3.1 Track selection

Electron (including positron if not specified) candidates are selected from good tracks satisfied the flowing selection:

1. number of fit points (*nHitsFit*) in the TPC greater than 19 (maximum 45) to ensure good tracking quality and momentum resolution;

2. the ratio of number of fit points over number of possible fit points in TPC greater than 0.52 to avoid split tracks in the TPC;

3. distance of closet approach (*dca*) to the primary vertex less then 1 cm to make sure selected tracks are from the primary collision;

4. number of *dE/dx* points used for calculation average *dE/dx* greater than 15 to ensure good *dE/dx* resolution.

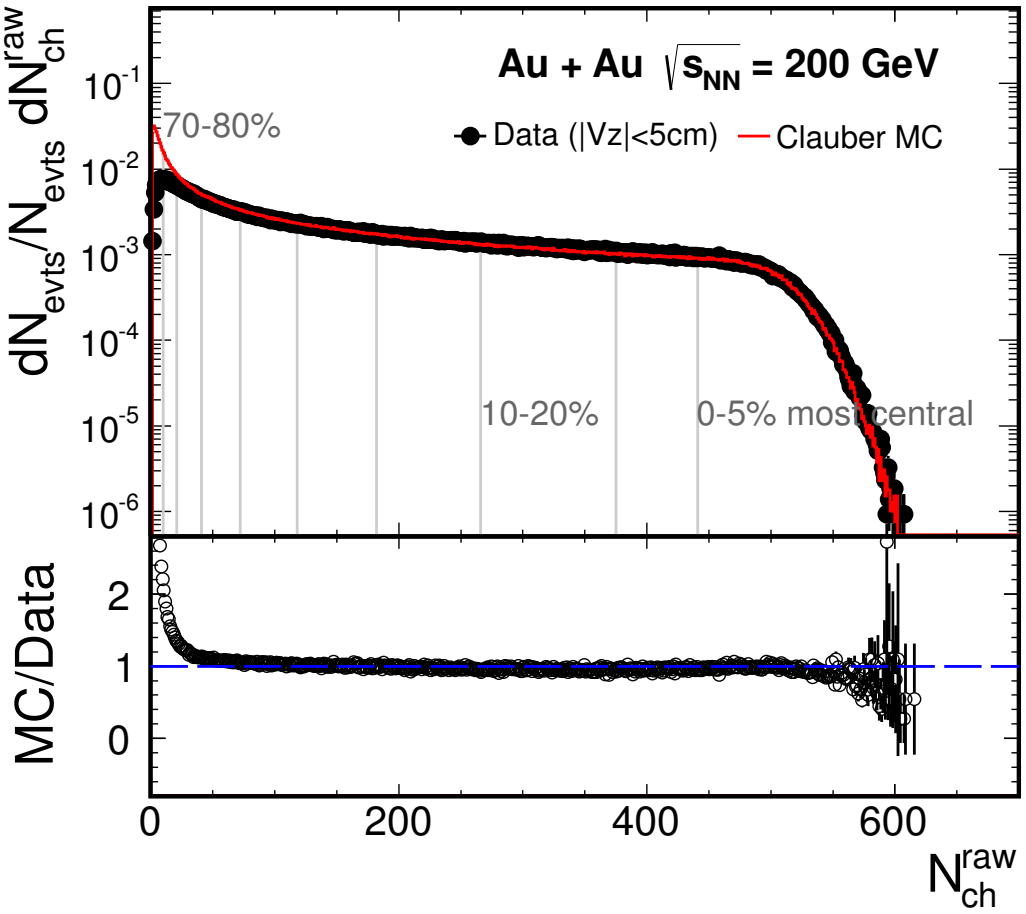

Figure 3.2 Upper Panel: Uncorrected charge particle multiplicity distribution measured within $|\eta| < 0.5$ and $|Vz| < 5cm$. The red curve represents the multiplicity distribution from MC Glauber calculation. Bottom Panel: the ratio between MC and data.

5. with a valid matching to a TOF hit and projected position on TOF module with the sensitive readout volume.

Table 3.4 left part lists the detailed track quality cut.

3.3.2 Electron identification

In additional of track detection, momentum determination, TPC also provide particle identification for charged particles by measuring their ionization energy loss (*dE/dx*) in the TPC gas. Usually, a normalized *dE/dx* (also called $n\sigma$) is used, which is defined:

$$n\sigma_e = \frac{1}{R_{dE/dx}} ln \frac{\langle dE/dx \rangle^{Mea}}{\langle dE/dx \rangle_e^{Bichsel}} \tag{3.1}$$

in the Eq. 3.1: $R_{dE/dx}$ is the *dE/dx* resolution, *Mea* and *Bichsel* are measured value and theoretical value. $n\sigma_e$ follows a standard gaussian distribution.

With TPC only, however, it is difficult to separate electron from hadrons because

Centrality	$\langle N_{part} \rangle$	$\langle N_{bin} \rangle$
0-10%	325.5 ± 3.7	941.2 ± 26.3
10-40%	174.1 ± 10.0	391.4 ± 30.3
40-80%	41.8 ± 7.9	56.6 ± 13.7
0-80%	126.7 ± 7.7	291.9 ± 20.5

Table 3.3 Summary of centrality bins, average number of participants $\langle N_{part} \rangle$ and number of binary collisions$\langle N_{bin} \rangle$ from Monte Carlo Glauber simulation at $\sqrt{S_{NN}} = 200GeV$ Au+Au collision.

the electron band crosses with hadron bands in higher momentum. With the flight timing information measured by TOF and the track path-length measured by TPC, we can calculate the velocity (β). Due to the very small electron mass, electron can be separated from the slow hadron by the velocity cut. Combining the velocity (β) information from TOF and energy loss(*dE/dx*) from TPC, electron can be identified up to momentum ~3GeV/c. Figure 3.3 left panel shows the inverse velocity distribution as a function of momentum, while the $n\sigma_e$ vs momentum distribution after TOF velocity cut is shown in right panel. The detailed electron identification cuts are listed in Table 3.4.

Track quality cuts		PID cuts	
dca	<1cm	p_T	> 0.2GeV/c
nHitsFit	>= 20	$n\sigma_e, p < 1.0GeV/c$	$1.5 \times (p-1) - 0.8 \sim 2.0$
nHitsFit/nHitsPoss	>=0.52	$n\sigma_e, p > 1.0GeV/c$	$-0.8 \sim 2.0$
ndEdxFit	>=16	TOF $1/\beta$	$\|1 - 1/\beta\| < 0.025$ (Au+Au)
η	+/- 1		$\|1 - 1/\beta\| < 0.03$ (p+p)
		TOF yLocal	$\|yLocal\| < 1.8cm$

Table 3.4 Electron selection criteria

3.3.3 Hadron contamination and electron purity

From Fig 3.3 right panel, even after the TOF cut, the slow hadron bands can still be seen in $n\sigma_e$ vs momentum distribution plot. We selected pure hadron (π, k and p) sample by a very tight m^2 cut provided by TOF (shown in Fig 3.4 left panel). The pure electron sample was from photonic conversion and π^0 Dalitz decay (Fig 3.4 (right)). This sample was also used in the efficiency study. Gaussian functions were used to parameterize the $n\sigma_e$ distribution from the pure sample for different particle species. Then, the hadron contamination and electron purity were studied by multi-gaussian fit

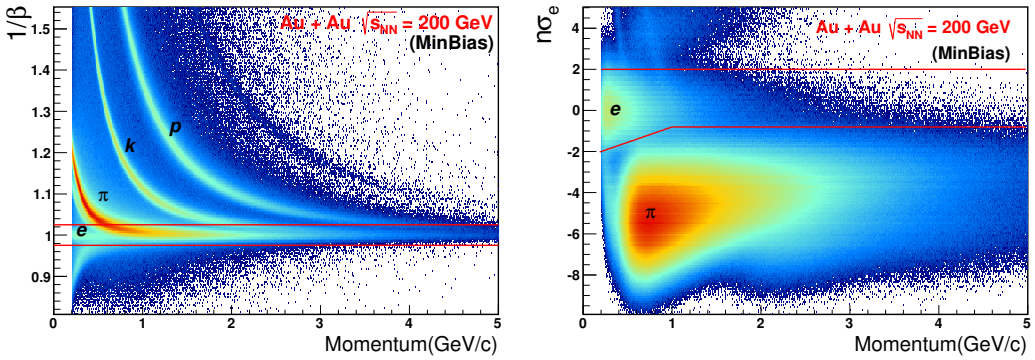

Figure 3.3 Left panel: inverse velocity $1/\beta$ vs momentum distribution in 200GeV Au+Au collisions. Right panels: $n\sigma_e$ distribution as a function of momentum after TOF velocity cut $|1/\beta - 1| < 0.025$ in 200GeV Au+Au collisions. The red lines in both panels show the PID cuts.

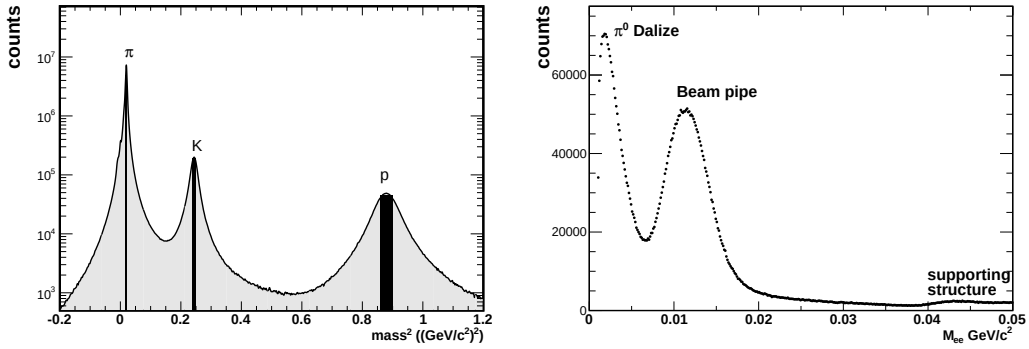

Figure 3.4 Left panel: Hadron sample selected by TOF. Right panel: pure electron sample from π^0 Daliza decay and photonic conversion.

to the $n\sigma_e$ distribution in differential momentum bins to obtain the yields for different particles. The mean and σ were fixed in the fit respecting to the value obtained from the pure sample. Figure 3.5 picks up the fit result in momentum bin [0.6, 0.64) GeV/c as an example. The fit also included the merged π component which is from the merging of two closed π tracks, and thus has a doubled *dE/dx* value compared to a normal π track. In some momentum regions, the electron band crosses with the hadron bands, where the multi-gaussian fit may not be reliable. In this analysis, exponential functions were used to extrapolate the particle yields into the cross region (Figure 3.7 (left), and the uncertainties from the exponential fit were taken into account as systematic uncertainty. Figure 3.7 right panel shows the electron purity for Au+Au 200GeV minimum bias data taken in year 2011. Table 3.5 lists electron purity for the data set used in this analysis.

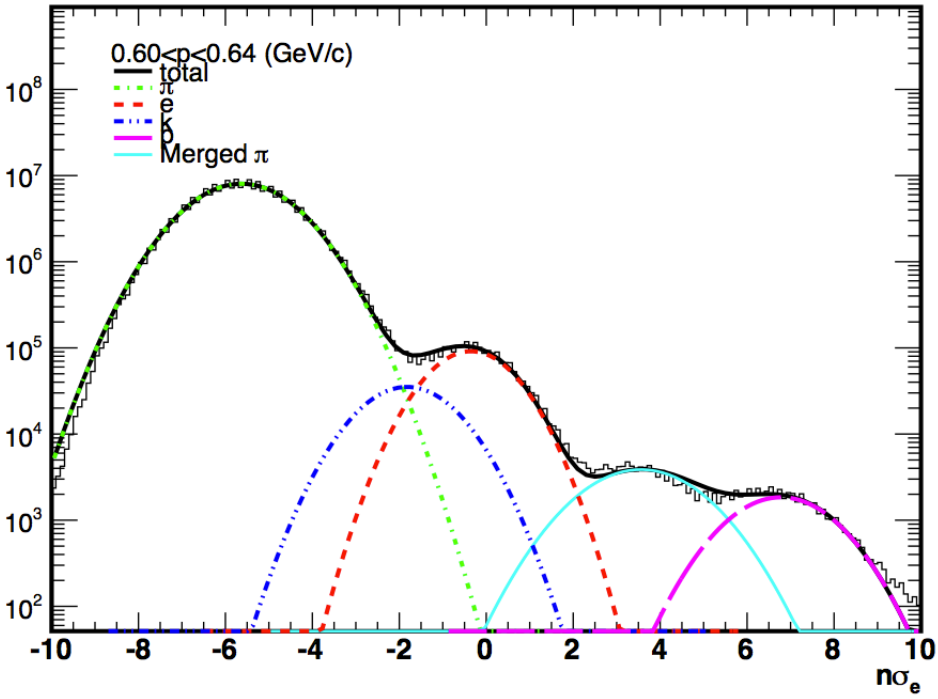

Figure 3.5 A multi-gaussian fit in momentum bin [0.6, 0.64) (GeV/c) in Au+Au 200GeV minimum bias collisions.

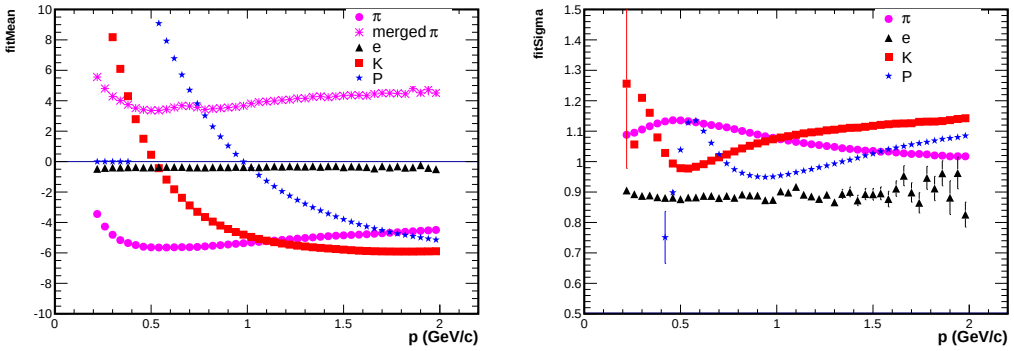

Figure 3.6 Mean (left) and sigma (right) of the gaussian distribution as a function of momentum from pure samples for different particle species in Au+Au 200GeV minimum bias collisions.

Au+Au 200GeV	MinBias	$\sim 0.946 \pm 0.024$
	Cenrtral	$\sim 0.921 \pm 0.025$
p+p 200GeV	MinBias	$\sim 0.980 \pm 0.040$

Table 3.5 Electron average purity for different data samples.

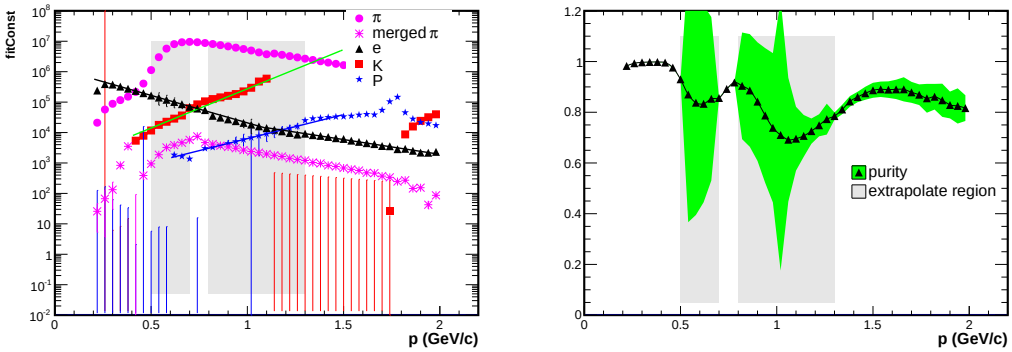

Figure 3.7 (left) Yields for different particle species from multi-gaussian fit as a function of momentum. The grey area show the cross region. And the solid lines depict the exponential fits to extrapolate the yields in the cross region. (right) Electron purity as a function of momentum, the green band represents he uncertainty from the extrapolation and the multi-gaussian fits.

3.4 Pair reconstruction and background

The dielectron pairs (foreground, also marked as *unlike-sign pairs*) were reconstructed by randomly combining electron and position from the high purity electron (position) sample from the same event. The invariant mass of dielectron pairs M_{ee} were calculated as :

$$M_{ee} = \sqrt{(E_+ + E_-)^2 - (\vec{p_+} + \vec{p_-})^2} \tag{3.2}$$

where $E_\pm = \sqrt{(\vec{p_\pm})^2 + m_e^2}$, $m_e = 0.511 MeV/c$, and $\vec{p_\pm}$ is the momentum of electron (positron) which was measured by TPC. The candidate tracks were required to satisfy cut: $p_T > 0.2 GeV/c$ and $|\eta| < 1$ to fit into the acceptance of STAR detector, while the dielectron pairs were constructed in mid-rapidity ($|y_{ee}| < 1$). Unlike-sign pairs include the dielectron signal and background, where the signal is defined by dielectron pairs from hadron decay, and QGP/media contribution which is what we are interested . On the other hand, the background includes the following source:

1. Combinatorial background: background comes from randomly pairing, which is uncorrelated.

2. Correlated background, which is the case that two partner tracks come from different parents but from the same source. E.G, $\pi^0 \to \gamma + e^+e^-$, then γ converts into another e^+e^- pair, when pair is combined randomly, it is possible to pick one track from π^0 decay and another from the converted photon. There is also contribution from Jet, e.g electrons and positrons from same Jet or back to back Jet. In this case, the final state particles are correlated, which is mainly contributed in

high momentum and high mass region. In additional, the hadron contamination also has small contribution, e.g π, p from Λ decay are misidentified by electrons. This contribution was considered as systematic uncertainty, and will be discussed in following section.

3. Photon conversion. The invariant mass of dielectron pairs from real photon conversion should be close to 0. However, due to the primary track reconstruction algorithm, the momentum of these electrons from conversion which happened away from the primary vertex are biased, which lead to a finite pair invariant mass. This kind of background mainly contributes in very low mass region ($M_{ee} < 0.2GeV/c^2$). It will be discussed in detail in follow section.

In this analysis, we adopted two methods to reproduce the background.

3.4.1 Like-sign method

The Like-sign method is used to calculate contributions of uncorrelated and correlated background at the same time and serves as a standard of the background to justify the background distribution. In this analysis, we constructed like-sign background by randomly combining same charge pairs N_{++} , N_{--} from the same event. We used the geometric mean of the like-sign pairs $2\sqrt{N_{++} \times N_{--}}$, because it is demonstrated in this paper [2] that when the e^+ and e^- are produced in statistically independent pairs, the geometric mean fully describes the background in the unlike-sign pair foreground distribution.

The TPC has de-active zones, (e.g the gap between TPC sectors), and in magnet field, different charged particles are bended into opposite direction. Therefore, the acceptance of different charged particle is different. Figure 3.8 shows the transverse momentum (p_T) vs azimuthal angle (ϕ) distribution of negative tracks and positive tracks in magnet field. The white bands show the de-active regions of TPC. In Figure 3.8, it can be clearly seen that the acceptance effect is different for negative and positive charged tracks. Therefore, the acceptance of unlike-sign pairs and like-sign pairs are different (Fig 3.9).

To address this difference, mixed event method was used in this analysis. Because it does not include correlated pairs, mixed event method can be used to study the detector acceptance effect. The like-sign background was calculated by Eq. 3.3, and the acceptance correction factor also defined there. In principle, the acceptance difference should be studied in several dimensions, such like p_T, electron decay angles, θ and ϕ

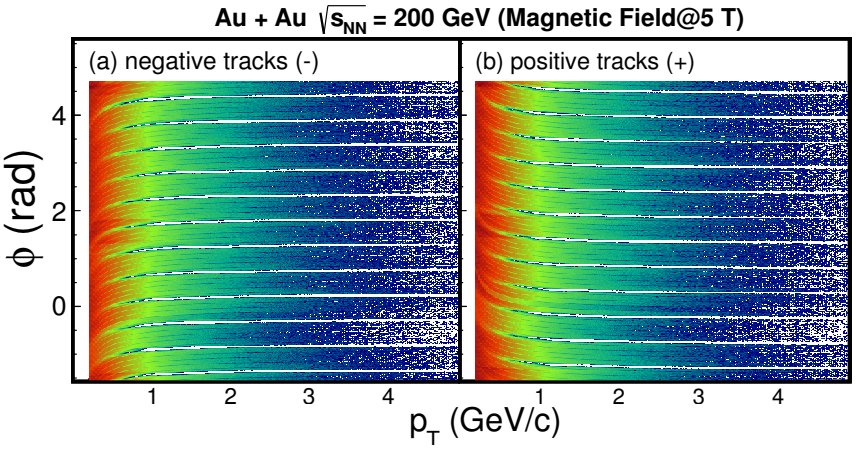

Figure 3.8 p_T vs ϕ distribution for negative tracks (a) and positive tracks (b) in magnet field.

etc. But due to the limited statistics, we now only calculated the acceptance factor in 2D (mass vs p_T). And the difference between 2D and 1D (mass) was used to estimate the systematic uncertainty due to the statistical fluctuation. Figure 3.10 shows acceptance correction factor as function of M_{ee} in 200 GeV Au+Au and p+p minimum bias collisions.

$$N_{likesign}(M_{ee}, p_T) = 2\sqrt{N_{++}(M_{ee}, p_T) \times N_{--}(M_{ee}, p_T)} \cdot F_{acc}(M_{ee}, p_T)$$
$$F_{acc}(M_{ee}, p_T) = \frac{N^{Mix}_{+-}(M_{ee}, p_T)}{2\sqrt{N^{Mix}_{++}(M_{ee}, p_T) \times N^{Mix}_{--}(M_{ee}, p_T)}} \tag{3.3}$$

3.4.2 Mixed event method

Like-sign method as mentioned in section 3.4.1 can fully reproduce combinatorial background and correlated background. However, the like-sign background is lack of statistics. In this analysis, the like-sign background was used in low mass region ($M_{ee} < 0.75$ GeV/c^2) where we have better statistics and also the sizable contribution from correlated pairs. For higher mass region, event mixing technique was used to achieve better statistical accuracy.

Mixed event background is reproduced by mixing electron candidate tracks from different events. Since the two tracks are uncorrelated, mixed event method is only able to reconstruct combinatorial background. To ensure events mixed together have similar structure, we classified event sample according magnet, centrality, Vz and event plane, and split it into $Magnet \times Centrality \times EventPlane \times Vz = 2 \times 9 \times 12 \times 10$ event pools. Each event pool holds 50 (100 for p+p data) events at maximum, when the

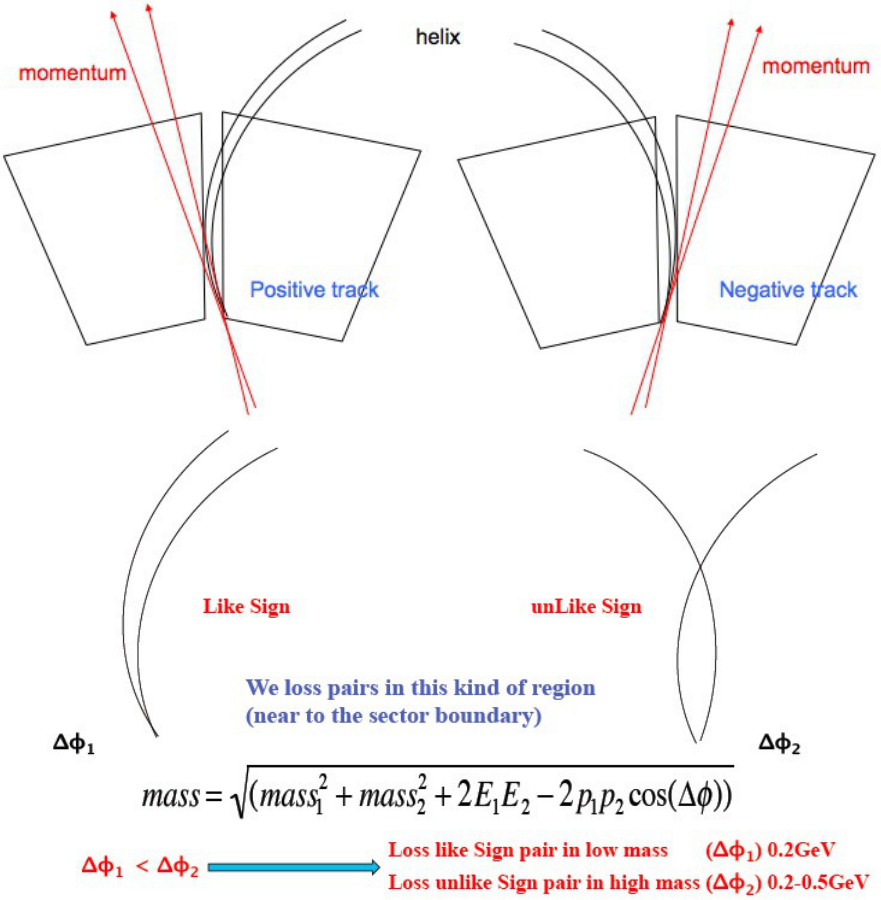

Figure 3.9 A cartoon shows the acceptance difference between unlike-sign pairs and like-sign pairs.

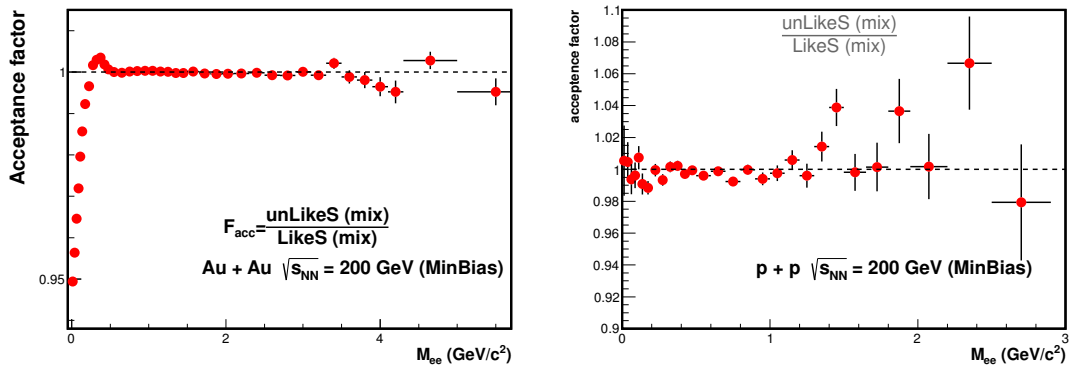

Figure 3.10 Acceptance correction factor in Au+Au (left) and p+p (right) collisions at 200 GeV.

number of events in the event pool reach limitation, one event is randomly dropped to make space for the new coming events. Dr. Jie Zhao did very detailed study about the number of event pools and event buffer effect on mixed event background in [57]. Here we chose the number of event pools and size of event buffer according to his study.

The mixed event background should be normalized to the same amplitude of like-sign background, since the like-sign background can fully reproduce the real background. The following equation was used to calculate the normalization factor:

$$\begin{aligned} A_{\pm} &= \frac{\int_{N.R} N_{\pm\pm}(M,p_T)dMdp_T}{\int_{N.R} N^{Mix}_{\pm\pm}(M,p_T)dMdp_T} \\ B_{\pm\pm} &= \int_0^{\infty} A_{\pm} N^{Mix}_{\pm\pm}(M,p_T)dMdp_T \\ N^{Norm}_{Mix}(M,p_T) &= \frac{2\sqrt{B_{++}B_{--}}}{\int_0^{\infty} N^{Mix}_{+-}(M,p_T)dMdp_T} N^{Mix}_{+-}(M,p_T) \end{aligned} \tag{3.4}$$

N.R represents the normalization region. The statistical uncertainty of the normalization factor is included into the total statistical uncertainty.

However, since the mixed event method can not reconstruct correlated background, the shape of mixed event background is expected to be different with the like-sign background. The normalization region was chosen as the flat region in $(N_{likesign} - N^{Mix}_{likesign})/\sigma(N_{likesign} - N^{Mix}_{likesign})$ which is shown in Fig 3.11. To take into account the difference between the like-sign and mixed event background, we used function 3.5 to fit the ratio of like-sign over mixed event background (Fig 3.12), and subtracted it in additional as *residue* of the correlated component from the foreground. The 68% confidence level of the fit was taken into accounted as systematic uncertainty.

$$f(M_{ee}) = 1 + exp((M_{ee} - a)/b) \qquad a, b \sim free\, parameters \tag{3.5}$$

3.4.3 Photon conversion

Photon conversion is that photon hit material of detectors and convert to e^+e^- pairs. When reconstructed unlike-sign foreground, it has contribution to the very low mass region ($M_{ee} < 0.2GeV/c^2$). Therefore, it must be subtracted from the signal. The pair mass from photon conversion pairs should be 0. However, momentum of electron tracks from conversion vertex away from primary vertex is biased which lead to a finite pair invariant mass, because the procedure of reconstruction primary tracks also included the primary vertex as a fit point.

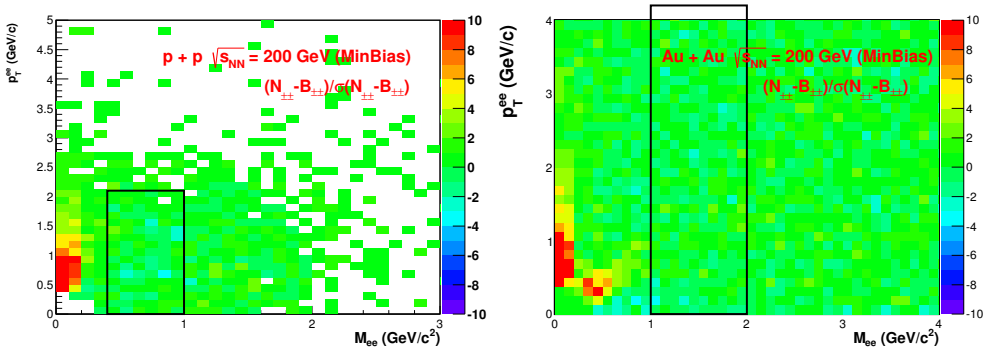

Figure 3.11 The difference between like-sign background and mixed event background divided by its standard deviation $(N_{likesign} - N^{Mix}_{likesign})/\sigma(N_{likesign} - N^{Mix}_{likesign})$ in p+p collision (left) and in Au+Au collision (right). the black box represent the chosen normalization region: $0.5 < M_{ee} < 1GeV/c^2$, $0 < p_T^{ee} < 2GeV/c$ for p+p data and $1 < M_{ee} < 2GeV/c^2$ for Au+Au data.

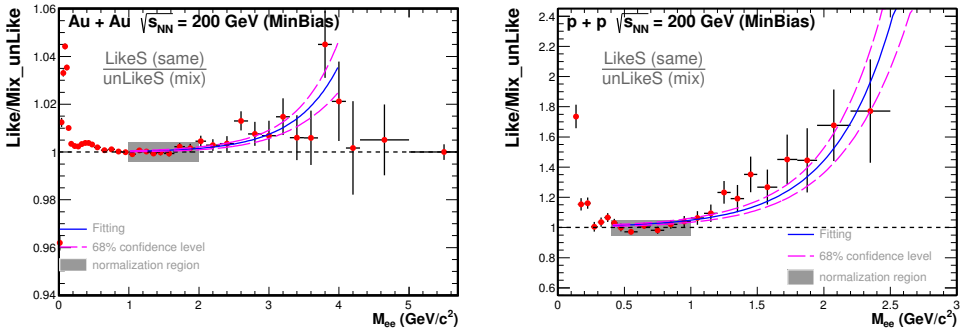

Figure 3.12 The distribution of like-sign over mixed event background ratio as a function of M_{ee}. The solid line depicts a fit to the raise about 1 GeV/c^2, while the dashed line shows 68% confidence level of the fit.

In this analysis, we used ϕ_V cut method which is similar to the method used by PHENIX [2]. Considering the zero opening angle of dielectron pairs from photon conversion, electron is bended inside the plate perpendicular to magnet direction. Therefore, ϕ_V is defined as Eq. 3.6, where $\vec{p}_+$, $\vec{p}_-$ are the momentum of e^+ and e^-, respectively, $\hat{z}$ is the direction of magnet.

$$\begin{aligned} \hat{\mu} &= \frac{\vec{p}_+ + \vec{p}_-}{|\vec{p}_+ + \vec{p}_-|}\,,\ \hat{\nu} = \vec{p}_+ \times \vec{p}_- \\ \hat{\omega} &= \hat{\mu} \times \hat{\nu}\,,\ \hat{\omega}_c = \hat{\mu} \times \hat{z} \\ \cos\phi_V &= \hat{\omega} \cdot \hat{\omega}_c \end{aligned} \tag{3.6}$$

ϕ_V should be zero (by consistently ordering positive and negative tracks within the pair we avoid $\phi_V = \pi$ as a solution for photon conversions), if the dielectron pair is originated from photon conversions. While, there is no preferred orientation for combinatorial pairs, and very weak dependence for dielectron pairs from hadron decays.

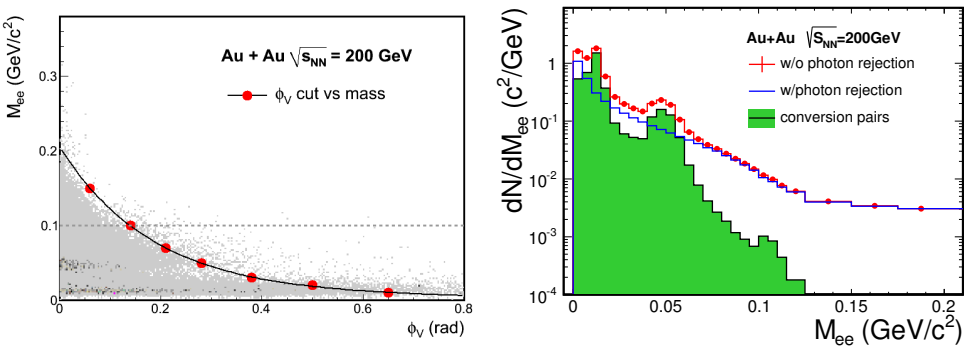

Figure 3.13 (left) ϕ_V *vs mass* distribution from Geant simulation, the solid line depicts the cut. (right) Dielectron mass spectra with photon rejection, without photon rejection and conversion pairs distribution from 200GeV Au+Au data. The conversion peaks from left to right are come from conversion happened at beam pipe (r~4cm), TPC supporting structure (r~20cm) and TPC inner field cage (r~46cm) , respectively.

A Geant simulation was done to study the distribution of ϕ_V vs mass (Fig 3.13(left) [60]). And the cut used in this analysis is shown as the red solid line. The conversion pairs were directly removed by this cut. This cut was only applied in very low mass ($M_{ee} < 0.2GeV/c^2$). Simulation shows ~95% conversion pairs are removed by this cut.

3.4.4 Centrality and p_T^{ee} dependence

In this analysis, for the Au+Au collision data, we also measured the dielectron mass spectra in different centrality bins and p_T^{ee} regions. The centrality and p_T^{ee} dependence of acceptance factor and correlated residue were also studied. Figure 3.14 shows the acceptance factor correction (acceptance difference between unlike-sign pairs and like-sign pairs) in different centrality and p_T bins. The acceptance factor shows a clear p_T dependence. It is because the bending effect in magnetic field is weaker for charged particles with higher p_T . The acceptance between positive and negative charged tracks is smaller at higher p_T. The correlated background residual distributions were also studied by using function 3.5 to fit the like-sign over mixed event background ratio in different centrality and p_T regions (Fig 3.15).

3.4.5 Dielectron signal

The follow tactics was used to subtract the background from the unlike-sign foregound:

- Considering the correlated component, we subtracted the like-sign background with an acceptance factor correction in mass region ($M_{ee} < M_{th}$, where $M_{th} =$

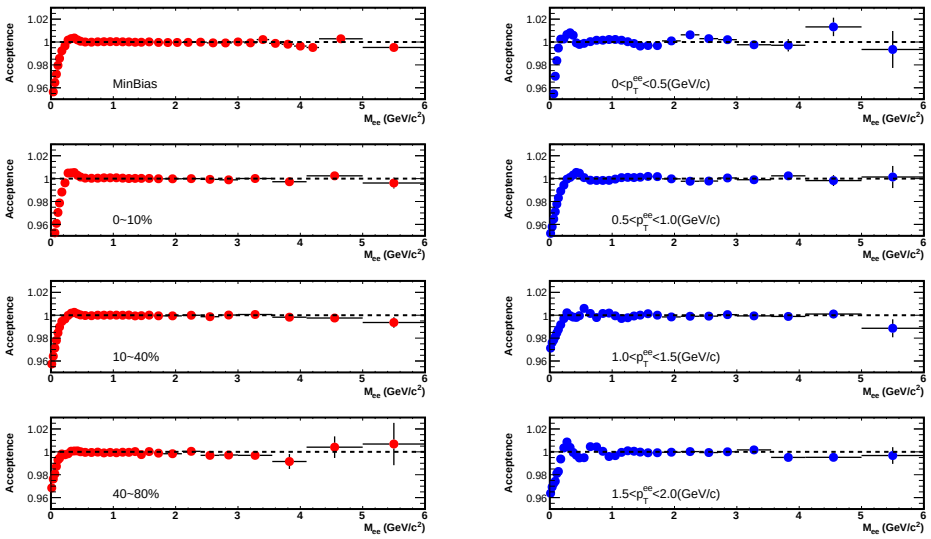

Figure 3.14 Acceptance factors in different centrality (left) and p_T (right) bins, for 200 GeV Au +Au collision data.

$1GeV/c^2$ for Au+Au collision, and $M_{th} = 0.4GeV/c^2$ for p+p collision), where the like-sign background has enough statistics.

- For the mass region above M_{th}, the normalized mixed event background was subtracted. And we subtracted the correlated component (Jet contribution) by fitting the ratio of like-sign over mixed event background (Eq. 3.5).

After the background subtraction, we got the raw dielectron spectra without efficiency correction. Figure 3.16 shows dielectron signal, foreground and background, as well as the signal over background ratio.

3.5 Efficiency and acceptance correction

The dielectron raw signal yields was corrected for efficiency within STAR acceptance of $|y_{ee}| < 1$, $|\eta_e| < 1$ and $p_T^e > 0.2GeV/c$. To calculate the efficiency, we first need single electron efficiency which can be separated into two parts: detector efficiency and PID efficiency. Then Monte Carlo method is used to evolved the single efficiency into pair efficiency. We will discuss it step by step, in the following sections.

3.5.1 Single electron efficiency

The single electron efficiency in this analysis included the TPC tracking efficiency (ε_{TPC}), TOF matching efficiency (ε_{TOF}) and electron identification efficiency (ε_{PID}) as Eq. 3.7.

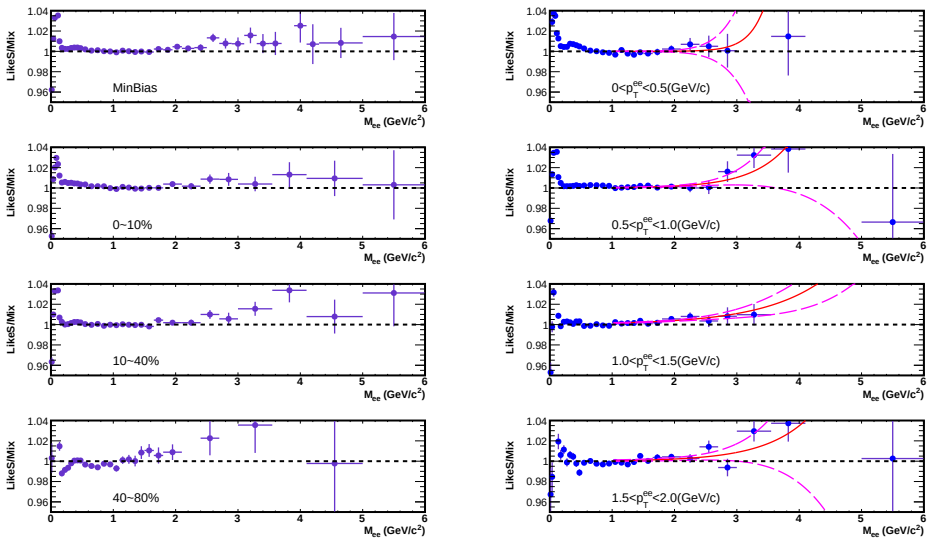

Figure 3.15 Like-sign over mixed event background ratio in different centrality (right) and p_T (left) bins, for 200 GeV Au+Au collision data.

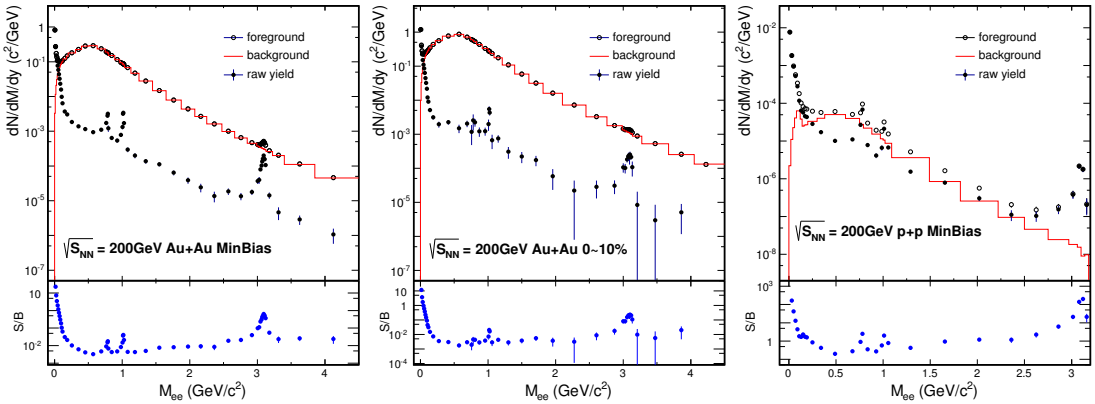

Figure 3.16 Unlike-sign foreground, background, raw dielectron spectra and signal over background ratio for Au+Au minimum bias (left), central (middle) collisions and p+p minimum bias collisions (right).

$$\varepsilon_{single} = \varepsilon_{TPC} \times \varepsilon_{TOF} \times \varepsilon_{PID} \tag{3.7}$$

TPC tracking efficiency The TPC tracking efficiency includes the track reconstruction efficiency and the TPC acceptance. Also the track quality cut (nHitFits, dca) efficiency are also combined into TPC tracking efficiency. The TPC tracking efficiency was obtained via the standard STAR embedding process. Monte Carlo (MC) electron tracks were generated within a certain phase space definition. The embedding tracks were sent into the GSTAR simulator and passed through STAR detector geometry corresponding to the data set and detector response simulator (TRS, TPC Response Simulator) to simulate the detector signal. Then, the MC tracks were mixed with the real data which we

called embedding sample here. The embedding sample were reconstructed by the same offline reconstruction chain used to produce real data. The tracking efficiency is defined by number of reconstructed MC tracks which satisfy the track quality cut divided by number of input MC tracks, also see Eq. 3.8.

$$\varepsilon_{TPC} = \frac{N_{rc}(nHitsFit \geqslant 20,\ dca < 1cm)}{N_{Mc}} \tag{3.8}$$

To qualify whether the embedding sample can reproduce the real data, we compared several track parameters (*nHitsFit, dca*) from embedding sample with those from the pure electron sample selected by photon conversion and π^0 Dalitz decay. The difference was included in the systematic uncertainty.

TOF efficiency The TOF efficiency (ε_{TOF}) was studied via comparing the number of track which matches TOF and the total number of TPC primary tracks from real data. A track match to TOF was defined as following:

- The track is projected to the radius of TOF, and there is a valid hit in the corresponding TOF cell (tofMatchFlag>0 in data structure).
- The distance between the projection position to the TOF cell center in local y coordinate (Localy) is smaller than 1.8 cm.

The definition of TOF matching efficiency is shown as Eq. 3.9.

$$\varepsilon_{TOF} = \frac{N_{matched}(tofMatchFlag > 0 \,\&\&\, |LocalY| < 1.8cm)}{N_{TPC}} \tag{3.9}$$

To achieve enough statistics to study the efficiency in 3 dimensions (p_T, η, ϕ), we used pure pion sample selected by a very tight *dE/dx* cut ($|n\sigma_\pi| < 0.5$) to study the η and ϕ dependence. The TOF matching efficiency from pure electron sample from photon conversion and π^0 Dalitz decay was served as a standard of the absolute value of the efficiency. A weight on η and ϕ dimensions was applied to the electron sample to address the difference in η and ϕ distribution with π sample. The efficiency from π sample was scaled to match with the one from electron sample. In this analysis, we used following function to parameterize the scale factor as a function of p_T :

$$f(x) = \frac{1 + ax + bx^2}{c + \exp\{(x - d)/f\}} \tag{3.10}$$

The fit result is shown in Fig. 3.17 and the difference was also included in the systematic uncertainty.

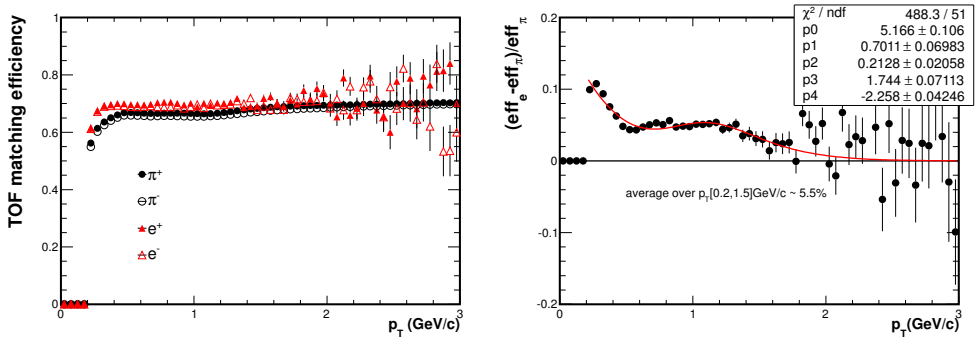

Figure 3.17 (Left) TOF matching efficiency from π sample and photon conversion sample in Au +Au 200GeV minimum bias collision. They difference is shown in the right panel. The red line depicts a fit by function 3.10.

The TPC efficiency and TOF matching efficiency were both studied and applied in 3 dimensions. TPC efficiency was calculated in 20×36 η, ϕ bins and 50 MeV p_T bin, while TOF matching efficiency was studied in 20×60 η, ϕ bins and 50 MeV p_T bin. The centrality dependence was also taken into account for Au+Au collisions by comparing the p_T distribution of TPC and TOF efficiency from different centralities with minimum bias.

PID efficiency The PID efficiency included efficiencies of $1/\beta$, $n\sigma_e$ and *ndEdxFits* cut. $1/\beta$ cut and *ndEdxFits* efficiencies were studied by the pure π sample and the pure electron sample from real data, their difference was considered as systematics uncertainty. The pure electron sample was also used to study the $n\sigma_e$ distribution for electrons as mention in section 3.3.3 which provided us the $n\sigma_e$ cut efficiency directly from the fit result.

Figure 3.18 and 3.19 summarize the single electron efficiency for Au+Au and p+p data sample.

3.5.2 Momentum resolution and energy loss

The momentum resolution and energy loss for TPC tracks was studied by embedding sample with the full detector simulation. Figure 3.20 shows the reconstructed electron p_T^{rec} probability distribution at a given input p_T^{MC} from embedding sample for Au +Au 200 GeV collision. The distribution was parametrized with a double Crystal-Ball function, defined in Eq. 3.11:

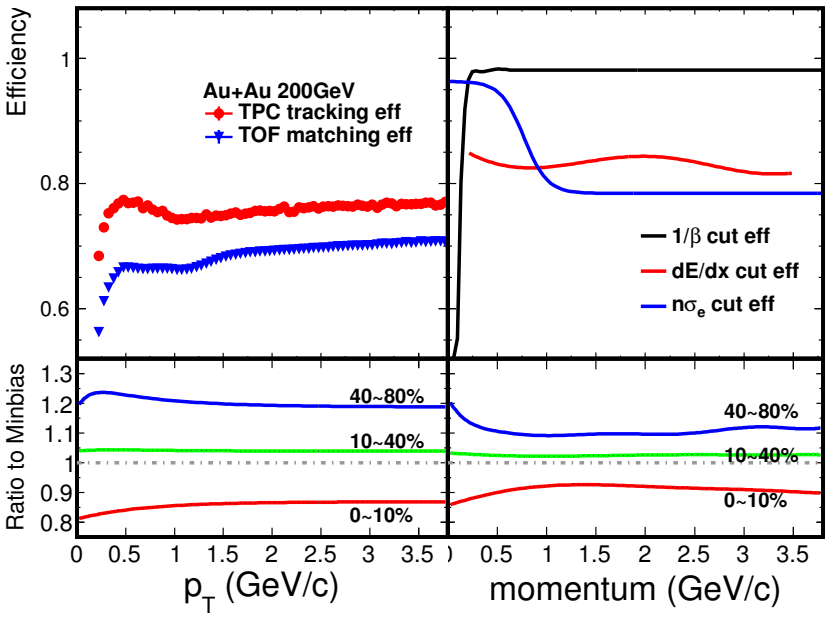

Figure 3.18 Summary of the single track efficiency for Au+Au 200 GeV.

$$P(p_T^{rec}, p_T^{MC}) \propto \begin{cases} A \times (B - R)^{-n}, & R < -\alpha \\ e^{-R^2/2}, & -\alpha < R < \beta \\ C \times (D + R)^{-m}, & R > \beta \end{cases} \tag{3.11}$$

and

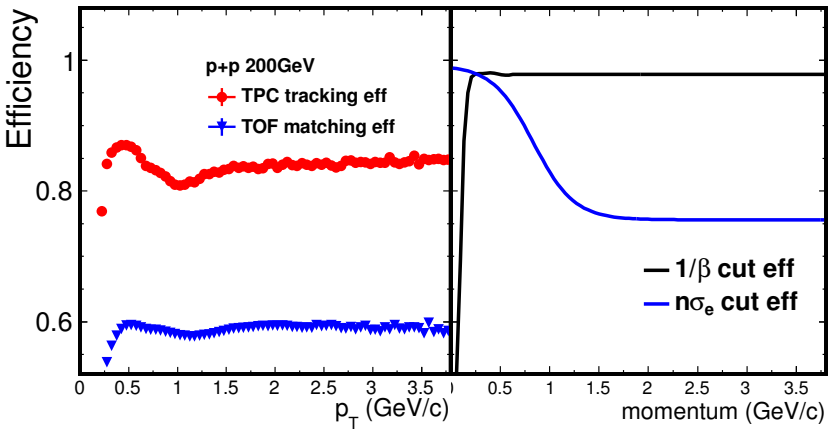

Figure 3.19 Summary of single track efficiency for p+p 200GeV.

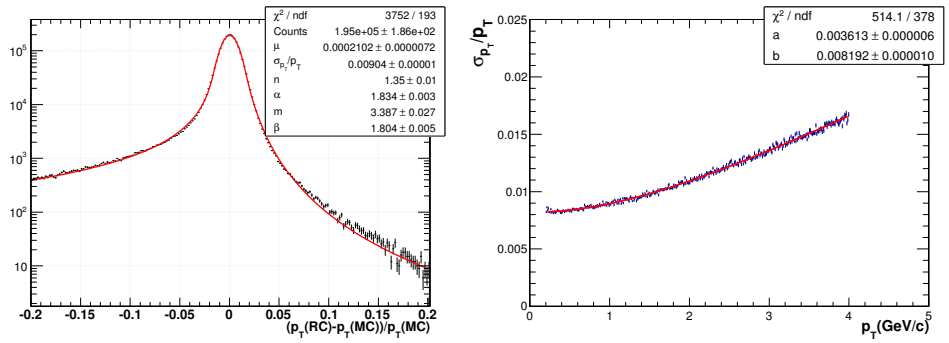

Figure 3.20 Left panel shows distribution of p_T^{rec} probability at a given input p_T^{MC} from the embedding sample with 1% momentum resolution. Right panel show the momentum resolution from the embedding sample.

$$
\begin{aligned}
A &= (\frac{n}{|\alpha|})^n \times e^{-\alpha^2/2} \\
B &= \frac{n}{|\alpha|} - |\alpha| \\
C &= (\frac{m}{|\beta|})^m \times e^{-\beta^2/2} \\
D &= \frac{m}{|\beta|} - |\beta| \\
R &= (\frac{p_T^{rec} - p_T^{MC}}{p_T^{MC}} - \mu)/\frac{\sigma_{p_T}}{p_T}
\end{aligned}
\tag{3.12}
$$

where $n = 1.35$, $\alpha = 1.83$, $m = 3.39$, $\beta = 1.80$, for Au+Au 200 GeV minimum bias collision in year 2011. $\mu = 0.0002$ which is slightly shifted because the STAR tracking assumed every track is pion when accounted for the energy loss. σ_{p_T}/p_T was used as a measure of the p_T resolution. It was assumed to follow:

$$
(\frac{\sigma_{p_T}}{p_T})^2 = (a \times p_T)^2 + (\frac{b}{\beta})^2; \quad \beta = \frac{p}{E} \sim \frac{p_T}{\sqrt{p_T^2 + m^2}} \tag{3.13}
$$

Figure 3.20 right panel shows σ_{p_T}/p_T distribution from the embedding sample. Due to various distortion effect in the TPC detector under the high luminosity RHIC environment, it is very challenging to precisely reproduce the momentum resolution by the embedding sample. We used a data-driven method: we tuned parameters a and b in Eq. 3.13 to get the best match to the J/ψ signal distribution. Finally the two parameters were chosen to be $a = 0.0060\, c/GeV$ and $b = 0.0083$.

3.5.3 Pair efficiency and acceptance

The pair efficiency was evaluated by Monte Carlo folding method from the single track efficiency. We used two methods for folding the pair efficiency in Au+Au analysis:

1. virtual photon decay method, which virtual photons with M_{ee} and p_T distributions from the cocktail simulation and a flat η, ϕ distribution. Then the virtual photon is isotropically decay into electron pairs.

2. cocktail method, where we used cocktail as input. The input particles decay into electron pairs following their decay kinematics. The heavy flavor quark decay process, suck like open charm decay and Drell-Yan process were from PYTHIA model. This method will be discussed in detail in next section.

In relativistic heavy-ion collision, we have difficulties in separating the electrons from heavy flavor quark decay and those produced from medium. Furthermore, the contribution from heavy flavor decays remains unclear due to the possible medium modification effect in heavy-ion collision. The two methods served as two extreme approaches of decay kinematics in the Au+Au collision : virtual photon method is close to the decay kinematics of medium; cocktail method handles the heavy flavor decays through PYTHIA model which is similar to the process in p+p collision.

The single electron efficiency was folded in for each daughter track in full 3D (p_T, η, ϕ) momentum space. Their momenta were smeared by the momentum resolution and energy loss effect (see section 3.5.2). The pair efficiency was calculated and applied in 2 dimension (M_{ee} vs p_T), within STAR acceptance ($|y_{ee}| < 1$, $p_T^e > 0.2GeV/c$, $|\eta_e| < 1$). The difference between the two methods is small and we included it in systematic uncertainty. The photon conversion rejection cut efficiency was calculated by π^0 Dalitz decay embedding sample and included in the pair efficiency, shown in Figure 3.21. Figure 3.22 summarizes the pair efficiencies as a function of M_{ee} used in this analysis.

In this analysis, the dielectron transverse mass (m_T) spectra and their inverse slope parameters were also studied in Au+Au collision, which need to be corrected for the detector acceptance. The acceptance correction was calculated as following:

$$\varepsilon_{pair}^{acc} = \frac{dN/dM_{ee}/dy(p_T(e) > 0.2GeV/c,\ |\eta_e| < 1,\ |y_{ee}| < 1)}{dN/dM_{ee}/dy(|y_{ee}| < 1)} \tag{3.14}$$

In Figure 3.23, the acceptance correction was calculated by the two methods mentioned previously for Au+Au 200 GeV minimum bias collisions. There is a huge difference

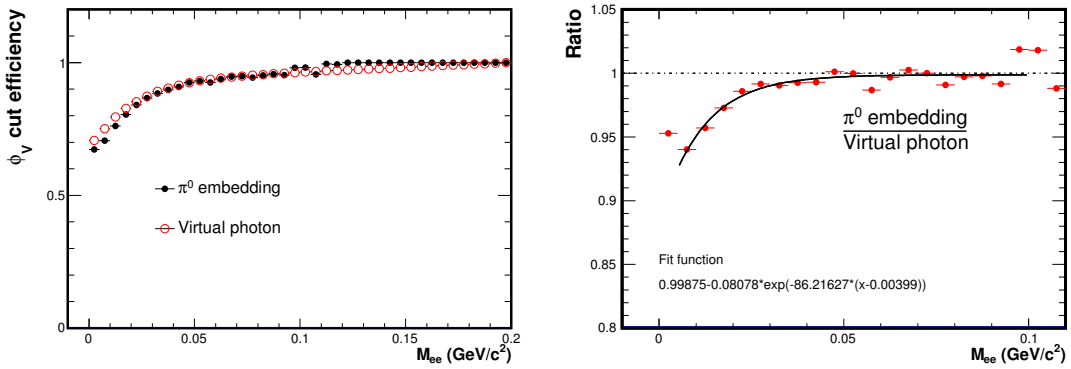

Figure 3.21 ϕ_V efficiency calculated by π^0 Dalitz decay embedding and virtual photon method (left) and also their comparison (right).

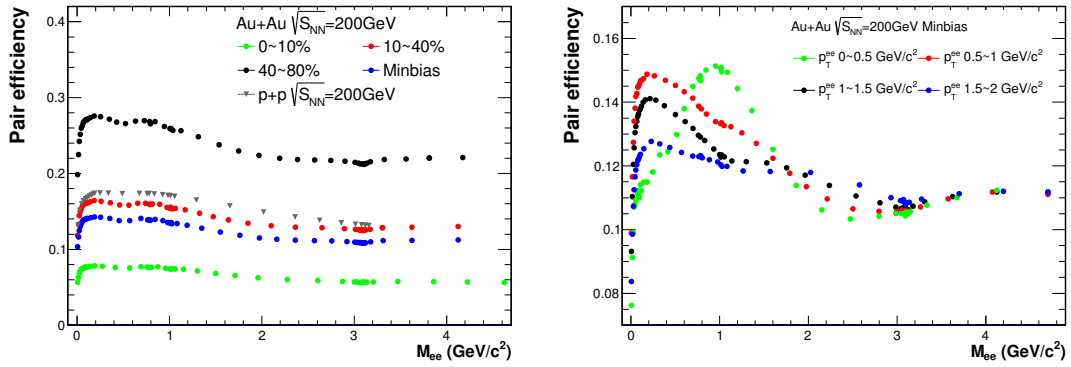

Figure 3.22 (Left) Pair efficiency for different centralities Au+Au collision and p+p collision. (Right) p_T^{ee} dependence of pair efficiency in Au+Au minimum bias collision.

between the two method, especially in intermediate mass region (IMR). It is because dielectrons mainly come from charm contribution in this mass region. The two methods treat the correlation between the daughter pairs quite differently. In virtual photon method, the correlation between the decay daughters is come from decay kinematics itself. While in cocktail method, since the charm component is simulated by PYTHIA, the daughter pairs carry the strong correlation inherited from charm pairs. Therefore, it leads to some difference in the acceptance for dielectron pairs. We took the difference between the two methods as systematic uncertainty in inverse slope parameters of transverse mass spectra due to leak of knowledge of this two processes in heavy-ion collisions.

3.5.4 Trigger efficiency, trigger bias and vertexing bias

The event sample selection is required by a VPD coincidence and a valid primary vertex. Due to the inefficiency of the VPD detector in p+p collisions, we need correct

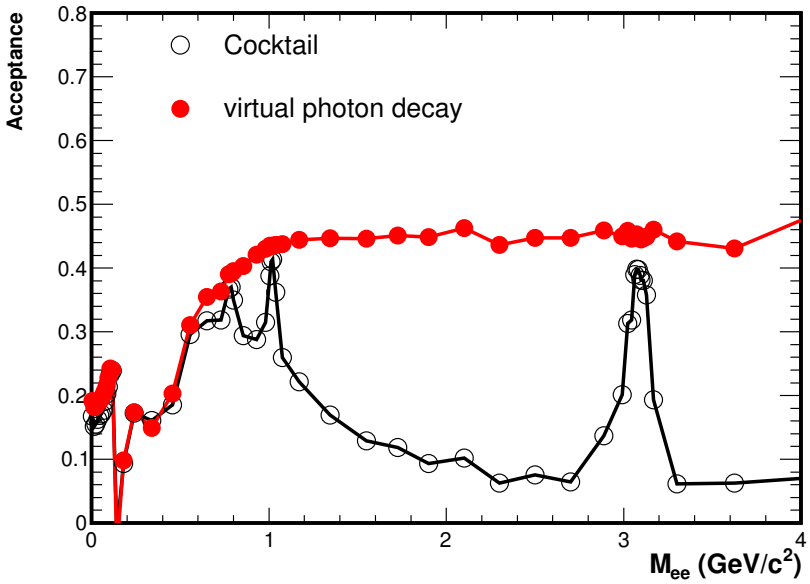

Figure 3.23 Acceptance correction calculated by virtual photon method and cocktail method for Au+Au 200GeV collision.

the possible bias of trigger and vertex selection. In this analysis, trigger bias correction factor was taken from [1], the number is 64% with 8% systematic uncertainty.

3.5.5 The total correction factors for dielectron spectra

Finally, the dielectron continuum raw yield within STAR acceptance are corrected as following:

$$Y(M_{ee}, p_T) = \frac{N_{raw}(M_{ee}, p_T)}{dM_{ee}dy \times \varepsilon_{pair}(M_{ee}, p_T)} \times f_{triggerbias} \tag{3.15}$$

, where N_{raw} is the dielectron raw yields within STAR acceptance, ε_{pair} is the efficiency correction and $f_{triggerbias}$ is the trigger bias factor (~64% in p+p collisions, ~1 in Au+Au collisions).

3.6 Hadronic cocktails

The dielectron signals observed in experiment are produced from various sources during the system evolution. After chemical freeze out, dielectron pairs from long life meson and hadron decays contribute mainly to the dielectron signal. These components, which is usually called “Hadronic cocktails”, can be well understood by measuring the corresponding decay channels. In this analysis, cocktails contain contributions from decays and Dalitz decays of π^0, η, η', ρ (only in p+p collisions), ω, ϕ, J/ψ, ψ', $c\bar{c}$, $b\bar{b}$

and Drell-Yan (DY) production.

The cocktail for p+p collision is taken from STAR published result [1], and the charm cross section is updated to $d\sigma/dy|_{y=0} = 171 \pm 26$ μb with respect to the newest published result from STAR [61]. Figure 3.24 left panel shows the input hadron p_T spectra for p+p collision. Figure 3.25 shows the cocktail for p+p collisions.

We used the similar cocktail simulation methods for Au+Au 200 GeV collision as we used in p+p collision [1]. The cocktail simulation only contains the hadron form-factor decays in the vacuum at freeze-out. For the ρ component, we included a vacuum ρ calculation only when comparing data with cocktails including the vacuum ρ. We assumed a flat rapidity distribution within $|y| < 1$ for the input hadrons. Table 3.6 lists the dN/dy (or cross-section), branching ratios, uncertainty and reference for all input sources. The hadron spectra measured by STAR and PHENIX were parameterized by the simultaneous Tsallis Blast-Wave (TBW) model fit [62]. Figure 3.24 right panel shows the TBW fit results for all input hadron spectra except J/ψ. The cocktail input for J/ψ was taken from the measurement by the PHENIX collaboration [2]. For light hadrons, the TBW fit provides good parameterizations to these measure spectra. The same core TBW parameters was used to predicted the spectral shapes for these components without measurements (e.g. low p_T η, η', ω).

The correlated charm, bottom and Drell-Yan contributions were studied by PYTHIA simulation [63] and scaled by the number of binary collisions (N_{bin}) in Au+Au collisions. We used PYTHIA 6.419 with settings: MSEL=1, PARP(91) ($\langle k_\perp \rangle$) = 1.0 GeV/c and PARP(67) (parton shower level) = 1.0, which was tuned to match STAR measured charmed meson spectrum in p+p collisions [64]. The input charm cross section was also taken from the charmed meson measurement.

The detector resolution was also taken into account by smearing the daughter electron's momentum with the method discussed in section 3.5. Finally, the dielectron pair mass distributions from the sources are normalized by branching ratios and the measured dN/dy. Figure 3.26 shows the cocktails for Au+Au 200 GeV minimum collisions.

The cocktails were also simulated in difference centrality bins (0~10%, 10~40% and 40~80%). The similar TBW model fit was applied to parameterize the measured spectra in corresponding centrality bins. For hadron without measurement, the TBW predictions were used as the input p_T distributions. We used the relative pion yields (R_π) with respect to minimum bias collisions (0~80% centrality bin) as scale factor for the input dN/dy in each centrality bin. The correlated charm contributions were scaled by the relative number of binary collisions ($R_{N_{bin}}$). Table 3.7 summarizes all these scale

source	B.R.	dN/dy or σ	Uncertainty	Reference
$\pi^0 \to \gamma ee$	1.174×10^{-2}	98.5	8%	STAR [65, 66]
$\eta \to \gamma ee$	7×10^{-3}	7.86	30%	PHENIX [2]
$\eta' \to \gamma ee$	9×10^{-4}	2.31	100%	PHENIX [2]
$\rho \to ee$	4.72×10^{-5}	9.88	42%	STAR [67]
$\omega \to ee$	7.28×10^{-5}			
$\omega \to \pi^0 ee$	7.7×10^{-4}	9.87	33%	STAR [68]
$\phi \to ee$	2.95×10^{-4}			
$\phi \to \eta ee$	1.15×10^{-4}	2.43	10%	STAR [69]
$J/\psi \to ee$	5.94×10^{-2}	2.33×10^{-3}	15%	PHENIX [70]
$\psi' \to ee$	7.72×10^{-3}	3.38×10^{-4}	27%	PHENIX [71, 72]
$c\bar{c} \to ee$	1.03×10^{-1}	$d\sigma^{c\bar{c}}/dy = 171\mu b$	15%	STAR [61]
$b\bar{b} \to ee$	1.08×10^{-1}	$\sigma_{pp}^{b\bar{b}} = 3.7\mu b$	30%	Pythia [63]
Drell-Yan	3.36×10^{-2}	$\sigma_{pp}^{DY} = 42nb$	30%	Pythia [63]

Table 3.6 Inputs of various cocktail components for Au+Au 200 GeV minimum bias collisions.

centrality	π dN/dy	R_π	$\langle N_{bin} \rangle$	$R_{N_{bin}}$
0~80%	98.49	1	291.90 ± 20.46	1
0~10%	279.2	2.834	941.24 ± 26.27	3.224
10~40%	131.1	1.331	391.36 ± 30.21	1.341
40~80%	30.45	0.309	56.62 ± 13.62	0.194

Table 3.7 Scale factors for centrality dependent cocktails.

factors.

3.7 Systematic uncertainty

In this analysis, the systematic uncertainty was split into two main parts: from data analysis which is highly correlated with M_{ee} , and from efficiency which is uncorrelated with M_{ee}.

The systematic uncertainties source from data analysis are listed below:

1. Background, including uncertainties of the acceptance factor for like-sign background ($M_{ee} < M_{th}$)and the normalization for mixed event background ($M_{ee} > M_{th}$).

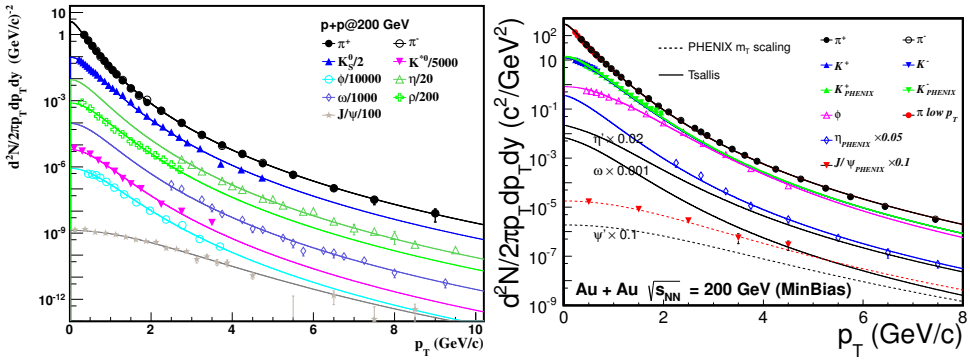

Figure 3.24 Left panel: the invariant yields of measured mesons fit with the Tsallis functions in p +p 200 GeV collision [1]. The solid lines represent the fit. Right panel: invariant yields of mesons in Au+Au collision at $\sqrt{s_{NN}} = 200$ GeV. The solid lines represent the simultaneous Tsallis Blast-Wave (TBW) fit to the measure data points and TBW predictions for η, η', ω with the same set of fit parameters. The dash lines depict the same parametrization to the measures J/ψ spectrum and the predicted ψ' spectrum as in [2].

2. Like-sign residue, the uncertainty from the fit to parameterize the difference between like-sign and mixed event background in mass region $M_{ee} > M_{th}$.

3. Hadron contamination.

The uncertainty from acceptance factor was come from difference between 1D (p_T) and 2D (M_{ee}vs p_T) acceptance factor correction as mentioned in section 3.4.1. The normalization uncertainty was studied by changing the normalization regions around which used in the analysis, and the difference was taken as systematic uncertainty. For p+p collision the normalization regions was changed to 0.3~0.8 GeV/c^2 and 0.5~1.2 GeV/c^2, while in Au+Au collision it was changed to 0.75~1.75 GeV/c^2 and 1.25~3 GeV/c^2. As mentioned in section 3.4.2, we used function 3.5 to parameterized the correlated residue and subtract it additionally from the foreground. The 68% confidence level of the fit was taken as systematic uncertainty (Figure 3.12).

Hadron contamination was studied by mixing pure hadron sample into electron sample, we called it the mixed sample. The hadron sample was weighted by the ratio of hadron yield over electron yield from the electron purity study (Figure 3.27). The particles in the mixed sample were randomly paired with each other. There are three condition: e-e pairs, this is dielectron signal; e-h and h-h contamination pairs. Then the same background subtraction was done to the mixed sample. Finally, we used function 3.16 to parameterize yields of the contamination pairs and calculated its contribution to systematic uncertainty (Figure 3.28).

Finally, we combined all these source and plotted the systematic uncertainty from data analysis in Fig 3.29 and 3.30.

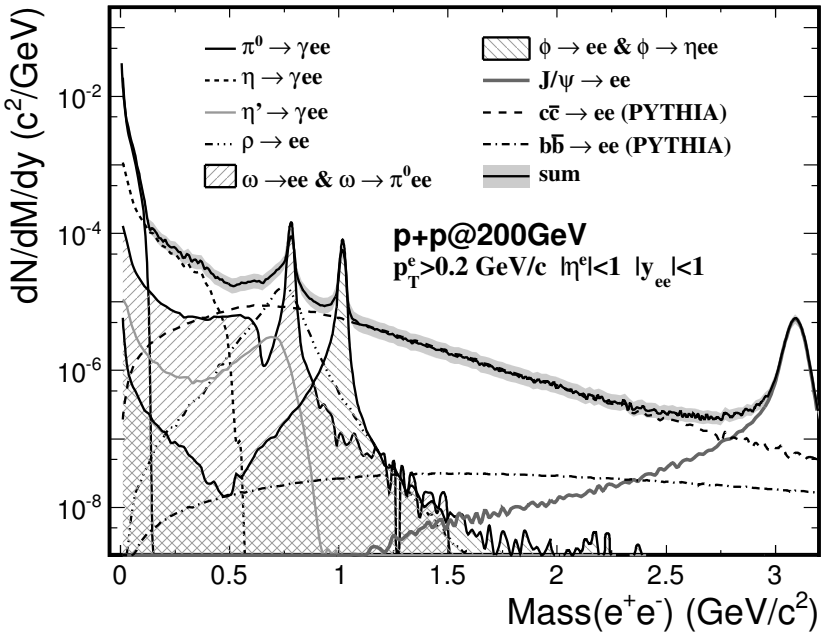

Figure 3.25 Cocktails for p+p 200 GeV minimum bias collision.

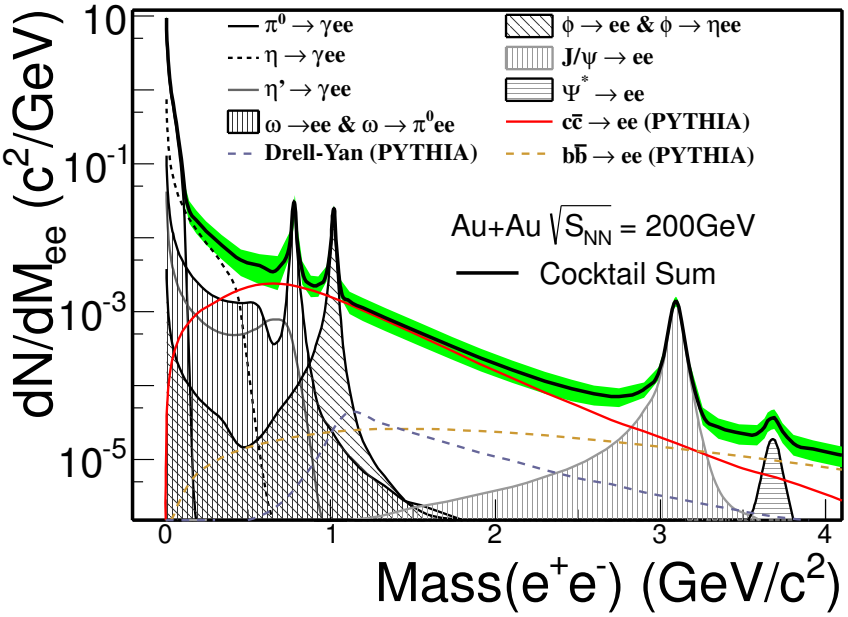

Figure 3.26 Cocktails for Au+Au 200GeV minibias collision. The green band depicts the systematics uncertainty.

		Au+Au	p+p
	component	Systematic Uncertainty	Systematic Uncertainty
TPC	nHitsFits (15-25)	3.2%	0.9%
	dca (1.5-0.5cm)	1.4%	1.8%
	ndEdxFits	2%	2%
TOF	matching	5.5%	8%
	$1/\beta$	1.7%	0.7%
total		7.3%	8.3%
pair total		14.6%	16.6%

Table 3.8 Systematic uncertainty from efficiency.

$$f(x) = \begin{cases} a_0 + a_1 x + a_2 x^2 + a_3 x^3 & x < x_{th} \\ b\exp(cx) & x > x_{th} \end{cases} \tag{3.16}$$

The efficiency uncertainties have already been discussed in section 3.5. Table 3.8.

3.8 Combine the Au+Au results from year 2010 and year 2011

To achieve better statistics, we combined the results from year 2010 and year 2011 together for Au+Au 200 GeV collisions. The year 2010 result has already published in PRL [73].

3.8.1 Comparison

Before combined the data, we compared the results from year 2010 and year 2011. Figure 3.31 and 3.32 show the comparison of the two years results in different centralities and p_T regions. The efficiency correction was done separately for each year's results by the same process mentioned in section 3.5. The results are reported within the STAR acceptance ($|y_{ee}| < 1, p_T^e > 0.2GeV/c, |\eta_e| < 1$) and show good consistency with each other within uncertainty.

3.8.2 Combination

Year 2010's and year 2011's results were combined statistically and systematically. For the 0~10% centrality bin, since Run 10 have dominate statistics, we didn't combine Run10 and Run11 data in this centrality to ensure the systematics uncertainty is under control.

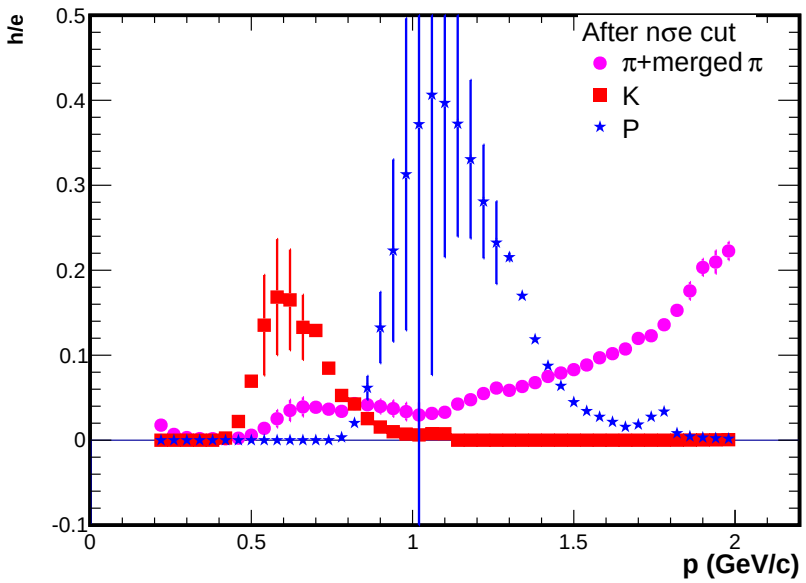

Figure 3.27 Ratio of hadron yields over electron yields as a function of momentum.

The data points and their statistical errors were combined by standard error propagate formula, see Eq. 3.17, where *Y ~ yield, w ~ weight and δ ~ statistic uncertainty.*

$$
\begin{aligned}
Y_{com} &= w_{10} \times Y_{10} + w_{11} \times Y_{11} \\
\Delta_{com} &= \sqrt{w_{10}^2 \delta_{10}^2 + w_{11}^2 \delta_{11}^2} \\
w_{10} &= \frac{1/\delta_{10}^2}{(1/\delta_{10}^2 + 1/\delta_{11}^2)} \\
w_{11} &= \frac{1/\delta_{11}^2}{(1/\delta_{10}^2 + 1/\delta_{11}^2)}
\end{aligned}
\tag{3.17}
$$

We combined systematic uncertainty of efficiency (which is uncorrelated vs mass) and other systematic uncertainty sources (which is correlated vs mass) separately. The method used to calculate the combined error are list below:

- efficiency uncertainty (relative error) uncorrelated source, summed by quadratic sum: $\sigma_{com} = \sqrt{w_{10}^2 \sigma_{10}^2 + w_{11}^2 \sigma_{11}^2}$.
- other uncertainty source (relative error) correlated source, summed by direct sum : $\epsilon_{com} = w_{10}\epsilon_{10} + w_{11}\epsilon_{11}$.
- total systematic uncertainty : $\Sigma_{com} = \sqrt{\sigma_{com}^2 + \epsilon_{com}^2} \times Y_{com}$.

The combined results are plotted in different centrality and p_T bins and compared with cocktail simulation in Fig and .

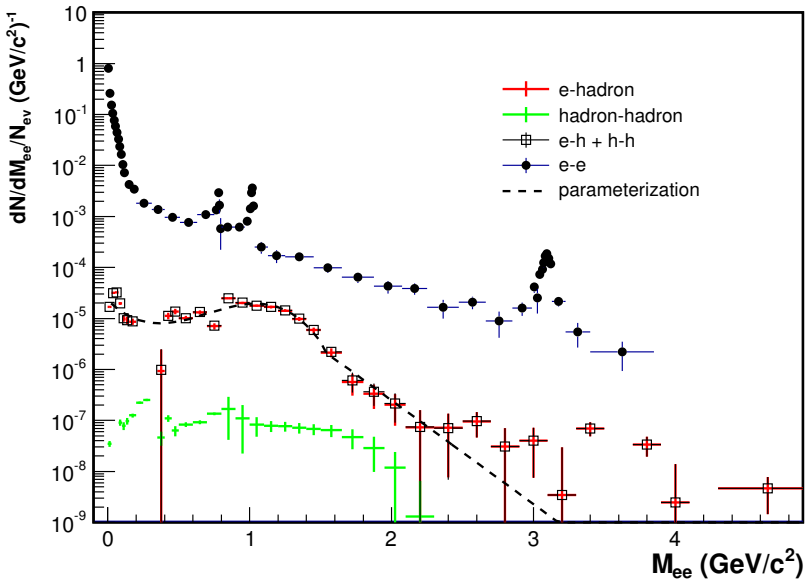

Figure 3.28 Yields of dielectron signal pairs, e-h and h-h contamination pairs.

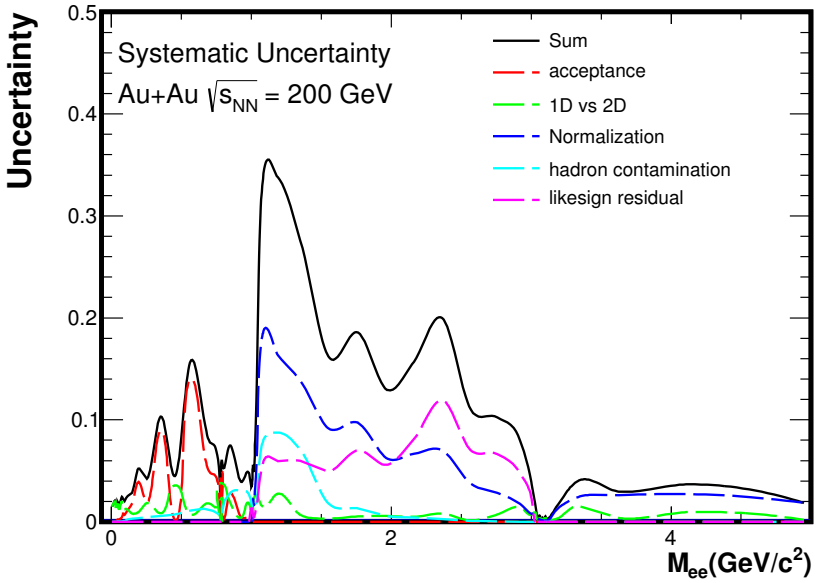

Figure 3.29 Systematic uncertainty from data analysis for Au+Au 200GeV minimum bias collision.

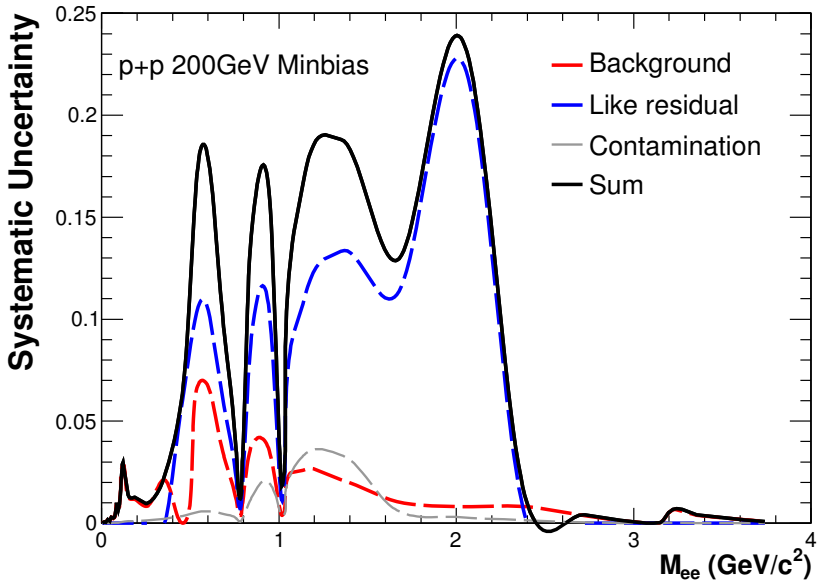

Figure 3.30 Systematic uncertainty from data analysis for p+p 200GeV minimum bias collision.

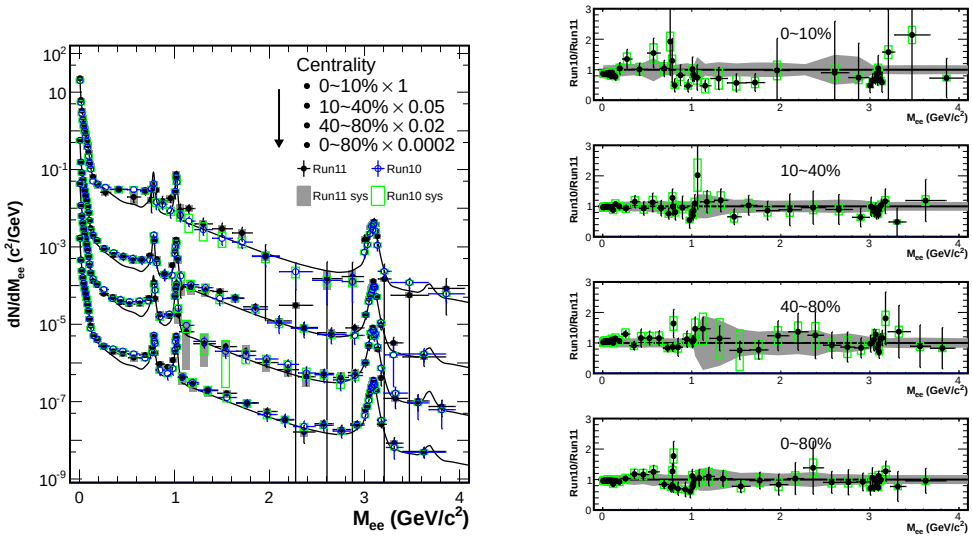

Figure 3.31 Comparison between Au+Au results from year 2010 and year 2011 in different centralities. Right panel shows the ratio of year 2010's results over year 2011's result. The green box depicts the systematic uncertainty for year 2010's results, and the grey bar represents the systematic uncertainty for year 2011's results.

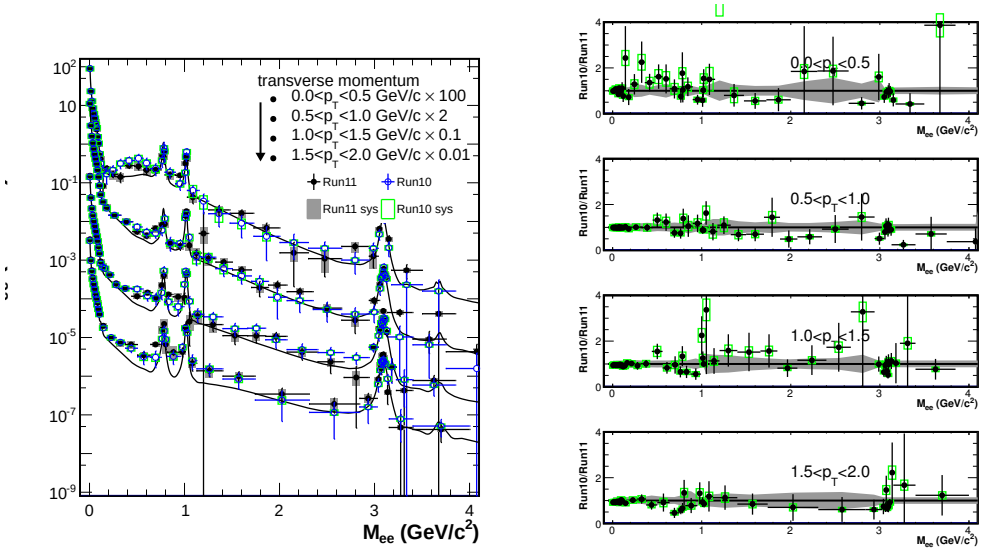

Figure 3.32 Comparison between Au+Au results from year 2010 and year 2011 in different p_T bins in minimum bias collision. Right panel shows the ratio of year 2010's results over year 2011's result. The green box depicts the systematic uncertainty for year 2010's results, and the grey bar represents the systematic uncertainty for year 2011's results.

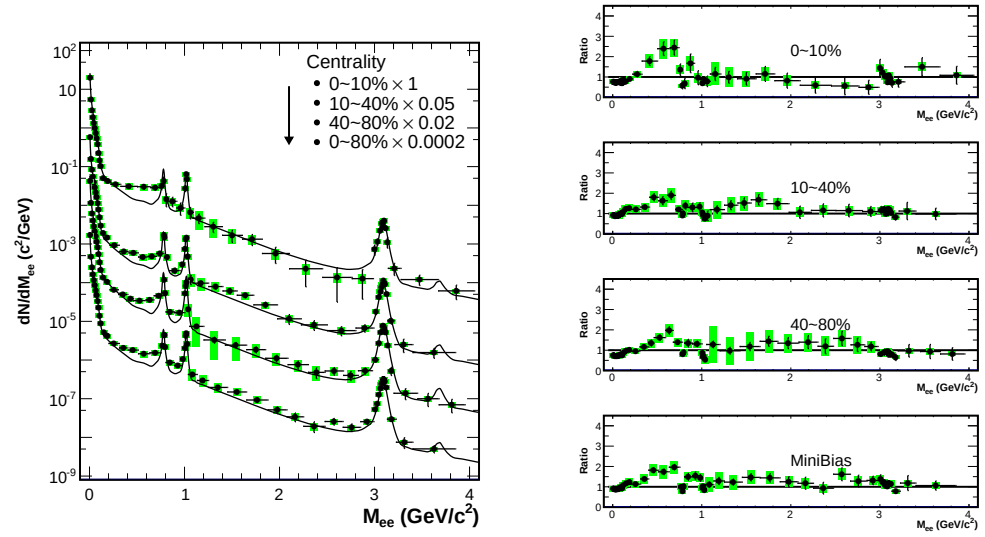

Figure 3.33 Combined results in different centrality bins for Au+Au 200 GeV collision from year 2010 and year 2011. The green bars depicts the systematic uncertainties.

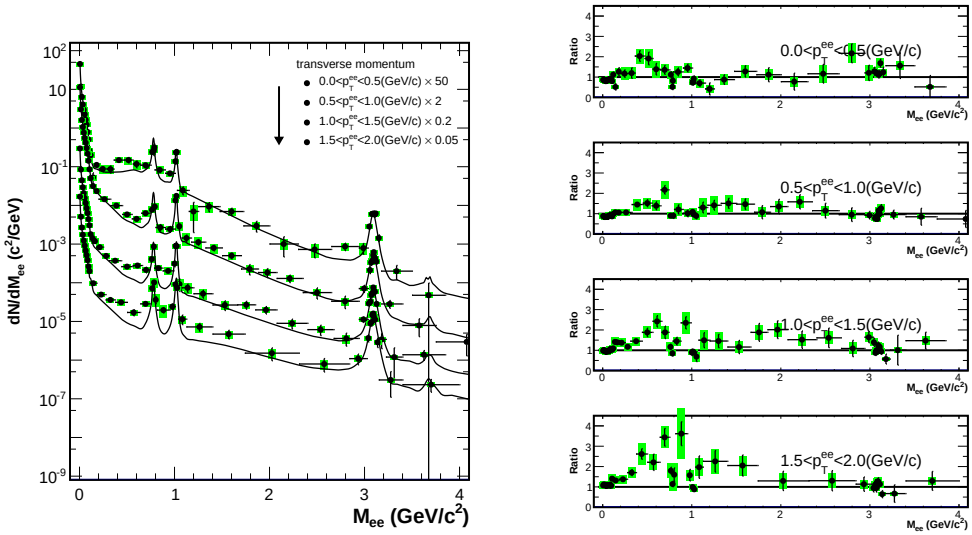

Figure 3.34 Combined results in different p_T bins for Au+Au 200 GeV minimum bias collision from year 2010 and year 2011. The green bars depicts the systematic uncertainties.

Chapter 4 Result and discussion

4.1 Dielectron production in 200 GeV p+p collisions at STAR

Figure 4.1 shows the dielectron invariant mass spectra from 200 GeV p+p collisions taken in year 2012. The cocktail is taken from the STAR published result [1], and the charm cross section is updated to $797 \pm 210\,(stat.)\,^{+208}_{-295}\,(sys.)\ \mu b$ with respect to the newest published result from STAR [64]. The cocktail simulation can reproduce the new preliminary result very well. With a full TOF coverage and more data taken, year 2012 result has greatly improved statistics which is ~7 times more than STAR previously published result [1]. The large statistics new results at p+p 200 GeV provide a better baseline for Au+Au collisions.

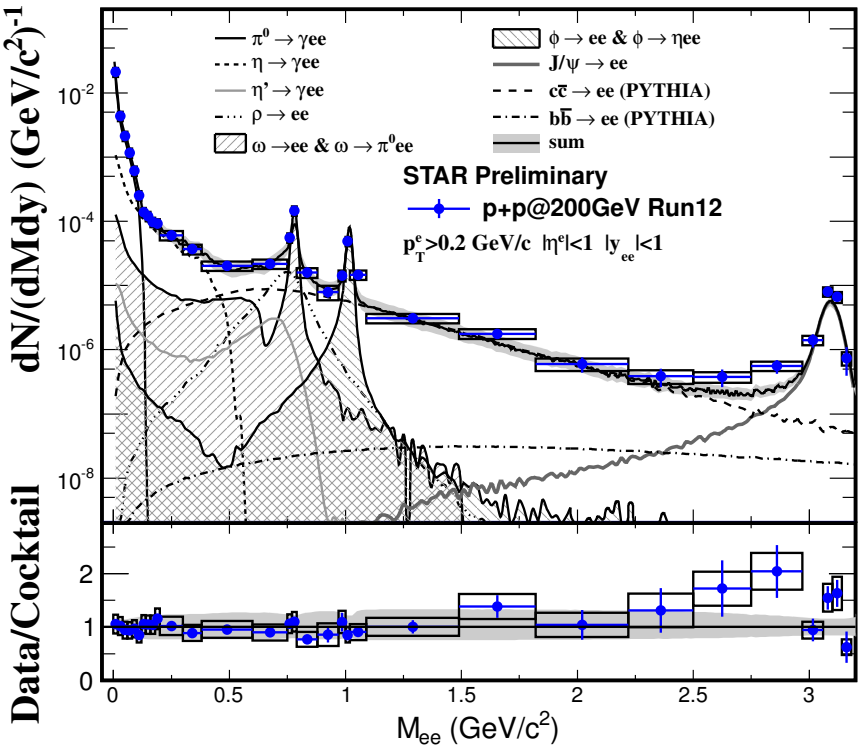

Figure 4.1 Invariant mass spectra from $\sqrt{s}$ = 200 GeV p+p collisions taken from year 2012. The black open box represents systematic error from data while the grey band depicts systematic uncertainty of cocktail.

4.2 Dielectron production in 200 GeV Au+Au collisions at STAR

In this section, we report the results from Au+Au collisions at $\sqrt{s_{NN}}$ = 200 GeV. All results in this section are taken from the combined year 2010 and year 2011 data (as described in Sec. 3.8). The dielectron signals were obtained as described in Sec 3.4.5. The dielectron yields were corrected for the dielectron reconstruction efficiency. All the results were measured in the STAR acceptance ($p_T^e > 0.2\,GeV/c$, $|\eta^e| < 1$ and $|y_{ee}| < 1$) .

4.2.1 Dielectron invariant mass spectra

The p_T integrated efficiency corrected dielectron mass spectrum dN/dM_{ee} at midrapidity $|y_{ee}| < 1$ in the STAR acceptance from 0~80% Au+Au minimum bias collisions at $\sqrt{s_{NN}} = 200$ GeV is shown in Fig. 4.2. The data are compared to the hadronic cocktail simulations without the vacuum ρ contribution. The ratios of data over cocktail simulations are shown in the bottom panels. The green band around unity indicates the uncertainties on the cocktail calculations, which are mainly determined by the uncertainties on the dN/dy and decay branching ratios for each individual source as discussed in Sec 3.6. We consider ρ mesons are strongly coupled with the medium in Au+Au collisions, thus we don't include it in default hadronic cocktail calculations. We left its contribution to the theory model calculations which will be discussed in following subsections. The correlated charm contribution as described in Sec 3.6 is taken from PYTHIA simulation and scaled by the number of binary collisions ($N_{\rm bin}$).

In the LMR region, an enhancement of $1.66\pm0.06(stat.)\pm0.24(sys.)\pm0.33(cocktail)$ is observed with respect to the cocktail without vacuum ρ contribution in the mass region of 0.3~0.76 GeV/c^2, when comparing the measured data points to the hadronic cocktail. The enhancement cannot be fully explained by the expected vacuum ρ contribution. The enhancement observed here is significantly lower than what has been reported from the dielectron measurement from PHENIX experiment [2]. And the new results with Hadron Blind Detector (HBD) from PHENIX group confirm the enhancements between STAR and PHENIX in 20-80% centrality bins are consistent [3].

In the IMR region, the cocktail is dominant with the contribution from correlated charm pair decays based on PYTHIA simulations. The cocktail simulations can generally describe the data points reasonably well within uncertainty, although the data seem to sit a bit higher then the expected cocktail contribution, leaving some room for contributions from other sources. However, the uncertainties on data points and cocktail

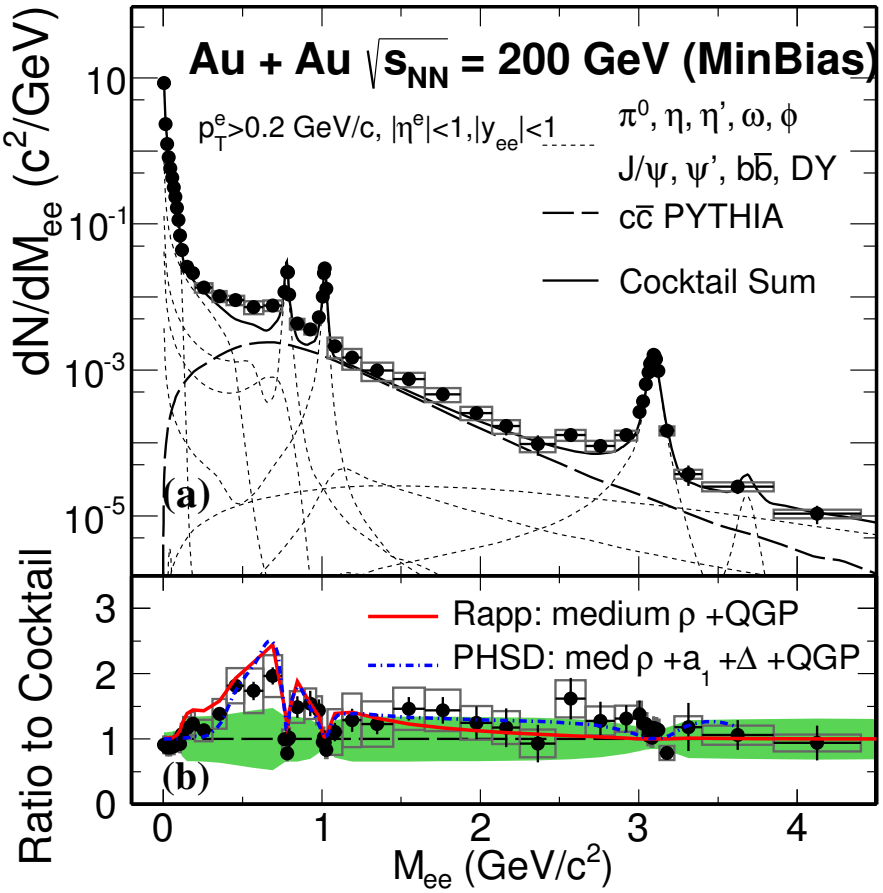

Figure 4.2 (a) Invariant mass spectra, (b) ratio of data to cocktail. Two model calculations are also included. In panel (b), the grey box represents the systematic uncertainty from data while the light green band shows the systematic uncertainty from cocktail.

are large which makes it impossible to distinguish any other contributions if it is there. The current uncertainty on the charm production cross section $d\sigma^{c\bar{c}}/dy$ at mid-rapidity which need to be used for normalization is around 40%. More precise measurements on both the total charm cross section as well as the correlation in Au+Au collisions are needed to conclude any other source contribution, such as QGP thermal radiation, in this mass region.

4.2.2 Comparison to models

Restoration of the spontaneously broken chiral symmetry will lead to modification to the vector meson (ρ meson in the leading role) spectral functions, which are accessible via dilepton measurements in heavy ion collisions. Thus, studying the chiral symmetry properties of the QCD medium created in heavy ion collisions is one of the major motivations of dilepton production measurements. There are two scenarios commonly used to address the effect due to the chiral symmetry restoration: (a) drop of the pole mass or

degeneracy of vector and axial-vector mesons due to the reduced $\langle q\bar{q}\rangle$ condensate [25]. (b) broadening of the spectral function due to mean body collisions in the vector-meson dominance [35, 74]. Both scenarios will introduce an enhancement in the mass region below the ρ mass when comparing to the spectral function in vacuum. High precision data from NA60 suggested that the enhancement in the low mass dilepton spectrum is consistent with in-medium broadening of the ρ spectral function instead of a dropping of its pole mass hypothesis at the SPS energy [41]. It is expected that the hadronic medium at top RHIC energy is similar to that created at the SPS energy.

The QGP contribution to dileptons has been often calculated perturbatively via the Born $q + \bar{q}$ annihilation at the leading order. Various approached have been studied to take into account high order contributions at the finite $T - \mu_B$ environment [75]. The QGP contribution is expected to become sizable at $M > 1.5\,GeV/c^2$ at the top RHIC energy due to the well established partonic phase [30].

There have been many theory calculations for the dielectron production at RHIC. We chosen two theory calculations from different groups to compare with out data:

Model I: from Rapp's group.

We chose one model calculation from Rapp [76], which is a *macroscopic effective many-body theory model*. In this model, dilepton production in the hadronic medium is calculated via electromagnetic correlators based on the Vector-meson Dominance Model (VDM) approach. This model assumes that the hadronic medium reaches thermal equilibrated. Therefore, the dilepton rates are determined by the ρ meson propagetor in this medium, which depends on the interactions of the ρ with mesons and baryons in this medium at finite T and μ_B. The calculation results shows the resulting broadened ρ spectral function is mostly due to the interactions with baryons rather than mesons [10, 77–79]. Thus total baryon density of the medium is one critical factor in determining the dielectron yield in heavy ion collisions.

The QGP contribution is calculated via perturbative $q\bar{q}$ annihilation with some improved corrections. It has been demonstrated in these calculations the dilepton rates from the hadronic medium and from partonic medium should be equivalent at T_c, which is called "parton-hadron" duality [10]. The final resulting dielectron yields from observation are calculated via the integral over the whole space-time evolution for this medium.

Model II: Parton-Hadron String Dynamic (PHSD) transport model.

The PHSD model is a *microscopic transport dynamic model.* It is consisted of the off-shell evaluation of vector mesons and the explicit partonic phase contributions in the

early stage of the medium evaluation as well as the dynamics of hadronization [80, 81]. The model allows for a microscopic study of various dilepton production channels in non-equilibriumous medium. In the hadronic sector, the PHSD is equivalent to the HSD transport approach that has been used for the description of pA and AA collisions from SIS to RHIC energies. It fairly reproduces the measured hadron yields, rapidity distributions and transverse momentum spectra [27, 82]. The PHSD model incorporates off-shell dynamics for vector mesons and a set of vector-meson spectral functions that covers possible scenarios for their in-medium modifications. In the scope of the one- and two-particle interactions, dilepton radiation by the constituents of the strongly interacting QGP proceeds via following elementary processes: the basic Born $q + \bar{q}$ annihilation mechanism, gluon Compton scattering ($q(\bar{q}) + g \rightarrow \gamma^* + q(\bar{q})$) and quark and anti-quark annihilation with the gluon Bremsstrahlung in the final state ($q+\bar{q} \rightarrow g+\gamma^*$). Dilepton production in these partonic channels is calculated with off-shell partons using the phenomenological parameterizations for the quark and gluon propagators and their interaction strength in QGP.

In the LMR (M_{ee}<1.1 GeV/c^2), the comparison is focused on model calculations with different hadronic medium modification scenarios for ρ mesons (Fig 4.3): no modification vacuum ρ contribution (left panel) and in-medium ρ with broadening mass spectral function (middle panel). The QGP radiation contributions are also included in comparison. The comparison with PHSD model is also shown (right panel). Figure 4.4 provides a more clearly view by comparing these model calculation with the dielectron excess spectra (data subtracted with the default cocktail). The grey bars depict the systematic uncertainties from data analysis, while the green brackets depict the total systematic uncertainties including those from data and cocktail. Considering the highly correlated systematic errors across all data points, we utilized the modified χ^2-test (see Appendix A) to quantify the consistency between data and model calculations, the results are summarized in Table 4.1. From the χ^2-test, the vacuum ρ + QGP scenario in Rapp's implementation is cleared ruled out by our data. The calculations including the broadened ρ scenario + QGP contribution from both Rapp and PHSD show reasonable agreements to our data, and the Rapp's calculation is more favored. The correlated charm also has a sizable contributions starting from 0.5 GeV/c^2, while our cocktail still uses the $N_{\rm bin}$ scaled correlated charm contribution from PYTHIA simulation. Therefore precision knowledge of correlated charm contribution in heavy ion collision will provide further improvement on distinguish between different scenarios .

In Figure 4.5, we compare our measured dielectron results in minimum bias col-

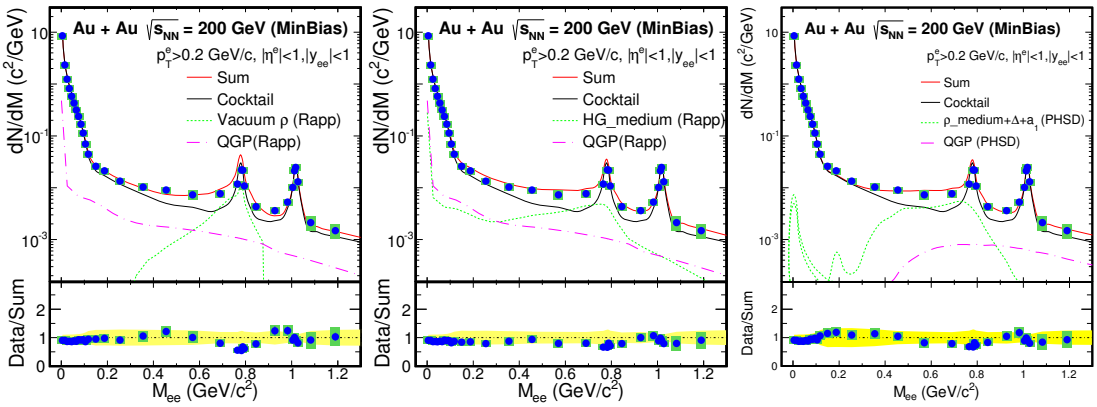

Figure 4.3 Dielectron mass spectrum in the low mass region measured in the STAR acceptance compared to the model calculations from Rapp for two different scenario: (a) vacuum ρ (left panel), (b) in-medium ρ in width broadening scenario (middle panel). The QGP contribution is also included. The right panel shows the comparison with PHSD model.

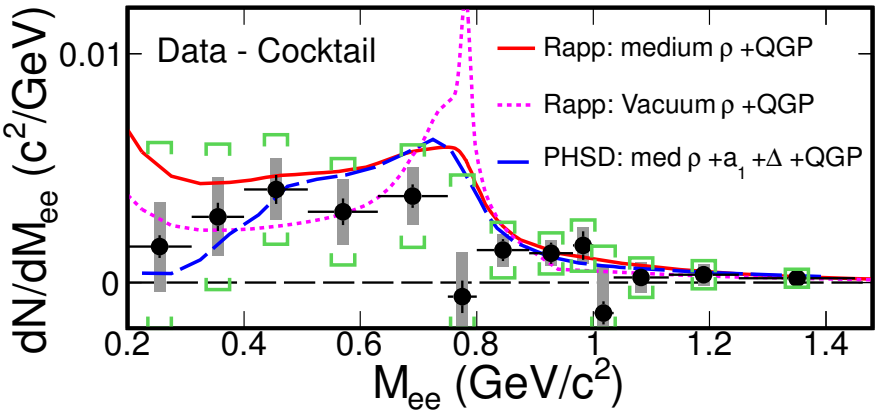

Figure 4.4 Excess spectra in LMR from $\sqrt{s_{NN}}$ = 200 GeV Au+Au minimum bias collisions and comparison with theory calculations. The green brackets depict the total systematic uncertainties including those from data and cocktail.

lisions to two model calculations in the full mass range. In upper panels of both plots, model calculations of the hadronic medium and QGP contributions were added to the default cocktail simulation and compared to the measured data. The bottom panels show ratios of data to the total sum contribution. In the LMR, the consistency between these two models and our data has already been addressed by the χ^2-test mentioned previously. In the IMR, the correlated charm contribution is dominant. However, we still do not have a clearly understanding about the correlated charm contribution. It is a bit early to argue the consistency between data and models.

4.2.3 p_T and centrality dependence

To gain more insight on the underlining physics, we also studied the p_T dependence as will as the centrality dependence of dielectron yields and compared them to

Model:	χ^2/ndf	p-value
Rapp: vaccum ρ +QGP	41.0/8	2.1×10^{-6}
Rapp: broadened ρ +QGP	8.2/8	0.41
PHSD: broadened ρ +QGP	16.4/8	0.037

Table 4.1 χ^2/ndf for model calculations compare to the excess data in mass region: 0.3-1.0 GeV/c^2.

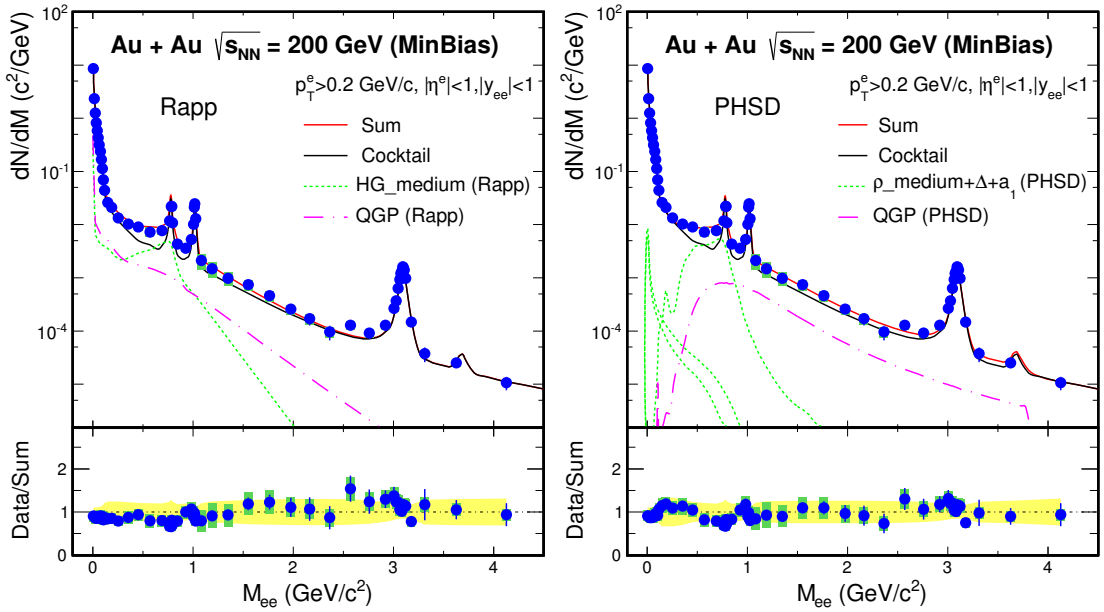

Figure 4.5 Dielectron mass spectrum in 200 GeV minimum bias Au + Au collisions compared to the hadron cocktail plus the hadronic medium and partonic QGP contributions calculated from Rapp's (left) and PHSD (right) models.

the hadronic cocktail simulations and model calculations. Figure 4.6 shows dielectron yields measured in each individual p_T region as well as the hadronic cocktail on the left plot, and the ratios of data over cocktail simulation on the right plot. Theoretical model calculations in each p_T window are included to compare to the measured data as well. The dielectron spectra were also studied in various centrality bins (0~10%, 10~40%, 40~80%). Figure 4.7 shows similar plots for centrality depended dielectron spectra as the p_T depended plots in Fig 4.6. Please note that the correlated charm contributions, which becomes to have sizable contribution from 0.5 GeV/c^2 and is dominant above 1 GeV/c^2 , were all taken from the N_{bin} scaled PYTHIA simulations with charm pair production cross section of $\sigma_{c\bar{c}} = 0.80 \pm 0.36$ mb. In a general view, one can see the enhancement factor with respect to the hadronic cocktail shows a weak p_T and centrality dependence. Both theoretical models are able to reasonably describe the LMR enhancement in all p_T bins and centrality bins.

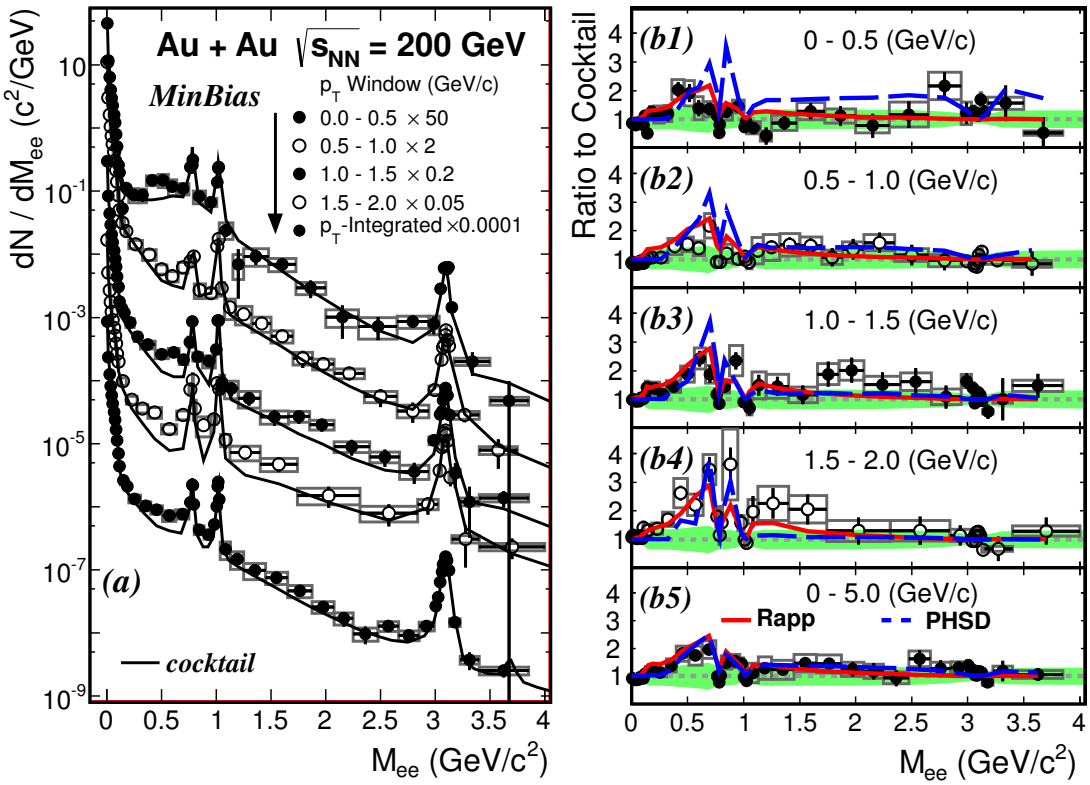

Figure 4.6 Left panel shows dielectron invariant spectra in different p_T ranges. The solid curves represent the hadronic cocktail. Right panel shows the ratio of data to cocktail in different p_T ranges. The green band represents the systematic uncertainty of cocktail.

To qualify the p_T and centrality dependence of the LMR excess, we separate the LMR into three mass regions: 0.3~0.76 (ρ-like), 0.76~0.8 (ω-like) and 0.98~1.05 (ϕ-like) GeV/c^2. The ratios of data w.r.t the hadronic cocktail were calculated in these three mass regions for each p_T and centrality bins and were shown in Fig 4.8 upper plot panel (a) (for centrality) and (b) (for p_T). One can see that the hadronic cocktail can reproduce the dielectron yield in the ω-like and ϕ-like regions. In the ρ-like region, a significant excess is observed in each p_T and centrality bins and the ratios of data w.r.t hadronic cocktail show weak dependence on N_{part} (centrality) and p_T. The bottom plot of Fig 4.8 shows the integrated excess yields (yields subtracted with cocktail) in the ρ-like region scaled by $1/N_{part}$. The ω-like and ϕ-like regions without cocktail subtraction scaled by $1/N_{part}$ are also included in the plot as comparison. The dielectron yields in the ω-like and ϕ-like regions show a N_{part} scaling while the excess yields increase faster than N_{part} with centralities. The dashed curve is a power fit ($\propto N_{part}^{a}$) to the excess yield/N_{part} in the ρ-like region, the fit shows $a = 0.48 \pm 0.11$ (stat. +uncorrelated sys.), indicating the dielectron yields in the ρ-like region are sensitive to the QCD medium dynamics, as expected from ρ medium modifications in theoretical

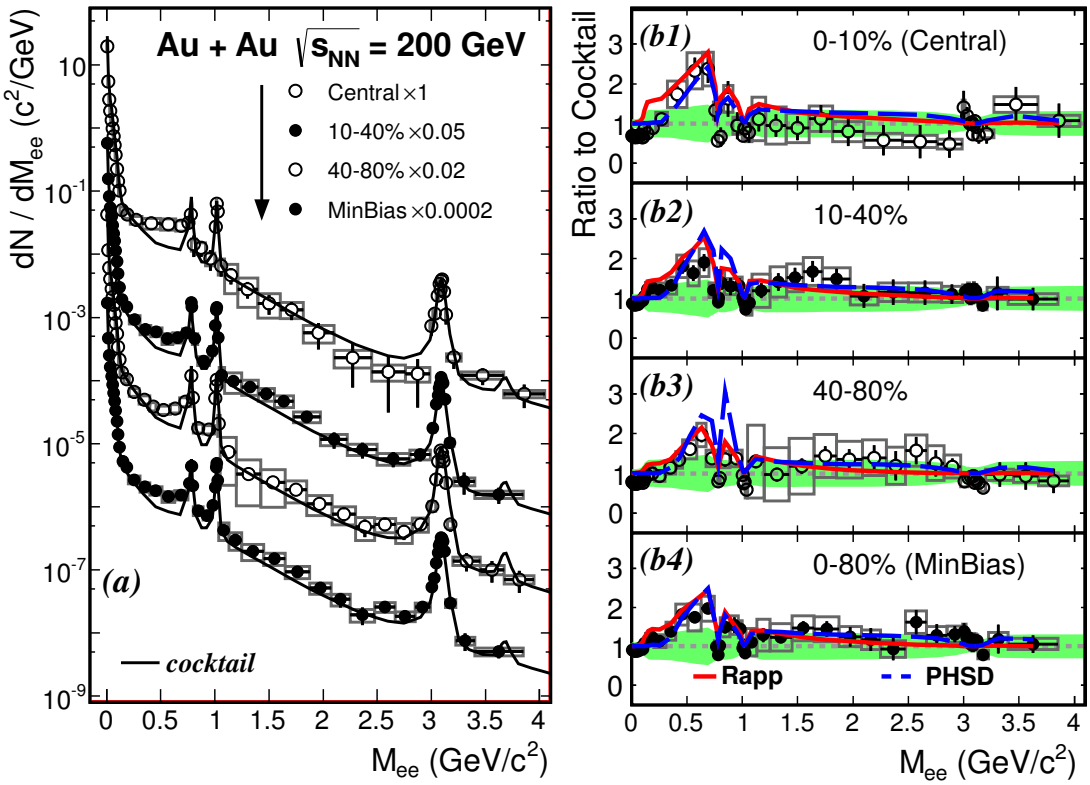

Figure 4.7 Left panel shows dielectron invariant mass spectra in different centralities. The solid curves represent the hadronic cocktail. The charm contribution is calculated by PYTHIA and scaled by $N_{\rm bin}$. Right panel shows the ratio of data to cocktail in different centralities. The green band represents the systematic uncertainty of cocktail.

calculations [76, 83]. The enhancement factor and dielectron yields in the ρ-like region for each p_T and centrality bins are summarized in Table 4.2 and 4.3.

p_T region (GeV/c)	Yield ($\times 10^{-3}$)	Yield/Cocktail
0-0.5	$1.15 \pm 0.09 \pm 0.20$	$1.61 \pm 0.12 \pm 0.28$
0.5-1.0	$1.58 \pm 0.07 \pm 0.27$	$1.48 \pm 0.06 \pm 0.25$
1.0-1.5	$0.67 \pm 0.03 \pm 0.11$	$1.69 \pm 0.08 \pm 0.27$
1.5-2.0	$0.24 \pm 0.02 \pm 0.04$	$2.40 \pm 0.15 \pm 0.40$

Table 4.2 The p_T dependence of dielectron yields in the STAR acceptance and the enhancement factor with respect to the hadronic cocktail in the mass region of 0.3−0.76 GeV/c^2.

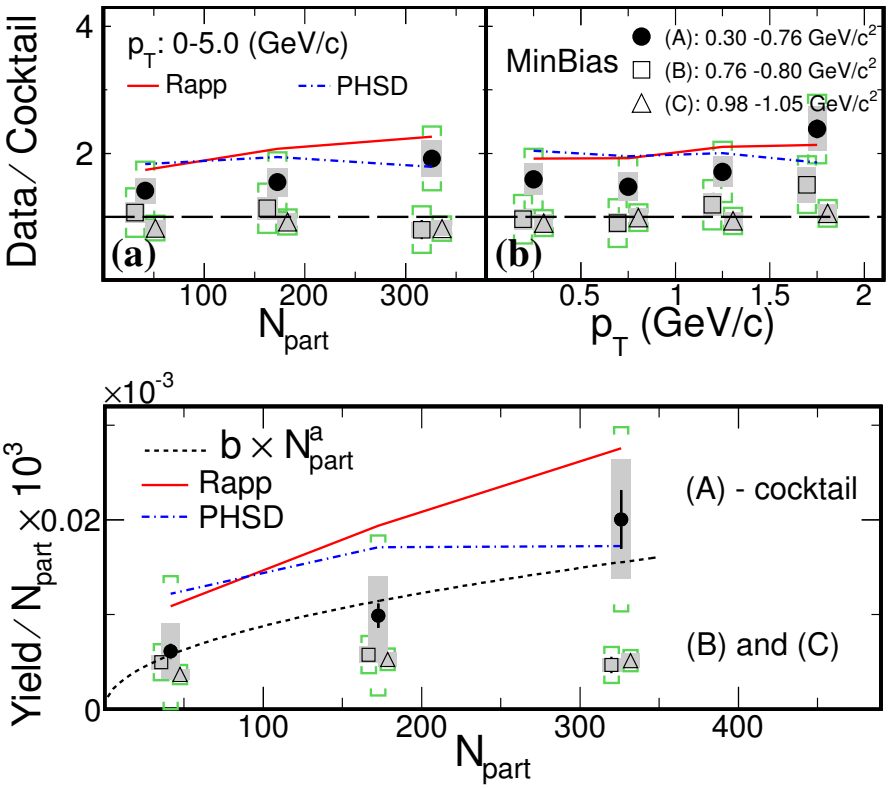

Figure 4.8 Panel (a) and (b) shows the integrated dielectron yields in mass regions of 0.3-0.76(ρ-like), 0.76-0.80(ω-like) and 0.98-1.05(ϕ-like) GeV/c^2 as a function of centrality and p_T. Panel (c) shows the yields scaled by N_{part} for the ρ-like with cocktail subtraction, and the ω-like and ϕ-like without cocktail subtraction. The dashed curve is a power-law fit to the yield/N_{part} for the ρ-like region subtracted by cocktail. Systematic uncertainties from data are shown as grey boxes, while the green brackets represent the total systematic uncertainties including the cocktail contribution. The ω-like and ϕ-like data points are slightly displaced horizontally for clarity.

Centrality	Yield ($\times 10^{-3}$)	Yield/Cocktail
0-10%	$13.64 \pm 1.01 \pm 2.07$	$1.92 \pm 0.14 \pm 0.29$
10-40%	$4.82 \pm 0.22 \pm 0.71$	$1.55 \pm 0.07 \pm 0.23$
40-80%	$0.87 \pm 0.04 \pm 0.12$	$1.42 \pm 0.06 \pm 0.20$
0-80%	$3.87 \pm 0.13 \pm 0.57$	$1.66 \pm 0.06 \pm 0.24$

Table 4.3 The centrality dependence of dielectron yields in the STAR acceptance and the enhancement factor with respect to the hadronic cocktail in the mass region of 0.3−0.76 GeV/c^2.

4.2.4 Correlated charm contributions

In Fig 4.9, we overlay the dielectron mass spectra from minimum bias and most central (0-10%) collisions. The spectra are scaled by the number of participant nucleons (N_{part}) and are plotted in the upper panel, and the ratio between them is plotted in the bottom panel. In the upper plot, charm contribution based on different assumptions on the correlations are also include as two dash lines. The dashed line depicts the correlated

charm from PYTHIA, while the dot-dashed line assumes a fully randomized azimuthal correlation between charm pairs and the p_T suppression factor on single electron spectrum from RHIC measurement is also included [84]. The measured ratio starts from unity in the π^0 and η mass region, indicating the production with N_{part} scaling. It begins to increase in mass region 0.5-1 GeV/c^2 towards the N_{bin} scaling. This is due to the fact that correlated charm contribution starts to dominate in this mass region and the charm quark production at RHIC energy is expected to follow the N_{bin} scaling. The hadronic medium also has a significant contribution in this mass region and is expected to increase faster than N_{part} [76, 83]. In the IMR region, the ratio shows a moderate deviation from the N_{bin} scaling (2.0σ deviation for the data point at 1.8-2.8 GeV/c^2). The difference in mass region 1-3 GeV/c^2 indicates a potential de-correlating effect on charm pairs while traversing the QCD medium or other contribution from medium (e.g thermal radiation). To qualify the difference, we preformed exponential fits to the mass spectra in central and minimum bias collisions and the resulting slopes differ by ~ 1.5σ.

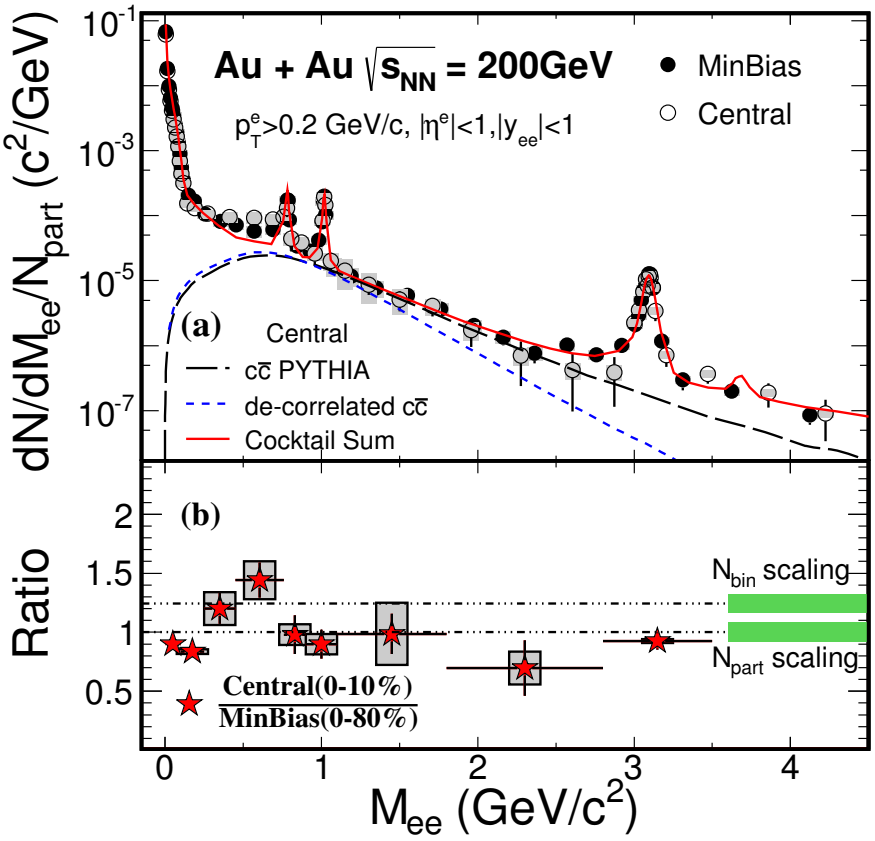

Figure 4.9 (a) Dielectron invariant mass spectra from minimum bias (0-80%) and central (0- 10%) collisions. The spectra are scaled by the number of participant nucleons (N_{part}). The solid line represents the hadronic cocktail for central collisions. (b) The ratio of N_{part} scaled dielectron yields between the central and minimum bias collisions. Systematic uncertainties are shown as the grey box.

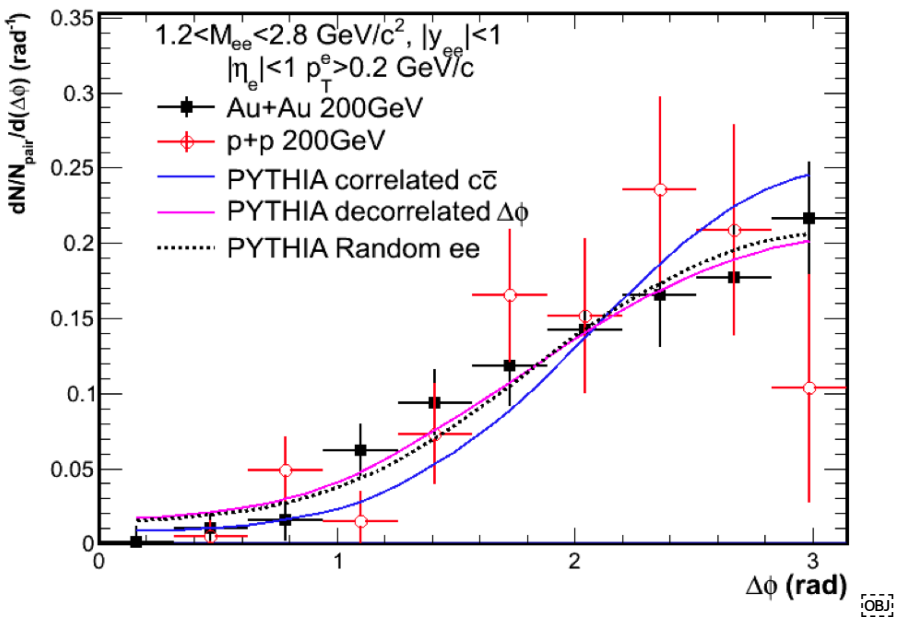

Figure 4.10 Dielectron azimuthal correlation distributions in IMR from p+p and Au+Au minimum bias collision at 200 GeV. The lines are from PYTHIA simulation with different assumption of the correlations of the $c\bar{c}$ pairs.

Figure 4.10 shows the dielectron azimuthal correlation distributions in IMR from p+p and Au+Au minimum bias collision at 200 GeV. The lines depict the PYTHIA simulation based on three different assumptions of correlation between charm pair:

1. Correlated $c\bar{c}$, which is the default set used in the cocktail simulation. The correlation between $c\bar{c}$ pairs is similar as p+p collisions.

2. Decorrelated $\Delta\phi$, only the azimuthal correlation between daughter electrons and positrons are broken which corresponds the case that there is no azimuthal correlation between the parent $c\bar{c}$ pairs.

3. Random $e\bar{e}$, the correlation between daughters are broken completely.

Current measurements can not be distinguished by different PYTHIA simulations due to large statistical uncertainties. Future measurement of $e-\mu$ correlations with the new installed detectors MTD and HFT, will provide a clean study of the correlation of charm-anticharm in high energy heavy ion collisions.

4.2.5 Low mass vector meson yields

Figure 4.11 shows the invariant mass distribution of the vector meson ω and ϕ from $\sqrt{s_{NN}}$ = 200 GeV Au+Au minimum bias collisions. The signal spectra are reconstructed

by subtracting the normalized mix-event unlike-sign background (Sec 3.4.2) from foregound same-event unlike-sign distribution. Two methods were used to fit the invariant mass distributions.

- Method I: A Breit-Wigner function plus a second order polynomial function. The second order polynomial function was used to describe the residual background.

- Method II: Using mass distributions (line-shapes) directly from the cocktail simulations to fit the signal. As described in Sec 3.5 and 3.6, the detector momentum resolution in the cocktail simulation was tune to match the J/ψ signal in the data.

Firstly we used Method I and Method II to fit the data distributions with all parameters left free to extract the mass positions and widths from measured data. And different background functions and different fit ranges were used to estimated the systematics uncertainty for Method I. Because the life time of ω and ϕ mesons are much longer than the typical lifetime of the medium created in high energy heavy ion collision, the observed signals from the detector are dominant by the freeze-out ω and ϕ. Therefore, although vector mesons can be modified in the hot medium due to the interactions with the medium, the observed ω and ϕ spectra will have little sensitivity to see a medium modification effect. We compared the widths and mass positions of ω and ϕ signals from Method I with the values from PDG, as well as those from our full GEANT simulations (from the cocktail distributions), shown in Fig 4.12. The mass positions of ω and ϕ mesons from data generally agree with the PDG values, with a slight shift towards lower values. This is mainly because that the STAR tracking procedure only accounts for the energy loss assuming pions and this is also well reproduced in the full GEANT simulation. The widths of the signals is larger than the PDG value as expected, due to the detector resolution effect. The full simulations results also reproduce the observed signal widths for ω and ϕ mesons.

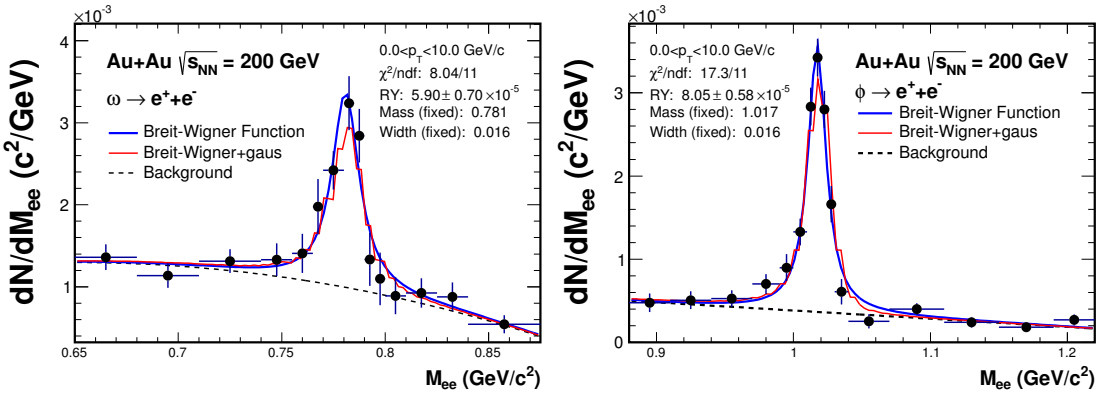

Figure 4.11 ω and ϕ meson invariant mass distribution from $\sqrt{s_{NN}}$ = 200 GeV Au+Au minimum bias collisions after the combinatorial background subtracted by using the mixed-event method. The blue and red lines depict two functions used for the signals in the fit. A second order polynomial function is used to describe the residual correlated background.

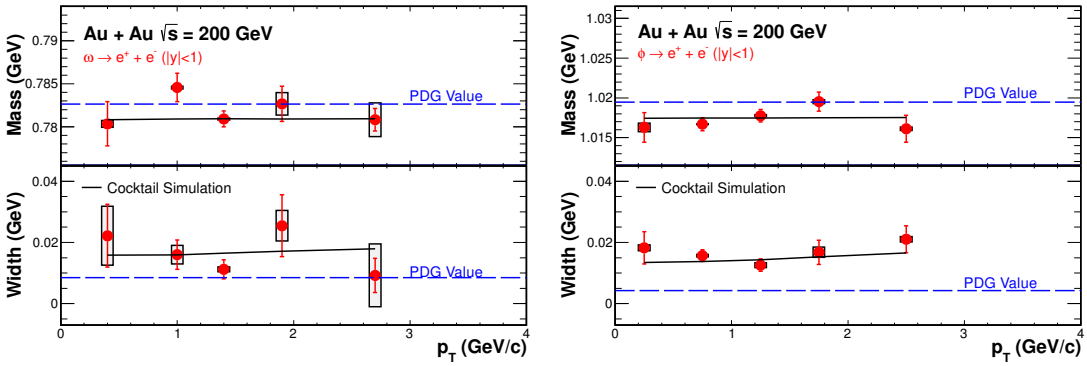

Figure 4.12 The widths and mass positions of ω and ϕ signals from data compared to the values from the PDG and the full GEANT simulation. Boxes on the data points depict the systematic uncertainties.

Figure 4.13 show the ω and ϕ invariant mass distributions in different p_T region. We used Method I with fixed widths and mass positions according to our full GEANT simulations to extracted the raw yields. The systematic uncertainty of the raw yields is estimated by changing background function and fit range. The difference between the free parameter fit by Method I and Method II is also included in the systematic uncertainty. The invariant mass distributions of J/ψ are also included in the fit as a consistency check for the methods. Finally, the raw yields are corrected for the detector acceptance and efficiency. Figure 4.14 show the final p_T differential invariant yields for ω and ϕ from Au+Au minimum bias collisions at $\sqrt{s_{NN}}$ = 200 GeV at mid-rapidity ($|y| < 1$). The final systematic uncertainties include the detector efficiency uncertainty and the raw signal uncertainty in extracting the raw meson yield. The ϕ spectrum from the dielectron decays is consistent with the previous measured result from hadron decay

channel ($\phi \rightarrow K^+ + K^-$)[69]. Also included in the figure are the Tsallis Blast-Wave model [62] fit to the previous ϕ spectrum and a prediction to the ω spectrum with the same set of parameters obtained from the simultaneous fit to all available light hadrons (Sec 3.6). The TBW prediction describes the measured ω spectrum well. The measured *dN/dy* for ω is $8.461 \pm 0.677(stat.) \pm 1.589(sys.)$, and *dN/dy* for ϕ meson is $2.200 \pm 0.098(stat.) \pm 0.335(sys.)$.

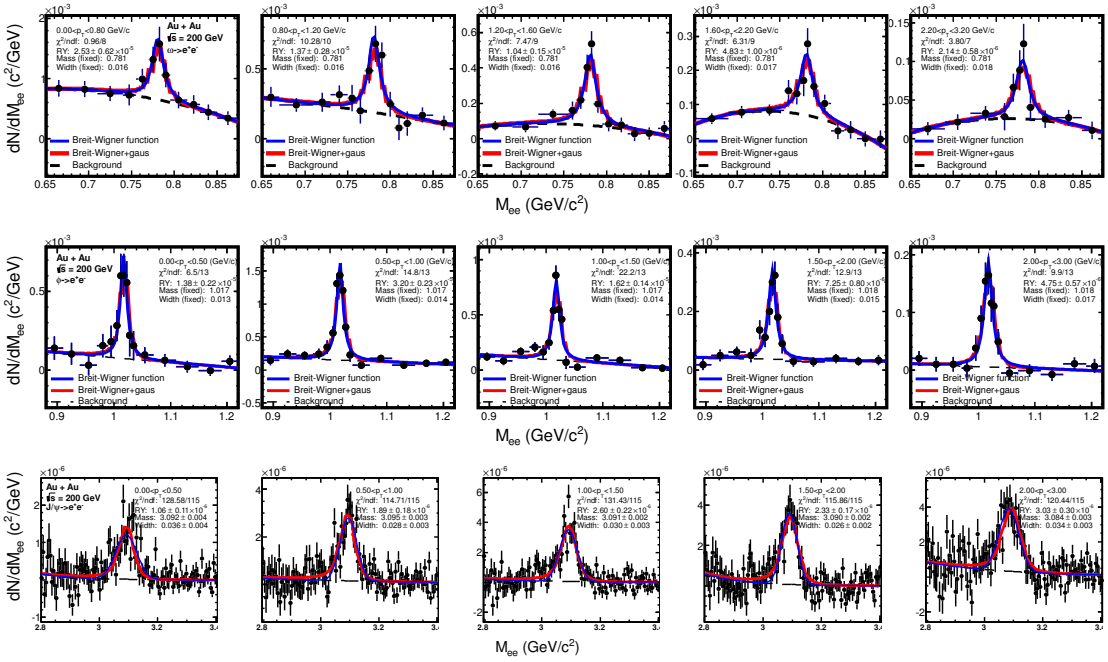

Figure 4.13 p_T dependence of the ω, ϕ and J/ψ meson invariant mass distributions from $\sqrt{s_{NN}}$ = 200 GeV Au+Au minimum bias collisions.

4.2.6 m_T slope parameters

Figure 4.15 shows the invariant transverse mass spectra in Au+Au minimum bias collisions at 200 GeV. The yields were corrected for the STAR acceptance loss ($p_T^e > 0.2GeV/c$, and $|\eta_e| < 1$) by the two method described in Sec 3.5.3. The transverse mass spectra show approximate exponential distributions in all mass windows. We used the exponential function in Eq. 4.1 to fit to measured data points up to 2.5 GeV/c^2.

$$\frac{dN}{m_T dm_T} = \frac{1}{T(m_0 + T)} \exp(-\frac{m_T - m_0}{T}) \tag{4.1}$$

The parameter T is commonly called the "slope parameter" or T_{eff}. The extracted slope parameters of inclusive dielectrons as a function of dielectron mass are shown in Fig 4.16. The results from mesons (ω, ϕ and J/ψ) measured by their dielectron decay

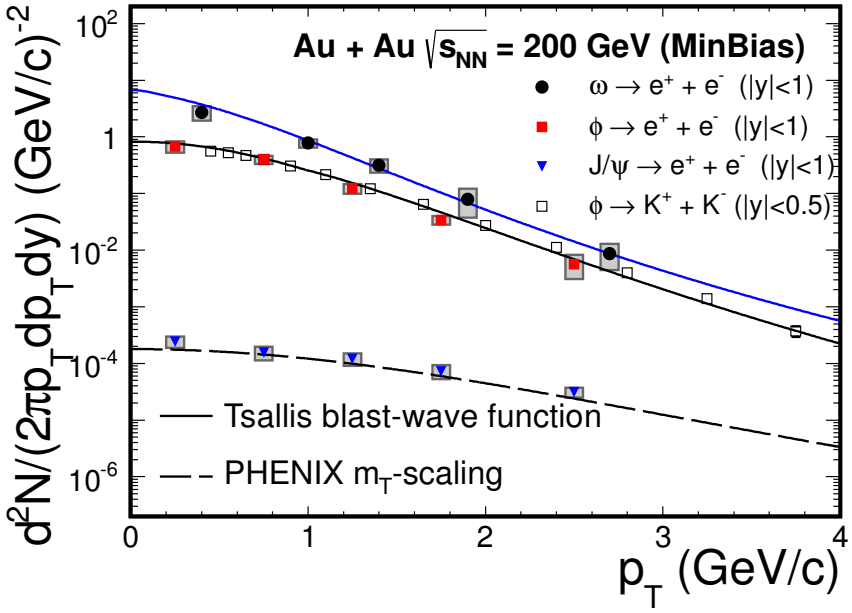

Figure 4.14 The p_T distributions of the ω, ϕ and J/ψ meson invariant yields from $\sqrt{s_{NN}}$= 200 GeV Au+Au minimum bias collisions.

channel are also included. The results from dielectron analysis are compared to previous RHIC hadron measurements [65, 69, 70, 85] and different model calculations.

In the π^0 mass region, the difference between the dielectron result and the hadron result is due to the decay kinematic change of π^0 Dalitz decay. In the mass region (0.3~1.1 GeV/c^2), the contributions to the dielectron yields are complicated. We lack knowledge of the contributions from correlated charms and the dN/dy inputs for the cocktail simulation still have large uncertainties (η and η'), which makes the data point not so intuitive to interpret. The results for mesons from their dielectron decay channel are consistent with the previous RHIC hadron measurements. In IMR (1.1~3.0 GeV/c^2), dielectron pair from the decay of correlated charm and from the thermal radiation have significantly different acceptance loss correction factor for calculating the invariant yield (Fig 3.23). Due to the lack of knowledge of both sources, we took the averaged correction factor from two sources for the central value and the variation between two extreme corrections were included as the major systematic uncertainty to the data points in IMR. In Fig 4.16, on the data points in 1~3 GeV/c^2 the lower limit of the systematic uncertainty corresponds to the correction factor assuming correlated charm pair decays, which is consistent with the expectation from PYTHIA calculation. Also included in comparison are the expected slope parameters of dielectrons from model calculation including hadronic medium and QGP thermal radiation contributions, which is consistent with the upper bound of the systematic uncertainty. Current measurements

can not distinguish these two contributions in this mass region. Future measurement on understanding the correlated charm contribution is essential to get insight into the thermal radiation.

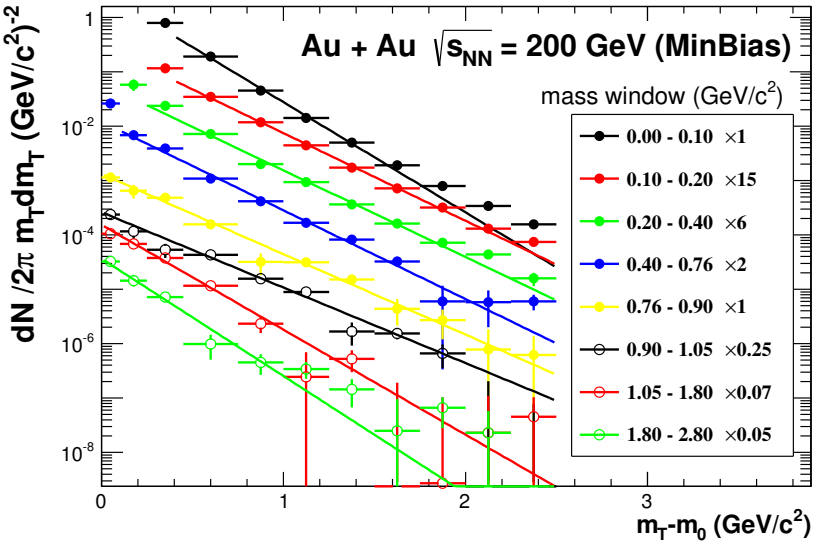

Figure 4.15 Invariant transverse mass spectra in 0-80% minimum bias collisions. The yields shown here were corrected for the STAR acceptance loss ($p_T^e > 0.2GeV/c$, and $|\eta_e| < 1$) by using the cocktail method (Sec 3.5.3).

4.3 Summary and outlook

To summarize, we have reported STAR measurements of dielectron yields at midrapidity in p+p and Au+Au collisions at 200 GeV within the STAR acceptance ($p_T^e > 0.2GeV/c$, $|\eta^e| < 1$ and $|y_{ee}|$<1). The dielectron spectra of p+p 200GeV collisions based on data taken in year 2012 have ~7 times more statistics than the STAR previous published results, which provide a better baseline for Au+Au collisions. The Au+Au results are from the combined year2010 and year2011 data.

The measured dielectron yields in Au+Au 200 GeV minimum bias collisions show an enhancement with respect to the hadronic cocktail calculations in the mass region below M_ϕ. The integrated enhancement factor in mass range 0.3~7.6 GeV/c^2 and full p_T is $1.66 \pm 0.06(stat.) \pm 0.24(sys.) \pm 0.33(cocktail)$. The enhancement factor is much smaller than the measure from PHENIX. Further measurement in differential p_T and centrality bins shows this enhancement has a mild p_T and centrality dependence with respect to the hadronic cocktail.

We compared our results to theory model calculations including a macroscopic many-body effective model and a microscopic transport model. Both models included

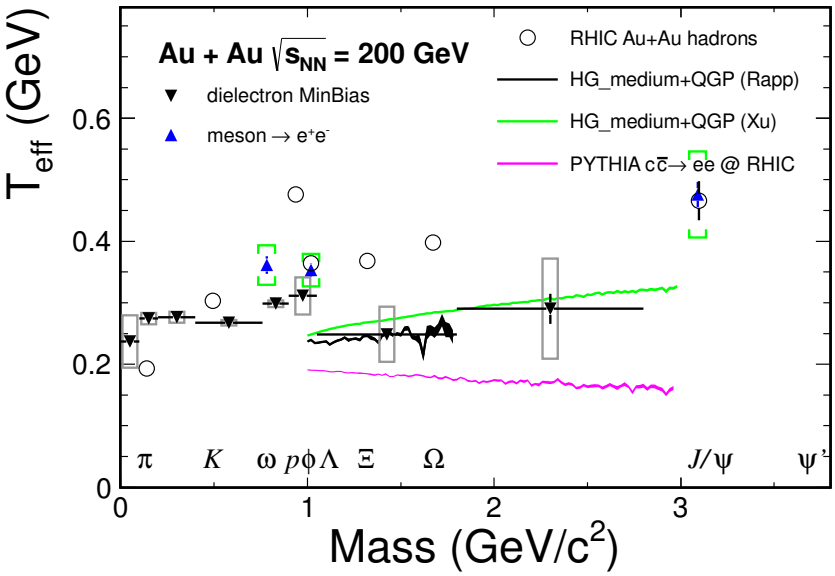

Figure 4.16 The measured inclusive dielectron slope parameter T_{eff} as a function of mass from Au+Au minimum bias data, shown as solid black triangles. The gray boxes indicated the uncertainty due to the acceptance correction factor. The blue triangles represent the slope parameters for mesons (ω, ϕ and J/ψ) measured by their dielectron decay channel. The green brackets depict the systematic uncertainties. The results from dielectron analysis are compared to previous RHIC hadron measurements. Also several model calculations are included as the solid lines.

in-medium modification of the ρ based on the broadening of its spectra function through the interactions with the hadronic medium. Both of the two models can reproduce the low mass excess observed in our date reasonably will in all p_T and centrality region. A power-law fit to the excess yield in ρ-like region vs. N_{part} shows a power of 1.48 ± 0.11.

We also reported the measurement of ω and ϕ meson production through the dielectron decay channel in Au+Au 200 GeV collisions. The measured mass position and the widths of signal distribution are well reproduced by the full GEANT simulation. The measured ϕ invariant spectrum through the dielectron decay channel is consistent with the previous measurement through hadron (K^+K^-) decay channel. The ω spectrum can also be well reproduced by the Tsallis Blast-Wave model prediction which uses the same set of parameters from the simultaneous fit to all available light hadrons measurements.

In the intermediate mass region (1.1~3 GeV/c^2), our understanding of the dielectron production is limited both statistically and systematically. We have little control on contributions from the correlated charm decays which is dominant dielectron source in this mass region. The data in minimum bias collisions can be well reproduced by the N_{bin} scaled p+p contribution from PYTHIA calculation. However, when comparing the mass spectra between minimum bias and the central collisions, the data shows a difference about 1.5σ in slopes of exponential fit in mass region 1~3 GeV/c^2. This could

be an indication of the possible modification of the correlated charm contribution or other contributing source from the medium in Au+Au collision. Due to the same reason, currently the data don't allow to disentangle the contributions from thermal radiation and correlated charm decay in m_T slope measurement.

Bibliography

[1] Adamczyk L, Agakishiev G, Aggarwal M M, et al. Di-electron spectrum at mid-rapidity in $p+p$ collisions at $\sqrt{s} = 200$ GeV. Phys. Rev. C, 2012, 86:024906.

[2] Adare A, Afanasiev S, Aidala C, et al. Detailed measurement of the e^+e^- pair continuum in p+p and Au+Au collisions at $\sqrt{s_{NN}} = 200$ GeV and implications for direct photon production. Phys. Rev. C, 2010, 81:034911.

[3] Atomssa E T. Dielectron measurements by PHENIX using the HBD. Nuclear Physics A, 2013, 904–905(0):561c–564c.

[4] Adler C, Denisov A, Garcia E, et al. The {RHIC} zero-degree calorimeters. Nuclear Instruments and Methods in Physics Research Section A: Accelerators, Spectrometers, Detectors and Associated Equipment, 2003, 499(2–3):433 – 436. The Relativistic Heavy Ion Collider Project: {RHIC} and its Detectors.

[5] Beringer J, Arguin J F, Barnett R M, et al. Review of Particle Physics. Phys. Rev. D, 2012, 86:010001.

[6] Karsch F, Laermann E. Susceptibilities, the specific heat, and a cumulant in two-flavor QCD. Phys. Rev. D, 1994, 50:6954–6962.

[7] Heinz U. CONCEPTS OF HEAVY-ION PHYSICS. arXiv:hep-ph/0407360..

[8] STAR Collaboration. Studying the Phase Diagram of QCD Matter at RHIC, 6, 2014. https://drupal.star.bnl.gov/STAR/starnotes/public/sn0598.

[9] al R. Measurement of the axial-vector τ spectral functions and determination of α_s from hadronic τ decays. The European Physical Journal C - Particles and Fields, 1998, 4(3):409–431.

[10] R Rapp J W, Hees H. The Chiral Restoration Transition of QCD and Low Mass Dileptons. arXiv: arXiv:0901.3289..

[11] Agakichiev G, Baur R, Breskin A, et al. Enhanced Production of Low-Mass Electron Pairs in 200 GeV/Nucleon S-Au Collisions at the CERN Super Proton Synchrotron. Phys. Rev. Lett., 1995, 75:1272–1275.

[12] Adamová D, Agakichiev G, Appelshäuser H, et al. Enhanced Production of Low-Mass Electron-Positron Pairs in 40-*A*GeV Pb-Au Collisions at the CERN SPS. Phys. Rev. Lett., 2003, 91:042301.

[13] Arnaldi R, Banicz K, Borer K, et al. NA60 results on thermal dimuons. The European Physical

Journal C, 2009, 61(4):711–720.

[14] NA60 Collaboration H J S. Thermal Dileptons from Hot and Dense Strongly Interacting Matter. arXiv:1011.0615 [nucl-ex]..

[15] Hahn H, Forsyth E, Foelsche H, et al. The {RHIC} design overview. Nuclear Instruments and Methods in Physics Research Section A: Accelerators, Spectrometers, Detectors and Associated Equipment, 2003, 499(2–3):245 – 263. The Relativistic Heavy Ion Collider Project: {RHIC} and its Detectors.

[16] Anderson M, Berkovitz J, Betts W, et al. The {STAR} time projection chamber: a unique tool for studying high multiplicity events at {RHIC}. Nuclear Instruments and Methods in Physics Research Section A: Accelerators, Spectrometers, Detectors and Associated Equipment, 2003, 499(2–3):659 – 678. The Relativistic Heavy Ion Collider Project: {RHIC} and its Detectors.

[17] Bieser F, Crawford H, Engelage J, et al. The {STAR} trigger. Nuclear Instruments and Methods in Physics Research Section A: Accelerators, Spectrometers, Detectors and Associated Equipment, 2003, 499(2–3):766 – 777. The Relativistic Heavy Ion Collider Project: {RHIC} and its Detectors.

[18] Weinberg S. Precise Relations between the Spectra of Vector and Axial-Vector Mesons. Phys. Rev. Lett., 1967, 18:507–509.

[19] Collins J C, Perry M J. Superdense Matter: Neutrons or Asymptotically Free Quarks? Phys. Rev. Lett., 1975, 34:1353–1356.

[20] Ejiri S. Canonical partition function and finite density phase transition in lattice QCD. Phys. Rev. D, 2008, 78:074507.

[21] Bowman E S, Kapusta J I. Critical points in the linear σ model with quarks. Phys. Rev. C, 2009, 79:015202.

[22] Cheng M, Christ N H, Datta S, et al. Transition temperature in QCD. Phys. Rev. D, 2006, 74:054507.

[23] Aoki Y, Fodor Z, Katz S, et al. The {QCD} transition temperature: Results with physical masses in the continuum limit. Physics Letters B, 2006, 643(1):46 – 54.

[24] Brown G E, Rho M. Scaling effective Lagrangians in a dense medium. Phys. Rev. Lett., 1991, 66:2720–2723.

[25] Brown G, Rho M. Chiral restoration in hot and/or dense matter. Physics Reports, 1996, 269(6): 333 – 380.

[26] R Rapp J W. Chiral Symmetry Restoration and Dileptons in Relativistic Heavy-Ion Collisions. Adv. Nucl. Phys, 2000, 25(1).

[27] Cassing W, Bratkovskaya E. Hadronic and electromagnetic probes of hot and dense nuclear matter. Physics Reports, 1999, 308(2–3):65 – 233.

[28] Gale C, Haglin K L. Electromagnetic radiation from relativistic nuclear collisions Electromagnetic radiation from relativistic nuclear collisions Electromagnetic radiation from relativistic nuclear collisions, volume 3 of *Quark-gluon plasma*. 2003: 364.

[29] Alam J, Sarkar S, Roy P, et al. Thermal Photons and Lepton Pairs from Quark Gluon Plasma and Hot Hadronic Matter. Annals of Physics, 2000, 286(2):159 – 248.

[30] Rapp R. Signatures of thermal dilepton radiation at ultrarelativistic energies. Phys. Rev. C, 2001, 63:054907.

[31] Deng J, Wang Q, Xu N, et al. Dilepton flow and deconfinement phase transition in heavy ion collisions. Physics Letters B, 2011, 701(5):581 – 586.

[32] Chatterjee R, Srivastava D K, Heinz U, et al. Elliptic flow of thermal dileptons in relativistic nuclear collisions. Phys. Rev. C, 2007, 75:054909.

[33] Shuryak E. Monitoring parton equilibration in heavy ion collisions via dilepton polarization. arXiv:1203.1012 [nucl-th]..

[34] Pisarski R D. Phenomenology of the chiral phase transition. Physics Letters B, 1982, 110(2): 155 – 158.

[35] Rapp R, Wambach J. Low-mass dileptons at the CERN-SpS: evidence for chiral restoration? The European Physical Journal A - Hadrons and Nuclei, 1999, 6(4):415–420.

[36] Porter R J, Beedoe S, Bossingham R, et al. Dielectron Cross Section Measurements in Nucleus-Nucleus Reactions at $1.0A$ GeV. Phys. Rev. Lett., 1997, 79:1229–1232.

[37] Agakichiev G, Agodi C, Alvarez-Pol H, et al. Dielectron Production in ^{12}C $+^{12}$ C Collisions at $2A$ GeV with the HADES Spectrometer. Phys. Rev. Lett., 2007, 98:052302.

[38] Agakishiev G, Balanda A, Belver D, et al. Dielectron production in Ar + KCl collisions at $1.76A$ GeV. Phys. Rev. C, 2011, 84:014902.

[39] al A. Excess of continuum dimuon production at masses between threshold and the J/Ψ in S-W interactions at 200 GeV/c/nucleon. The European Physical Journal C - Particles and Fields, 2000, 13(3):433–452.

[40] Collaboration T C. e + e–pair production in Pb-Au collisions at 158 GeV per nucleon. The European Physical Journal C - Particles and Fields, 2005, 41(4):475–513.

[41] Arnaldi R, Averbeck R, Banicz K, et al. First Measurement of the ρ^0 Spectral Function in High-Energy Nuclear Collisions. Phys. Rev. Lett., 2006, 96:162302.

[42] Arnaldi R, Banicz K, Castor J, et al. Evidence for Radial Flow of Thermal Dileptons in High-Energy Nuclear Collisions. Phys. Rev. Lett., 2008, 100:022302.

[43] Baur R, Breskin A, Chechik R, et al. The {CERES} {RICH} detector system. Nuclear Instruments and Methods in Physics Research Section A: Accelerators, Spectrometers, Detectors and Associated Equipment, 1994, 343(1):87 – 98.

[44] Agakichiev G, Baur R, Braun-Munzinger P, et al. Low-mass e+e− pair production in 158 A GeV Pb-Au collisions at the {CERN} SPS, its dependence on multiplicity and transverse momentum. Physics Letters B, 1998, 422(1–4):405 – 412.

[45] Brown G, Rho M. On the manifestation of chiral symmetry in nuclei and dense nuclear matter. Physics Reports, 2002, 363(2):85 – 171.

[46] Ruppert J, Gale C, Renk T, et al. Low Mass Dimuons Produced in Relativistic Nuclear Collisions. Phys. Rev. Lett., 2008, 100:162301.

[47] Hees H, Rapp R. Dilepton radiation at the {CERN} super-proton synchrotron. Nuclear Physics A, 2008, 806(1–4):339 – 387.

[48] Dusling K, Zahed I. Transverse momentum spectra of dileptons measured by the NA60 Collaboration in In + In collisions at 158 GeV/nucleon. Phys. Rev. C, 2009, 80:014902.

[49] Ackermann K, Adams N, Adler C, et al. {STAR} detector overview. Nuclear Instruments and Methods in Physics Research Section A: Accelerators, Spectrometers, Detectors and Associated Equipment, 2003, 499(2–3):624 – 632. The Relativistic Heavy Ion Collider Project: {RHIC} and its Detectors.

[50] Anderson M, Bieser F, Bossingham R, et al. A readout system for the {STAR} time projection chamber. Nuclear Instruments and Methods in Physics Research Section A: Accelerators, Spectrometers, Detectors and Associated Equipment, 2003, 499(2–3):679 – 691. The Relativistic Heavy Ion Collider Project: {RHIC} and its Detectors.

[51] Eidelman S, Hayes K, Olive K, et al. Review of Particle Physics. Physics Letters B, 2004, 592(1–4):1 – 5. Review of Particle Physics.

[52] Bichsel H. A method to improve tracking and particle identification in {TPCs} and silicon detectors. Nuclear Instruments and Methods in Physics Research Section A: Accelerators, Spectrometers, Detectors and Associated Equipment, 2006, 562(1):154 – 197.

[53] Zeballos E C, Crotty I, Hatzifotiadou D, et al. A new type of resistive plate chamber: The multigap {RPC}. Nuclear Instruments and Methods in Physics Research Section A: Accelerators, Spectrometers, Detectors and Associated Equipment, 1996, 374(1):132 – 135.

[54] Adler C, Berger J, Demello M, et al. The {STAR} Level-3 trigger system. Nuclear Instruments and Methods in Physics Research Section A: Accelerators, Spectrometers, Detectors and Associated Equipment, 2003, 499(2–3):778 – 791. The Relativistic Heavy Ion Collider Project: {RHIC} and its Detectors.

[55] Observation of the antimatter helium-4 nucleus. Nature, 2011, 473(7347):353–356.

[56] Ke H. Beam Energy, Collision Centrality and Charge Asymmetry Dependence of the Pion Event Anisotropy in Au+Au Collisions at RHIC[D]. Central China Normal University, 5, 2013.

[57] Zhao J. Dielectron production at RHIC[D]. Shanghai Institute of Applied Physics Chinese Academy of Sciences, May, 2013.

[58] Huang B. Di-lepton production measurements in p+p and Au+Au collisions at RHIC[D]. University of Science and Technology of China, 2011.

[59] Miller M L, Reygers K, Sanders S J, et al. Glauber Modeling in High-Energy Nuclear Collisions. Annual Review of Nuclear and Particle Science, 2007, 57(1):205–243.

[60] GEANT 3.21, CERN program library. http://wwwasdoc.web.cern.ch/wwwasdoc/22geanthtml3/geantall.html..

[61] (STAR Collaboration) L A. Observation of D^0 meson nuclear modifications in Au+Au collisions at $\sqrt{s_{NN}}$= 200 GeV. arXiv:1404.6185..

[62] Tang Z, Xu Y, Ruan L, et al. Spectra and radial flow in relativistic heavy ion collisions with Tsallis statistics in a blast-wave description. Phys. Rev. C, 2009, 79:051901.

[63] Sjöstrand T, Edén P, Friberg C, et al. High-Energy-Physics Event Generation with PYTHIA 6.1. Comput. Phys. Commun., 2001, 135:238.

[64] Adamczyk L, Agakishiev G, Aggarwal M M, et al. Measurements of D^0 and D^* production in p+p collisions at $\sqrt{s}$=200 GeV. Phys. Rev. D, 2012, 86:072013.

[65] Adams J, Adler C, Aggarwal M M, et al. Identified Particle Distributions in pp and Au + Au Collisions at $\sqrt{s_{NN}} = 200$ GeV. Phys. Rev. Lett., 2004, 92:112301.

[66] Abelev B I, Aggarwal M M, Ahammed Z, et al. Identified Baryon and Meson Distributions at Large Transverse Momenta from Au + Au Collisions at $\sqrt{s_{NN}} = 200$ GeV. Phys. Rev. Lett., 2006, 97:152301.

[67] Adams J, Adler C, Aggarwal M M, et al. ρ^0 Production and Possible Modification in Au+Au and p+p Collisions at $\sqrt{s_{NN}}$=200 GeV. Phys. Rev. Lett., 2004, 92:092301.

[68] STAR Collaboration) B H. Acta Phys. Pol. B Proc. 5, 2012, 471.

[69] Adams J, Adler C, Aggarwal M, et al. ϕ meson production in and collisions at. Physics Letters B, 2005, 612(3–4):181 – 189.

[70] Adare A, Afanasiev S, Aidala C, et al. J/ψ Production versus Centrality, Transverse Momentum, andRapidity in Au+Au Collisions at $\sqrt{s_{NN}}$=200 GeV. Phys. Rev. Lett., 2007, 98:232301.

[71] al R G. Int. J. Mod. Phys. A, 1030431995.

[72] Silva C L. Quarkonia measurement in and collisions at by {PHENIX} Detector. Nuclear Physics A, 2009, 830(1–4):227c – 230c. Quark Matter 2009 The 21st International Conference on Ultrarelativistic Nucleus-Nucleus Collisions.

[73] Adamczyk L, Adkins J K, Agakishiev G, et al. Dielectron Mass Spectra from Au + Au Collisions at $\sqrt{s_{NN}} = 200$ GeV. Phys. Rev. Lett., 2014, 113:022301.

[74] Eletsky V L, Belkacem M, Ellis P J, et al. Properties of ρ and ω mesons at finite temperature

and density as inferred from experiment. Phys. Rev. C, 2001, 64:035202.

[75] Braaten E, Pisarski R D, Yuan T C. Production of soft dileptons in the quark-gluon plasma. Phys. Rev. Lett., 1990, 64:2242–2245.

[76] Rapp R. PoS CPOD2013, 2013, 008.

[77] Xu H j, Chen H f, Dong X, et al. Di-electron production from vector mesons with medium modifications in heavy ion collisions. Phys. Rev. C, 2012, 85:024906.

[78] Vujanovic G, Young C, Schenke B, et al. Dilepton production in high energy heavy ion collisions with 3+1D relativistic viscous hydrodynamics. Nuclear Physics A, 2013, 904–905(0): 557c – 560c. The Quark Matter 2012 Proceedings of the {XXIII} International Conference on Ultrarelativistic Nucleus–Nucleus Collisions.

[79] G Vujanovic e a. Dilepton emission in high-energy heavy-ion collisions with viscous hydrodynamics. arXiv:1312.0676 [nucl-th]..

[80] Cassing W, Bratkovskaya E. Parton–hadron–string dynamics: An off-shell transport approach for relativistic energies. Nuclear Physics A, 2009, 831(3–4):215 – 242.

[81] Bratkovskaya E, Cassing W, Konchakovski V, et al. Parton–Hadron-String Dynamics at relativistic collider energies. Nuclear Physics A, 2011, 856(1):162 – 182.

[82] Bratkovskaya E, Cassing W. Dilepton production from {AGS} to {SPS} energies within a relativistic transport approach. Nuclear Physics A, 1997, 619(3–4):413 – 446.

[83] Heinz U, Lee K S. The ϱ-peak in the dimuon spectrum as a clock for fireball lifetimes in relativistic nuclear collisions. Physics Letters B, 1991, 259(1–2):162 – 168.

[84] Adare A, Afanasiev S, Aidala C, et al. Energy Loss and Flow of Heavy Quarks in Au + Au Collisions at $\sqrt{s_{\rm NN}} = 200$ GeV. Phys. Rev. Lett., 2007, 98:172301.

[85] Agakishiev G, Aggarwal M M, Ahammed Z, et al. Strangeness Enhancement in Cu-Cu and Au-Au Collisions at $\sqrt{s_{NN}} = 200$ GeV. Phys. Rev. Lett., 2012, 108:072301.

[86] Adare A, Afanasiev S, Aidala C, et al. Quantitative constraints on the transport properties of hot partonic matter from semi-inclusive single high transverse momentum pion suppression in Au+Au collisions at $\sqrt{s_{NN}} = 200$ GeV. Phys. Rev. C, 2008, 77:064907.

[87] Guo Y, Star collaboration. Dielectron production in 200 GeV p+p and Au+Au collisions at STAR. Journal of Physics: Conference Series, 2014, 535(1):012006.

Appendix A χ2 test of the model calculation for the Low-Mass dielectron spectra

In order to quantify how different model compare with the measured data in Fig 4.4, a χ2 test are performed. but in our measured data, the total uncertainty contain three part: (1)statistical uncertainty, (2)systematic uncertainty and (3)the cocktail uncertainty. Here the uncertainty(1) are independent for each data point, uncertainty(2) and (3) are correlated for each data point, so we used a new χ2 calculation method [86], which list below:

$$\chi^2 = \sum_{i=1}^{n} \frac{[y_i + \varepsilon_b \sigma_{b_i} - \mu_i(\vec{p})]^2}{\widetilde{\sigma}_i^2} + \varepsilon_b^2 \tag{A.1}$$

where y_i is the measured data point, σ_i are independent uncertainty, μ_i are the model value. σ_{b_i} are the correlated uncertainty,ε_b are the fraction variation of the σ_{b_i}, and $\widetilde{\sigma}_i$ is the uncertainty scaled by the multiplicative shift in y_i such that the fractional uncertainty is unchanged under shifts. In our calculation, the statistical uncertainty are consider as independent for each data point, systematic uncertainty and cocktail uncertainty are consider as the correlated uncertainty, which is defined following:

$$\widetilde{\sigma}_i = \sigma_i(\frac{y_i + \varepsilon_b \sigma_{b_i}}{y_i}) \tag{A.2}$$

The scan results are shown in Fig A.1 and A.2. The minimum χ^2 and corresponding ε_b are listed in table A.1.

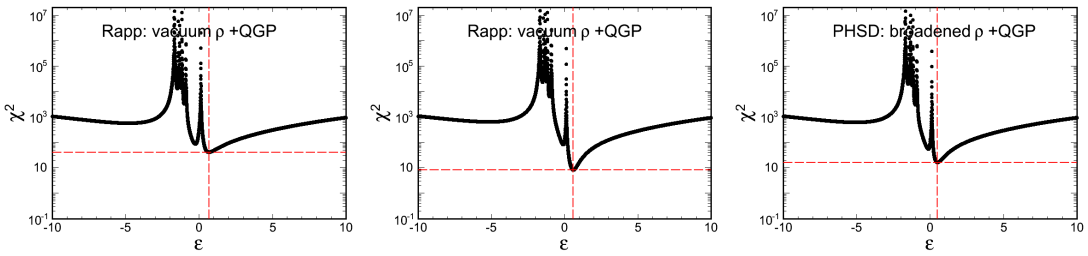

Figure A.1 χ^2 vs ε_b from vacuum ρ (left), in-medium ρ (middle), PHID (right) at mass range 0.3−1.0GeV /c^2

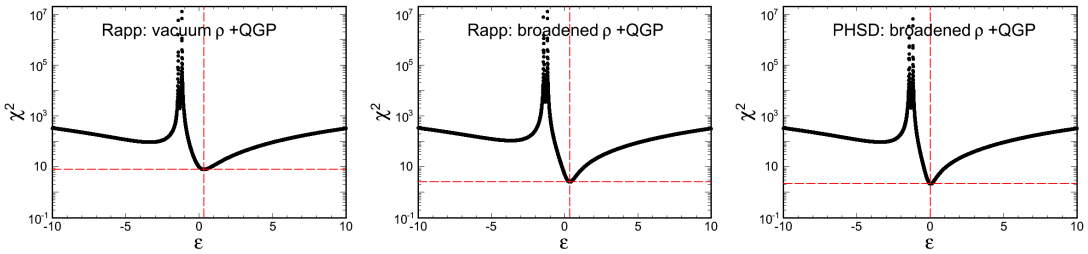

Figure A.2 χ^2 vs ε_b from vacuum ρ (left), in-medium ρ (middle), PHID (right) at mass range 0.8−1.0GeV /c^2

Model:	ε_b	χ^2/ndf	p-value
Rapp: vaccum ρ +QGP	0.668	41.0/8	2.1×10^{-6}
Rapp: broadened ρ +QGP	0.5	8.2/8	0.41
PHSD: broadened ρ +QGP	0.596	16.4/8	0.037

Table A.1 χ^2/ndf for model calculations compare to the excess data in mass region: 0.3-1.0 GeV/c^2.

ACKNOWLEDGMENTS

First and foremost I would like to express my deepest gratitude to my supervisor Prof. Nu Xu and Prof. Ziping Zhang for introducing me to the relativistic heavy-ion physics research. With their encouragement, tremendous support and sound advice, they make the research interesting for me. I would like to thank Dr. Timothy Hallman, Dr. James Dunlop, Prof. Zhangbu Xu, Prof. Nu Xu and Prof. Peter Jacobs for offering me the opportunity to work at BNL and LBNL. Prof. Nu Xu provided me wise advice, excellent ideas and brilliant guidance in my research. I learned a lot from him and I want to express my sincerely thanks to him.

I would especially thank Dr. Xin Dong for guiding me through all the detailed analysis in my research for two years. His perpetual energy and enthusiasm in research had motivated me. He offered me plenty helps and fruitful discussions. I benefit a lot from his guidance. I would have been lost without him. Also I would thank to Dr. Aihong Tang, he guided me in the work of the High Level Trigger and leaded me into the gate of experimental physics. And many thanks to Dr. Lijuan Ruan, she offered me plenty helps in analysis and physics.

I would like to thank Prof. Yifei Zhang and Dr. Bingchu Huang who introduced me into the data analysis. They keeps offering me the help in my research. I would also like to thank Dr. Jie Zhao. He worked together with me in the dielectron analysis and it is a pleasant experience to work with him and I learned a lot from him. My thanks also to Dr. Hongwei Ke, I worked with him on the High Level Trigger. He introduced me into the computing science and helped me a lot on programming. I would like to thank Dr. Chi Yang and Qiye Shou, my roommates in BNL, for enjoyable corporation on work and living and abundant helpful discussions. I would like to thank Ms. Xiangli Cui and Mr. Hao Qiu for their assistances in my research.

I would like to thank the dielectron physics group at STAR collaboration, especially Prof Frank Geurts, Dr. Patrick Huck, Joey Butterworth , Kefeng Xin. I would like to express my thanks to the STAR group colleagues at BNL and High Energy Physics Group colleagues at USTC, especially Prof Hongfang Chen, Prof. Zizong Xu, Prof. Xiaolian Wang, Prof. Qun Wang, Prof. Ming Shao, Mr. Hui Zeng. And I must thanks Dr. Hao qiu, Prof. Shusu Shi, Xu Sun, Long Ma and Dr. Alexander Schmah for they

help during my stay at LBNL. It is really a beautiful experience in my life.

I would like to thank all my friends for inspiring me in research and life during the 5 years we spent together at USTC, BNL and LBNL. They are, for example, Chengming Du, Yan Yang, Lizhu Chen, Xiangli Cui, Xuan Li, Yuhui Zhu, Liqin Han, Wangmei Zha, Liang Zheng and so on.

Finally, my deep gratitude goes to my parents for their unflagging love and support throughout my life. This dissertation is impossible without them.

Yi Guo

14 September 2014

Presentations and publication List

Presentations:

1. Oct. 2012, Centrality and p_T Dependence Study of Di-electron Production in $\sqrt{s_{NN}}$ = 200 GeV Au+Au Collisions at STAR, oral presentation, American Physical Society's meeting of the Division of Nuclear Physics, CA, USA.

2. Apr. 2014, Dielectron production in 200 GeV p+p and Au+Au collisions at STAR, oral presentation, 30th Winter Workshop on Nuclear Dynamics (WWND 2014), TX, USA.

3. Apr. 2014, Dielectron production in 200 GeV p+p and Au+Au collisions at STAR , oral presentation, 中国物理学会高能物理分会第九届全国会员代表大会暨学术年会, 武汉。

4. Aug. 2014, Dielectron production at STAR, oral presentation, STAR Regional Meeting & a workshop on "high temperature and high density nuclear matter study", Weihai, China.

Posters:

1. Aug. 2012, Centrality and p_T Dependence Study of Di-electron Production in $\sqrt{s_{NN}}$ = 200 GeV Au+Au Collisions at STAR, poster, Quark Matter 2012 International Conference, Washington, DC, USA.

2. May. 2014, Dielectron production in p+p and Au+Au collisions at $\sqrt{s_{NN}}$ = 200 GeV at STAR, Quark Matter 2014, Darmstadt Germany.

Publication:

1. ***(Principal Author),*** Adamczyk L, Adkins J K, Agakishiev G, et al. Dielectron Mass Spectra from Au + Au Collisions at $\sqrt{s_{NN}} = 200$ GeV. Phys. Rev. Lett., 2014, 113:022301

2. Proceeding for 30th Winter Workshop on Nuclear Dynamics (WWND 2014), Guo Y, Star collaboration. Dielectron production in 200 GeV p+p and Au+Au collisions at STAR. Journal of Physics: Conference Series, 2014, 535(1):012006